Sensitivity Analysis of Numerical Thermal Predictions for Turbine Stator Vanes

Sensitivitätsanalyse Numerischer Thermalvorhersagen für Turbinenstatorschaufeln
Master-Thesis by Paolo Salvatore from Guardiagrele
Day of Submission: 28/08/2017

Supervisor: M.Sc. Jonathan Hilgert

TECHNISCHE
UNIVERSITÄT
DARMSTADT

GLR
Institute of Gas Turbines and Aerospace
Propulsion

Sensitivity Analysis of Numerical Thermal Predictions for Turbine Stator Vanes
Sensitivitätsanalyse Numerischer Thermalvorhersagen für Turbinenstatorschaufeln

Master-Thesis by Paolo Salvatore from Guardiagrele

Supervisor: M.Sc. Jonathan Hilgert

Day of submission: 28.08.2017

Declaration of Authorship

I herewith formally declare that I, Paolo Salvatore, have written the submitted thesis independently. I did not use any outside support except for the quoted literature and other sources mentioned in the paper. I clearly marked and separately listed all of the literature and all of the other sources which I employed when producing this academic work, either literally or in content. This thesis has not been handed in or published before in the same or similar form.

I am aware, that in case of an attempt at deception based on plagiarism (§38 Abs. 2 APB), the thesis would be graded with 5,0 and counted as one failed examination attempt. The thesis may only be repeated once.

In the submitted thesis the written copies and the electronic version for archiving are identical in content.

Darmstadt, August 28, 2017

_____

(Paolo Salvatore)

To my family.

Acknowledgements

Contents

List of Figures

List of Tables

Nomenclature

Greek Characters

γ	$\frac{c_p}{c_v}$ Isentropic Exponent	$[-]$
δ	Boundary Layer Thickness	$[m]$
ε	Energy Dissipation	$\left[J \cdot kg^{-1}\right]$
η	Adiabatic Effectiveness	$[-]$
κ	Thermal Conductivity and kinetic energy	$\left[W \cdot m^{-1} \cdot K^{-1}\right] - [N \cdot m]$
μ	Laminar Viscosity	$\left[kg \cdot m^{-1}s^{-1}\right]$
μ_t	Turbulent Viscosity	$\left[kg \cdot m^{-1}s^{-1}\right]$
ν	Cinematic Viscosity	$\left[m^2 s^{-1}\right]$
ν_t	Cinematic Viscosity	$\left[m^2 s^{-1}\right]$
ρ	Density	$\left[kg \cdot m^{-3}\right]$
τ	Reynolds Stresses Tensor	$\left[N \cdot m^{-2}\right]$
ϕ	Dissipations and Overall Effectiveness	$\left[J \cdot m^{-3}\right] - [-]$
ω	$\frac{\epsilon}{\kappa}$	$[-]$

Latin characters

a	Thermal Diffusivity	$\left[m^2 \cdot s^{-1}\right]$
C_p	Heat Capacity at Constant Pressure	$\left[J \cdot K^{-1} \cdot kg^{-1}\right]$
C_v	Heat Capacity at Constant Volume	$\left[J \cdot K^{-1} \cdot kg^{-1}\right]$
E	Total Energy	$\left[W \cdot m^{-2}\right]$
h	Specific Enthalpy	$\left[J \cdot kg^{-1}\right]$
I	Identity Matrix and Inlet Turbulent Intensity	$[-] - [-]$
l	Characteristic Length	$[m]$
M	Blowing Ratio	$[-]$
Ma	Mach Number	$[-]$
Nu	Nusselt Number	$[-]$
P	Pressure	$[bar]$
Pr	Prandtl Number	$[-]$
q	Heat Flux	$\left[W \cdot m^{-2}\right]$
R	Specific Universal Gas Constant	$\left[J \cdot kg^{-1} \cdot K^{-1}\right]$
Re	Reynolds Number	$[\cdot]$
s	Specific Entropy	$\left[J \cdot kg^{-1} \cdot K^{-1}\right]$
S	Mean Rate if Strain	$\left[N \cdot m^{-2}\right]$
t	Time	$[s]$
T	Temperature	$[K]$
u	Velocity component in the x direction	$\left[m \cdot s^{-1}\right]$
u'	Turbulent Fluctuation Velocity	$\left[m \cdot s^{-1}\right]$
$\tilde{u}$	Weighted Average of the Velocity on the Density	$\left[m \cdot s^{-1}\right]$

u''	Favre Fluctuation Velocity	$\left[m \cdot s^{-1}\right]$
U	Mean Streamvise Velocity	$\left[m \cdot s^{-1}\right]$
v	Velocity component in the y direction	$\left[m \cdot s^{-1}\right]$
x	Position Vector in the x direction	$\left[m\right]$

Subscripts

99	99%
aw	Adiabatic Wall
c, out	Coolant Hole Referred
x	axial
r	Reference State
t	Stagnation State
w	Wall Referred
∞	Free Stream Referred
x	1D Referred

Acronymus

EVM	**E**ddy **V**iscosity **M**odels
$FFTB$	Heat **F**lux **F**orward **T**emperature **B**ack
$hFFB$	**H**eat Transfer Coefficient **F**orward Heat **F**lux **B**ack
$hFTB$	**H**eat Transfer Coefficient **F**orward **T**emperature **B**ack
NGV	**N**ozzle **G**uide **V**ane
SMC	**S**econd-**M**oment **c**losure Models
SST	**S**hear **S**tress **M**odel
TET	**T**urbine **E**ntry **T**emperature
$TFFB$	**T**emperature **F**orward Heat **F**lux **B**ack

Mathematics Operators

$\nabla \cdot$	Divergence Operator
∇	Gradient Operator
$\frac{d}{dx_i}$	Derivation Operator
$\frac{D}{Dt}$	Total Derivation Operator
$\frac{\partial}{\partial x_i}$	Partial Derivation Operator
$\frac{\partial^2}{\partial x_i^2}$	Second Order Partial Derivation Operator

1 Introduction

In jet engines the efficiency is directly related to the turbine entry temperature (TET), because of that in modern, high-efficiency gas turbine engines, the gas temperature often exceeds the allowable temperatures of the metal parts in much of the hot section. To maintain the integrity of the airfoils, they are usually cooled, Figure 1.1, with air flowing through internal passages of varying complexity. Film cooling is also commonly used in conjunction with internal cooling when the thermal environment is extremely severe.

An internally cooled turbine airfoil at operating conditions consists of three heat transfer "prob-
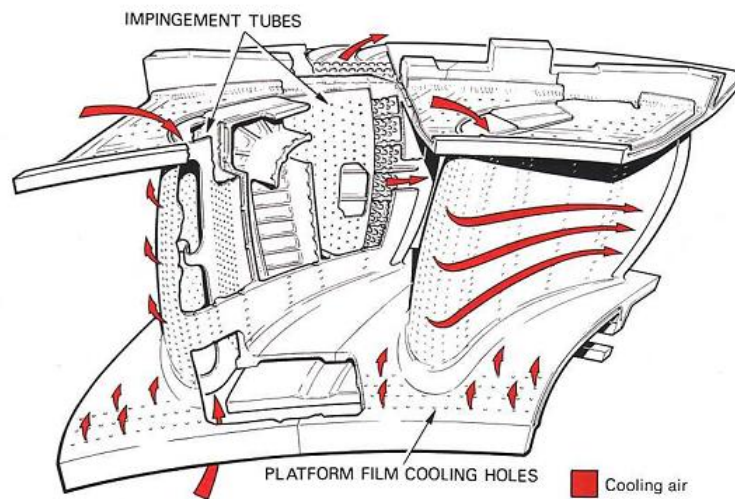
Figure 1.1: The cooling systems in turbine vanes, [4]

lems" that are inherently linked: external convection, internal convection, and conduction within the metal. It is the metal temperature distribution, and the temperature gradients, which ultimately determine the life of the part. However, due to the complex, coupled nature of the heat transfer problem, accurate prediction of the metal temperature is quite difficult from a design stand-point.

To better predict the heat exchange, coupled simulations can be performed; in this case the solution of the Navier-Stokes equations is modified by imposing zero velocity in the solid domain in order to solve the conduction problem. Another option is the "soft coupling", [6]: in this simulation two domains are created, one for the solid and one for the fluid. After that, the boundary condition between the two domains are iteratively changed until the convergence is achieved. This method requires two independent solvers, but allows to use different schemes for solving the domain, for example FEM for solid and finite volume in the fluid.

In the method heat flux forward temperature back (FFTB), the heat flux is exported from the fluid domain by imposing a guess wall temperature distribution. The exported heat flux is then applied

as boundary condition in the solid domain. Using the findings obtained from the solid domain, the fluid simulation is updated using the new boundary condition and so on until the convergence is reached.

An alternative approach is the temperature forward heat flux back (TFFB) method. In this process, the heat flux is imposed as boundary condition in the fluid domain and the temperature distribution is used as boundary condition in the solid side.

The *Biot number* is a measure of the stability of the method: if the value is above one, the first method tends to be stable; vice versa, if the value is lower than one, the second method tends to be stable.

$$Bi = \frac{htc}{\kappa/l}$$

An alternative approach is to use the *Newton Law* to model the wall heat flux in the solid domain. The driving force of the phenomenon is the temperature gradient $T_f - Tw$ (fluid temperature - wall temperature). The possibilities are to impose the temperature in the fluid walls and than to impose the *htc* in the solid domain and the method is called heat transfer coefficient forward temperature back (hFTB). The second option is to use the heat flux in the fluid domain and the method is called heat transfer coefficient forward heat flux back (hFFB). However, this process is time-consuming, often requiring multiple iterations, and accuracy is lost in the decoupling. It is far more accurate and efficient to run a single numerical simulation to solve the entire heat transfer problem at once, known as the conjugate approach.

Although the discussed conventional design method is still the state-of-the-art for finding the basic thermal design of a film-cooled blade, the conjugate calculation can be a valuable tool for the numerical test of the configuration with respect to the thermal load. The conjugate calculation methods are based on a coupled calculation of the fluid flow, heat transfer at solid/fluid boundaries and heat conduction in the solid walls. The 3-D simulations require much effort compared to the other methods, but the conjugate calculation can be used for further improvement of the thermal design.

The basic idea of coupled fluid flow and heat transfer calculations is not a new idea, but, it was the significant increase in calculation capabilities, Figure 1.2, based on new computer generations which allowed several research groups in the early 1990s to develop computation codes for 2-D and 3-D conjugate calculations.

CHT simulation can be divided in methods based on a hybrid coupling and homogeneous methods. The hybrid strategy is performed on existing CFD solvers, which are coupled to a conventional FEM solver for the temperature distribution in the solid walls.

The homogeneous method involves the direct coupling of the fluid flow and the solid body using the same discretisation and numerical approach for both zones. In this thesis directly coupled simulations are performed and a particular focus has been placed on the *heat transfer coefficient* calculation in order to verify the error which is committed in the uncoupled simulations. Furthermore another htc calculation method was used and compared with the classic one.

As said before, the temperature gradients, for example, are particularly dangerous for the stress distribution in the vane wall, therefore through this work the magnitude and the position of the zones most sensible was taken into account. This quantity, that in the following is called *sensitivity*,
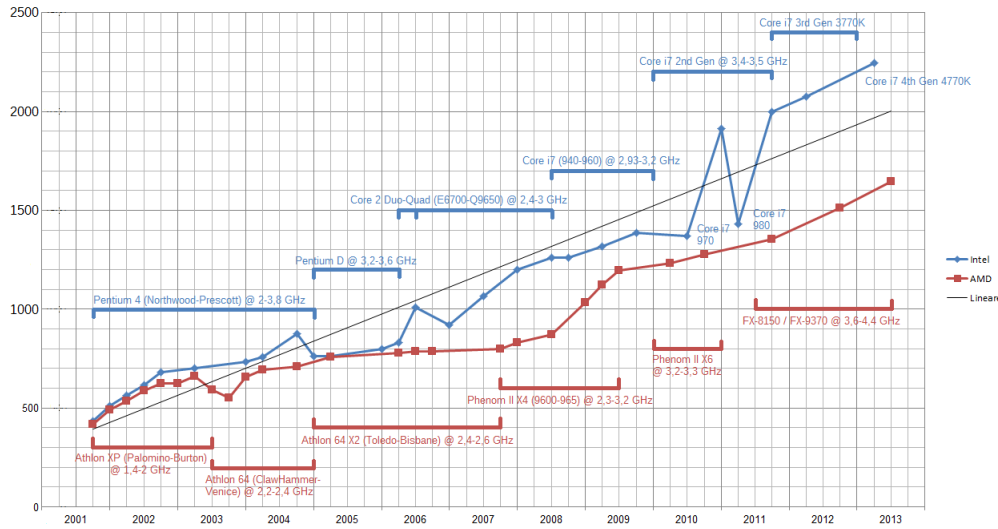
Figure 1.2: CPU Performances growing [1]

gives information of the principal critical zones of the vane due to change of the external properties.

The main goal of this thesis is to perform simulations on different cases and then try to superimpose the findings obtained. In fact, 2 different test cases and one more realistic vane were used . The first test case was a very simple geometry vane with 10 internal cooling ducts (Mark II), the second was a model of the leading edge of the vane with film cooling (LE). Thanks to these two models the results collected were compared with the findings of the realistic MT1 NGV with internal cooling and film cooling .

1.1 Motivations

An the end of the day, the designer of turbines would like to have the highest TET as possible. Unfortunately, the material used for the vanes is not so strong to hold these stresses. There are multiple factors that influence the life of the vanes and one important advantage would be to know which are the most influential.

In order to reduce the heat transfer from the fluid to the solid, the cooling systems are used. The internal cooling and the film cooling are analysed in this thesis, by regarding the efficiency and the influence of the cooling on the vane aerothermal behavior. The presence within the vane of these cooling systems could cause mechanical failures and also aerodynamic losses. However, the life of the vane is closely related to these equipments. Hence, the prediction of the cooling systems efficiency is required in order to avoid an overestimation of the system.

Usually, the design of the vanes is performed with very robust methods, such as the calculation of the htc distribution used in a FEM solver. Nowadays, the thermal loads that the vanes are called upon to hold must be managed in the right way. The conjugate heat transfer simulations are powerful computational methods which can simulate the interaction between the solid and the fluid in a very precise way. Moreover, the prediction of the physical quantities is better performed

because an iteration of the results is not required, so that high computational errors are in this manner avoided. During the last years, the CHT simulations are growing in popularity and now represent a very good tool which can help to design.

The main focus on this thesis is placed on the CHT simulations. Two low fidelity test cases are analysed by varying the inlet boundary condition values. Moreover, simulations on a more realistic vane are also performed. In the end, the findings gained with the low fidelity cases are superimposed onto the more realistic vane in order to find the most influential causes. The inlet parameter analysed is the Mach number because, as can be seen in the following chapters, the influence of the Reynolds number can be considered negligible in the low fidelity cases.

Furthermore, the film cooling problem is treated. The inlet Mach number variation leads to a change of the blowing ratio, which is one of the most characterising factors of the film cooling. The influence of the blowing ratio and its implication on the results are also explained during the thesis. The parameter used to compare the cases is the sensitivity. The value of this factor gives information of the most affected zones.

The heat transfer coefficient is used, nowadays, in the turbine vane design. The method to achieve the htc distribution uses a lot of approximations that can lead to errors. However, the error is accepted because the industries are used to implementing these methods. Another objective of the thesis is the analysis of the htc prediction and the comparison with the results obtained with the CHT simulation. The goal is trying to figure out if the classic design method is still valid or if it is necessary to set the eye toward a new predictions horizon.

2 Theoretical Basis

2.1 The Navier Stokes Equations and turbulence treatment

Using a finite domain big enough to use the continuous hypothesis the following equations can be written

$$\begin{cases} \frac{D\rho}{Dt} + \rho \nabla \cdot \overrightarrow{u} = 0 \\ \rho \frac{D\overrightarrow{u}}{Dt} = \rho \overrightarrow{F_\nu} + \nabla \cdot \underline{T} \\ \frac{\partial(\rho E)}{\partial t} + \nabla \cdot (\rho E \overrightarrow{u}) = -\nabla \cdot \overrightarrow{q} - \nabla \cdot (\underline{T}\,\overrightarrow{u}) \end{cases} \tag{2.1}$$

Where ρ is the density, $\overrightarrow{u} = (u, v, z)$ is the velocity vector, $\overrightarrow{F_\nu}$ are the external volume forces, $\underline{T}$ is the stress tensor, E is the total energy and $\overrightarrow{q}$ is the heat flux.

This system of three equations defines the flow movement and its exchange of energy and momentum with the external bodies.

The first equation of 2.1, is the continuity equation and states the mass conservation within the volume. The second equation is the momentum equation and controls the exchange of forces around the volume. The last one is the total energy equation that groups momentum and heat flux exchange. It is important to underline that these equations express the conservation of a property and also, written in that form, the independence by the system of reference[1].

By dealing with Newtonian fluid, in which the state $\tau = \mu \frac{du}{dy}$ is valid, the stress tensor $\underline{T}$ can be expressed as follow

$$\underline{T} = p\underline{I} - \rho\,\nu\left(\nabla\overrightarrow{u} + \nabla\overrightarrow{u}^T - \frac{2}{3}\nabla \cdot \overrightarrow{u}\,\underline{I}\right)$$

In industry the major part of the effort is spent for turbulence flows. The characteristic of these flows is the random movement of the particles and, consequently, the stream lines are not parallel, anymore. The *fluctuations*, as can be seen in Figure 2.1 of the particles lead to a higher momentum exchange than the laminar flows.

The computation effort is strongly incremented due to the fluctuations; in order to reduce the computing time the RANS equations, or Reynolds averaged Navier-Stokes equations, were introduced. The fluctuations are not visible anymore in the simulation, but the effect of the momentum exchange can be seen and, even if with less precision, the designers can use this valid tool during the product development process.

---

[1] The operators $\frac{\partial(\cdot)}{\partial t}$, $\frac{D(\cdot)}{Dt}$ and $\nabla(\cdot)$ are Galilean Invariants.
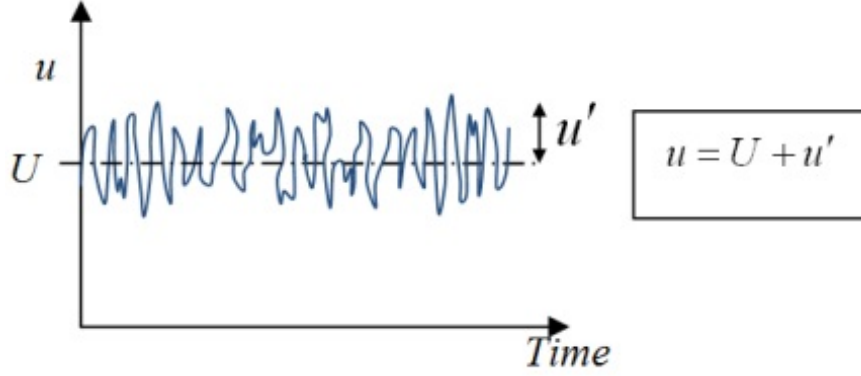
Figure 2.1: The velocity fluctuation in turbulent flows, [2]

The average process is now explained considering compressible flows. Reynolds states that for a turbulent flow[2]

$$u = U + u'$$

Where U is the average velocity and u' is the velocity fluctuation from the average. It follows that

$$U(\vec{x}, t) = \frac{1}{\Delta t} \int_t^{t+\Delta t} u(\vec{x}, t) \, dt$$

Consequently

$$\overline{u'}(\vec{x}, t) = \frac{1}{\Delta t} \int_t^{t+\Delta t} u'(\vec{x}, t) = 0$$

The problem with the Reynolds average is that, for example, in the continuity equation the mass conservation is not guaranteed. To solve this problem Favre introduced a new concept of average

$$\overline{\rho(\vec{x}, t)} \tilde{u}(\vec{x}, t) = \overline{\rho(\vec{x}, t) u(\vec{x}, t)} = \frac{1}{\Delta t} \int_t^{t+\Delta t} \rho(\vec{x}, t) u(\vec{x}, t) dt$$

The velocity is now

$$u(\vec{x}, t) = \overline{u}(\vec{x}, t) + u''(\vec{x}, t)$$

In this case the average of s'' is not zero in the time but

$$\overline{\rho(\vec{x}, t) u''(\vec{x}, t)} = \frac{1}{\Delta t} \int_t^{\Delta t} \rho(\vec{x}, t) u''(\vec{x}, t) dt = 0$$

Applying the Favre average, in the Navier Stokes equation new terms come out, for example in the momentum

$$-\overline{\rho u_i'' u_j''} = \mu_T \left(\frac{\partial \tilde{u}_i}{\partial x_j} + \frac{\partial \tilde{u}_j}{\partial x_i} \right) - \overline{\rho} \tilde{k} \delta_{ij}$$

A focus on the turbulent viscosity can be found in the section 2.6 on page 12 [15]

---

[2]   In the treatment the velocity in the x direction is used, but it is valid for all the variables.

The theory behind the boundary layer could be very difficult to understand and the aim of this thesis is not to explain the boundary layer theory. Thus in this section will be developed the theory for a plate at zero pressure gradient because is a very simple case in which are present all the characteristic of the boundary layer and its particular geometry introduces useful simplification in the treatment.

When a fluid meets a surface a boundary layer will form. In this very thin region the viscosity ν plays a very important role. Since the viscosity effect is very high in the boundary layer, the fluid is laminar and strong velocity gradient will be generated and consequently high stresses will be formed. It's possible to define the Reynolds number close to the wall. In the boundary layer the Reynolds number will be low by consequence of the strong viscous stresses.
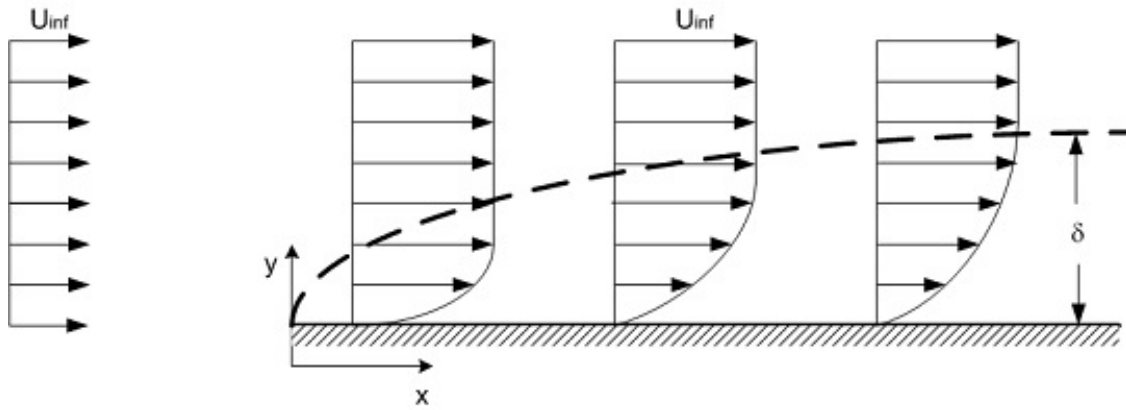
Figure 2.2: Schematic of the boundary layer on a zero incidence flat plate, [16]

As can be seen in the figure 2.2, the undisturbed flow arrive with a homogeneous velocity field, but by increasing the x the boundary layer will be generated and its thickness δ will increase.

In reality the boundary layer doesn't exist, in fact the transition from boundary layer to outer flow takes place continuously.

It's possible to estimate the boundary layer thickness by assuming the equilibrium of the viscous forces and the inertial forces. The inertial forces per unit volume are equal to $\rho u \partial u / \partial y$, instead the viscous forces are equal to $\mu \partial^2 u / \partial y^2$, assuming the newtonian stress representation. Regarding the inertial forces, the partial derivation of the velocity have the same order of magnitude of $\rho U_\infty / x$ in a flat plate, thus the inertial forces are in the order of magnitude $\rho U_\infty^2 / x$.

Very close to the wall the velocity gradient will be of the order of U_∞ / δ and the viscous forces of the order of $\mu U_\infty / \delta^2$. Applying the equilibrium of the forces

$$\rho \frac{U_\infty^2}{x} \sim \mu \frac{U_\infty}{\delta^2} \tag{2.2}$$

Solving for δ

$$\delta \sim \sqrt{\frac{\mu x}{\rho U_\infty}} \tag{2.3}$$

The proportionality factors were investigate in the past, in particular for the flat plate the thickness can be expressed as

$$\delta_{99}{}^3(x) = 5\sqrt{\frac{\nu x}{U_\infty}} \tag{2.4}$$

The dimensionless thickness related to the plate length l is

$$\frac{\delta(x)}{l} = \frac{5}{Re}\sqrt{\frac{x}{l}} \tag{2.5}$$

From the equation 2.5, the thickness decrease by increasing the Reynolds number, the limiting case is when Re is very high and the boundary layer vanishes. δ is also proportional to the $\sqrt{x}$, this means that the thickness grows during the crossing of the plate [16].

2.2.1 Boundary Layer on an Airfoil

By dealing with a complex geometry such as an airfoil, additional pressure forces occur. At the beginning, the laminar boundary layer is formed; by increasing the x, that represents the characteristic problem length, the Reynolds number increases and also the boundary layer thickness grows. At a certain distance x_{crit} the laminar-turbulent transition happens. The outer external inviscid flow imposes the pressure distribution on the wall. So the pressure distribution on the wall is identical to the outer pressure distribution. Some difference in the pressure distribution could occur due to compensation of the centrifugal forces. Also for the turbulent boundary layer
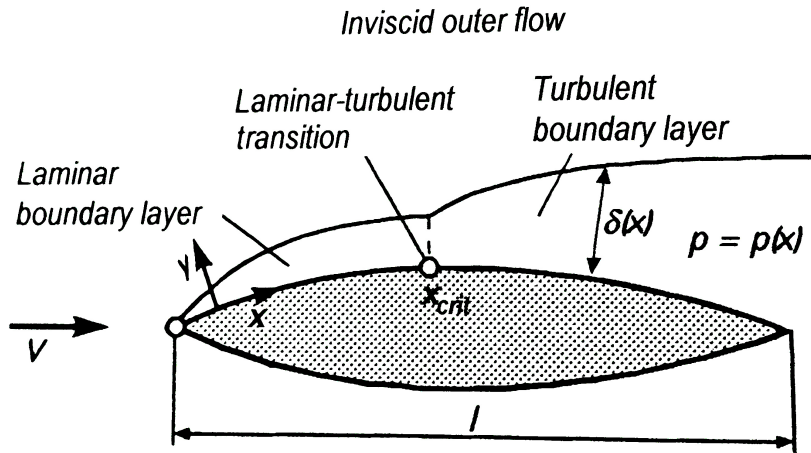
Figure 2.3: The boundary layer development on an airfoil, [16]

the thickness $\delta(x)$ increases by increasing the x, while the wall shear stress decreases.
Since the Reynolds number is a function of the main velocity V and characteristic length, the limiting case is when the $Re \rightarrow \infty$, in which the the boundary layer thickness tends to zero.

---

[3]   The thickness has the subscript 99 because, as said before, the exact boundary layer end doesn't exist.

The outer pressure distribution is of considerable importance in the formation of the boundary layer. The laminar-turbulent transition is influenced by the outer pressure distribution. If the pressure increases considerably along the airfoil, it is possible that the boundary layer detaches from the wall, this argument is treated in the section 2.7 [16].

2.3 Thermal Boundary Layer Without Coupling of the Velocity Field to the Temperature Field

As the velocity boundary layer also the temperature boundary layer will form during the flow movement. It can also be seen that the thermal boundary layer has a characteristic behaviour at high Reynolds numbers, i.e. the temperature field can also be divided in two regions: one region close to the wall, where the thermal conductivity λ plays a role, and a region in which λ can be neglected. If both boundary layers exist also a mutual coupling can be observed.

In the first case (λ that plays a role) the fluid properties ρ and μ can be considered constant, by assuming the independences of these two properties from the temperature and pressure. This assumption is justified by the fact that the pressure and the temperature variation are negligible in the boundary layer.

The energy equation can be written in the following form[4]:

$$\rho c_p \left(u \frac{\partial T}{\partial x} + v \frac{\partial T}{\partial y} \right) = \lambda \left(\frac{\partial^2 T}{\partial x^2} + \frac{\partial^2 T}{\partial x^2} \right) + \Phi \tag{2.6}$$

Where Φ can be expressed as:

$$\frac{\Phi}{\mu} = 2 \left[\left(\frac{\partial u}{\partial x} \right)^2 + \left(\frac{\partial v}{\partial y} \right)^2 \right] + \left(\frac{\partial v}{\partial x} + \frac{\partial u}{\partial y} \right)^2 \tag{2.7}$$

The equation 2.6 shows that a convective change in temperature is possible via conduction (laplacian) and dissipation (Φ). Since the components of the velocity u and v are in the 2.6 and 2.7 means that velocity field must be known to calculate the temperature field.

The Prandtl number is a very important physical property (defined as ν/a) because characterises the boundary layer thickness. It is defined as the ratio between two quantities that characterise the transport properties of the fluid with respect to the momentum (kinematic viscosity) and with respect to the heat (thermal diffusivity). If the transport of momentum is high with respect to the heat transfer transport, the thickness of the velocity boundary layer δ will be relatively tight and vice versa the thermal boundary layer thickness will be large δ_{th} ($Pr << 1$), figure 2.4 on the next page.

---

[4] The following relations are only 1D in order to not overload the explanation.

a) $Pr \rightarrow 0$ (Liquid metals)
b) $Pr \rightarrow \infty$ (Liquids, oils)
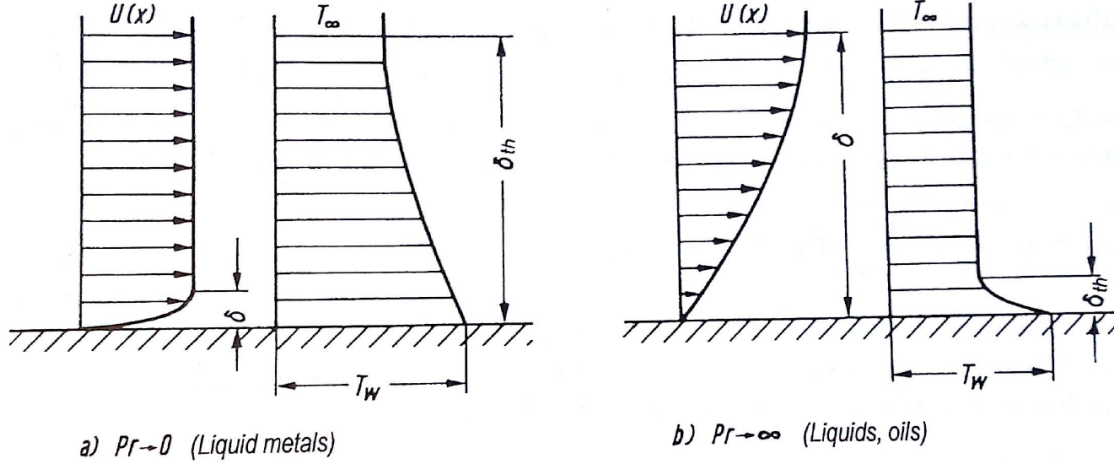
Figure 2.4: Schematic of the thermal and velocity boundary layer for different Pr number, [16]

In the thesis context, the flow was modelled as ideal gas and usually the gas has a $Pr = 1$ [16].

2.4 Thermal Boundary Layer With Coupling of the Velocity Field to the Temperature Field

Until now, physical properties-such as ρ, μ, c_p and λ were assumed constant, it follows that the velocity field was independent of the temperature field. In general cases, these physical properties are a function of temperature or pressure, even if for most of the applications they can be considered as a function of the temperature.

By considering a linear relation between the properties and the temperature, the calculation of the boundary layer is simplified. This is a good approximation if the the heat fluxes are moderate.

In the simulations the fluid is assumed as an ideal gas, it follows that

$$\frac{P}{\rho} = RT \tag{2.8}$$

In the simulation setup it is also assumed that

$$c_p = const, \quad c_v = cons, \quad \gamma = const \tag{2.9}$$

By dealing with gases, the Prandtl number is close to unity.

The viscosity $\mu(T)$ and the thermal conductivity $\lambda(T)$ depend on the temperature and it is possible to use some relations to calculate these quantities, such as

$$\frac{\mu}{\mu_r} = \left(\frac{T}{T_r}\right)^{\frac{2}{3}} \frac{T_r + s}{T + s} \tag{2.10}$$

Where μ_r is the values of the physical quantity evaluated at the reference state. s is a constant that depends on the gas, for air $s = 110K$ [16].

2.5 Laminar To Turbulent Transition

The prediction of the transition from laminar to turbulent flow is one of the most difficult problems in boundary layer modelling. The first man that investigates this phenomena was Reynolds in 1883. The Reynolds number is defined as

$$Re = \frac{Inertial\ Forces}{Viscous\ Forces} = \frac{\rho uL}{\mu} \tag{2.11}$$

The Reynolds number is the ratio between the inertial forces and the viscous forces. When the Reynolds number is higher than one it means that the inertial forces dominate the system thus the flow will be turbulent, in the other case the viscous forces play the main role and the flow will be laminar. There is a range of Re in which the flow is neither turbulent nor laminar, the flow is in transition.

The phenomenon that leads to the transition is the instability of the flow which is always upstream of the transition point. The disturbance between the point of instability where the Reynolds number equals the critical value and the point of transition depends on the degree of amplification of the unstable disturbances.
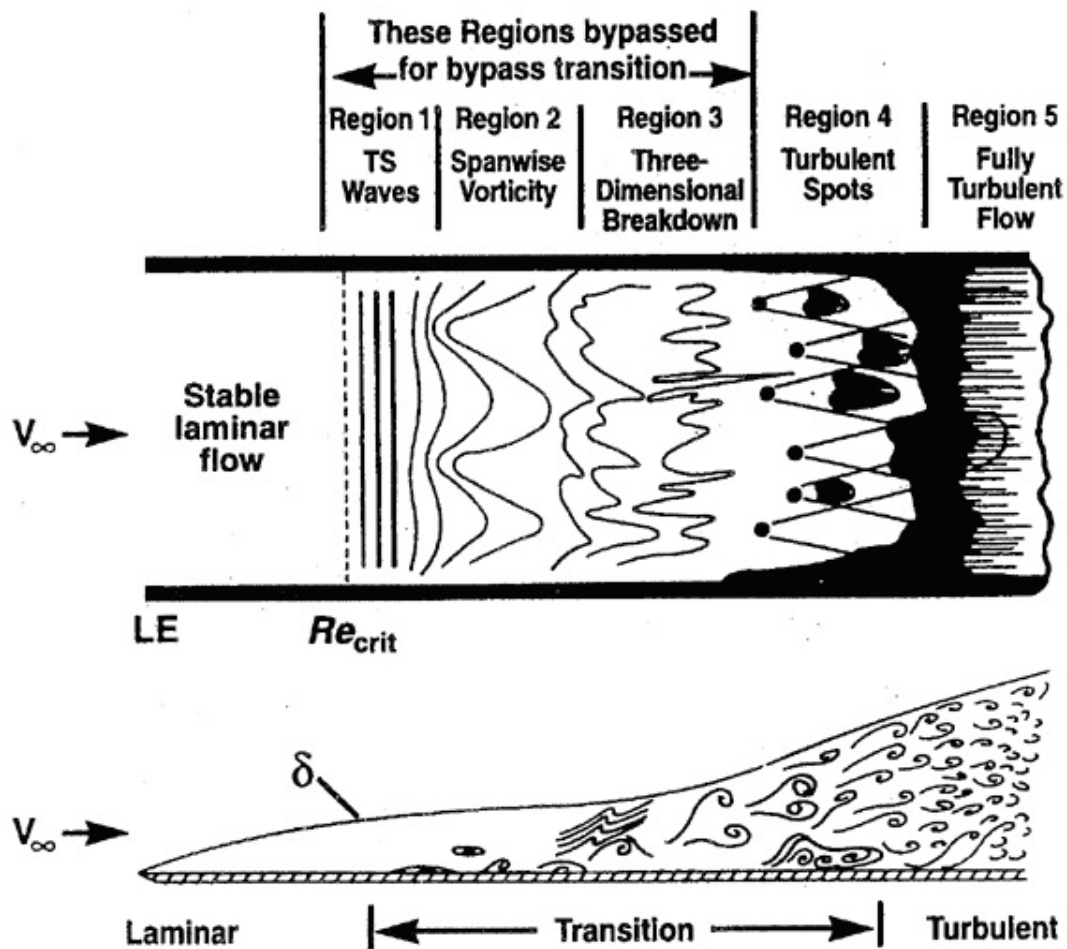
Figure 2.5: Plan view sketch of transition processes in boundary layer flow over a flat plate, [16]

An example is very useful to describe the transition phenomenon, Figure 2.6. The case is the flat plate invested by a laminar flow. In this particular case there is a finite region of Re numbers around Re=1000 where the disturbance are amplified. The precise sequence of events is sensitive to the level of disturbance of the incoming flow. If the incoming flow is laminar numerous experiments confirm the predictions of the theory that initial linear instability occurs around Re=91000. The two-dimensional disturbances are called Tollmien-Schlichting waves, region 1 in 2.5 on the previous page. These disturbance are amplified in the flow direction.

The subsequent development depends on the amplitude of the waves at maximum amplification. Since the amplification takes place over a limited range of Re, it is possible that the amplified waves are attenuated further downstream and that the flow remains laminar. If the amplitude is large enough a secondary, non-linear, instability mechanism causes the Tollmien-Schlichting waves to become three-dimensional and finally evolve into hairpin Λ-vortices, region 2 in 2.5 on the preceding page. Above the the hairpin vortices a high shear region in induced which subsequently intensifies, elongates and rolls up. Further stages of the transition process involve a cascading

Figure 2.6: Plan view of transition process in boundary layer over a flat plate, [16]

breakdown of high shear layer into smaller units with frequency spectra of measurable flow parameters approaching randomness. Regions of intense and highly localised changes occur at random times and locations near the solid wall. Triangular turbulent spots burst from this locations. These turbulent spots are carried along with the flow and grow by spreading sideways, which causes increasing amount of laminar fluid to take part in the turbulent motion.

Transition of a natural flat plate boundary layer involves the formation of turbulent spots at active sites and subsequent merging of different turbulent spots convected downstream by the flow. This takes place at $Re = 10^6$ [15].

2.6 A Short Introduction to Closure Models for Turbulent Flows

The RANS equations contain unknown variables as a consequence of averaging. In order to close the equation set, these variables need to be supplemented before any solution can be obtained. This problem is known as the *turbulence closure problem*. To close the problem we need a set of mathematical equations which provide the unknowns.

There are two different levels of of modelling: Eddy Viscosity/Diffusivity Models (EVM) (known also as first order models) and the Second-Moment Closure Models (SMC) (known also as Reynolds Stress/fluf models or second order models). The first order models assume that the turbulent flux of momentum, heat and species are directly related to the main flow. In the second-order models the turbulent flux is obtained by solving separate transport equations for each unknown variables.

The EVM are based on the Boussinesq (1877) assumption that the turbulent stresses tensor can be expressed in terms of the mean rate of strain in the same way as the viscous stresses. The same principle is applied also for the flux of species, heat and for other properties. For turbulent stress[5].

$$\tau_{ij}^t = -\rho \overline{u_i u_j} = -\frac{2}{3}\rho\kappa\delta_{ij} + 2\mu_t(S_{ij} - \frac{1}{3}S_{kk}\delta_{ij}) \tag{2.12}$$

Where $S_{ij} = \frac{1}{2}(\frac{\partial U_i}{\partial x_j} + \frac{\partial U_j}{\partial X_i})$ is the mean rate of strain, $\kappa = \frac{1}{2}\overline{u_i u_i}$ is the turbulent kinetic energy, μ_t is the eddy viscosity.

Using the RANS and modelling the turbulence using the eddy viscosity, another equation is required to close the problem and obtain the eddy viscosity. In the kinetic theory of gases the molecular viscosity is proportional to the product of the molecular mean free path and the average speed of the molecules. By analogy the turbulent viscosity can be also expressed as a characteristic turbulence length and velocity scale:

$$\nu_t = \frac{\mu_t}{\rho} \propto Lu \tag{2.13}$$

Where the scales L and u need to be determined.

The logic choice for the u is to use the kinetic energy:

$$u = \sqrt{\kappa} \tag{2.14}$$

With $\kappa = \frac{1}{2}(u_1^2 + u_2^2 + u_3^2)$ that is a measure of the averaged turbulence intensity.

A transport equation for κ can easily be derived, instead defining and providing adequate length scale L is more difficult and uncertain.

The EVMs can be divided in 2 categories: one-equation models and two-equation models.

In one-equation model L is provided using algebraic relations, in the other case a transport equation has to be solved in order to obtain the characteristic turbulent length scale.

In one-equation models a differential transport equation of a product involving the length scale and the turbulence intensity can be solved:

$$\frac{D(\kappa^p L^q)}{Dt} = Pruduction\ of\ (\kappa^p L^q) - Destruction\ of\ (\kappa^p L^q) + Diffusion\ of\ (\kappa^p L^q) \tag{2.15}$$

Depending of the choice of p and q the variable can have a physical different meaning. In the past different 'scale providing' variables were tested, but the most popular was the energy dissipation $\epsilon = \nu\frac{\partial u_i}{\partial x_l}\frac{\partial u_i}{\partial x_l}$. Relations between κ and ϵ constitute the $\kappa - \epsilon$ model.

Other models were developed such as the $\kappa - \omega$ which have a better performances in case of adverse pressure gradients and a better prediction of the flow separation. Unfortunately, the ω equation was found to be sensitive to the boundary value of ω at the free edge of turbulent shear layer.

In 1994 Menter proposes to use the robustness of the $\kappa - \epsilon$ and the better performance of the $\kappa - \omega$ combined together the two models, this new model was the SST or *shear stress transport*. The idea

---

[5] The equations shown are valid for incompressible flow in order to simplify the passages.

was to use the $\kappa - \omega$ close to the solid wall and the $\kappa - \epsilon$ away from the wall. The combination of the two models has been accomplished using a *blending function*.

Though the idea seems really simple, the achievement of a successful blending function was not easy and required the use of a number of empirical functions.

Despite the relative complexity and the relative empiricism grade, the SST model has been found to perform well in flow including heat transfer and has been adopted also in *CFX*.

2.7 Separation

When the shape of the body immersed in a flowing fluid it is such that the static pressure increases rapidly in the streamwise direction, a undesirable change in the flow pattern is often observed. The streamlines in the boundary layer near the surface suddenly depart from the surface, this phenomenon is called *separation* 2.7.
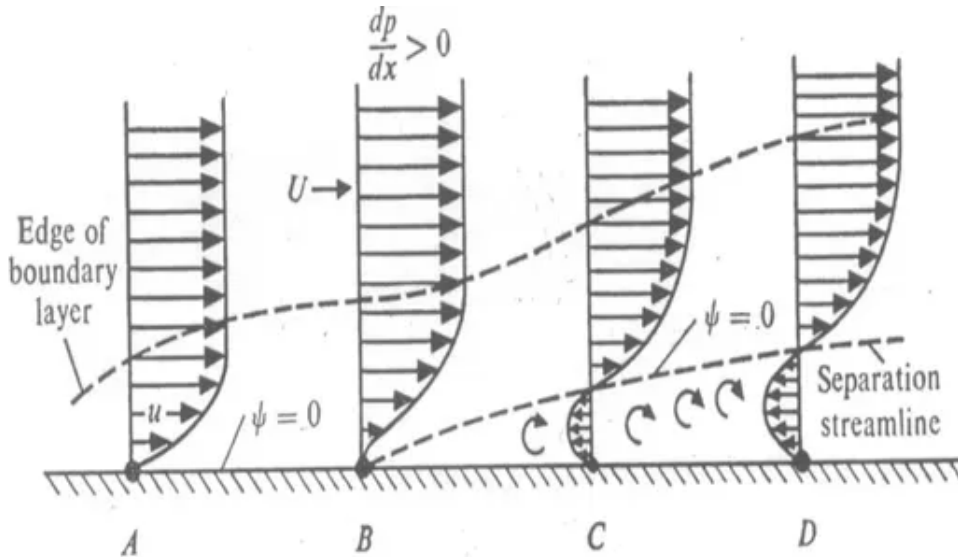
Figure 2.7: The separation phenomenon, [16]

This occurrence is undesirable because the airfoils are designed to have a specific static pressure distribution along the surface in order to produce a certain amount of lift for a wing, for example, and the separation process obviously disturbs the static pressure distribution.

The Bernoulli's equation 2.16 can be used to explain the phenomenon, even strictly applies only to inviscid flows. The solution is not exact, but gives a really clear explication of the problem.

The Bernoulli'e equation states that:

$$u\frac{\partial u}{\partial s} = -\frac{1}{\rho}\frac{\partial p}{\partial s}{}^{6}$$

(2.16)

along a stream line.

As represented in the picture 2.7, the pressure gradient is directed in streamwise direction and also

---

6   In this case, the partial derivation operator is used, but since the approximations enforced also the normal derivation could be used.

must be the same in the layer. Comparing two points, one at the edge of the layer and one well in the viscous layer, the following statement can be written:

$$u\frac{du}{ds} = U\frac{dU}{ds} \tag{2.17}$$

Since the pressure gradients are the same, u is very small compared to U and, because of that, the relation 2.17 points out that a given pressure gradient will produce a much larger change in the velocity at a point in the lower velocity viscous layer than a point in the inviscid flow at the edge. The ratio of the changes will be $U : u$. Since u approaches zero at the wall, a pressure gradient will produce a large Δu in a region where u is already small. The result is, as shown in the picture 2.7 on the preceding page, leading finally to an actual reversal in the direction of the flow. This reversed flow causes an effective obstacle to the upstream flow, so it separate from the original body surface to flow over the *separation bubble* [15].

2.8 Shock and Separation

When a fluid in motion, that can be also subsonic, meets an airfoil, the velocity on the suction side of the aifoil increase due to the geometry. Usually the vanes in jet engines work with a shock; obviously the shock is not a wanted phenomenon, but in order to increase the performances of the engines the pressure ratio between the vanes is such that a shock happens.

As a consequence of the shock, the separation phenomenon could occur, as shown in Figure 2.8.

Figure 2.8: Schematic of the separation due to the shock, [8]

A pressure, temperature and density gradient always occurs due to the shock. There is a total pressure loss that cause the growing of the physical quantities.

Hence, the static pressure increase immediately after the shock leads to a deceleration of the flow. Consequently, the boundary layer becomes susceptible to separation from the wall [8].

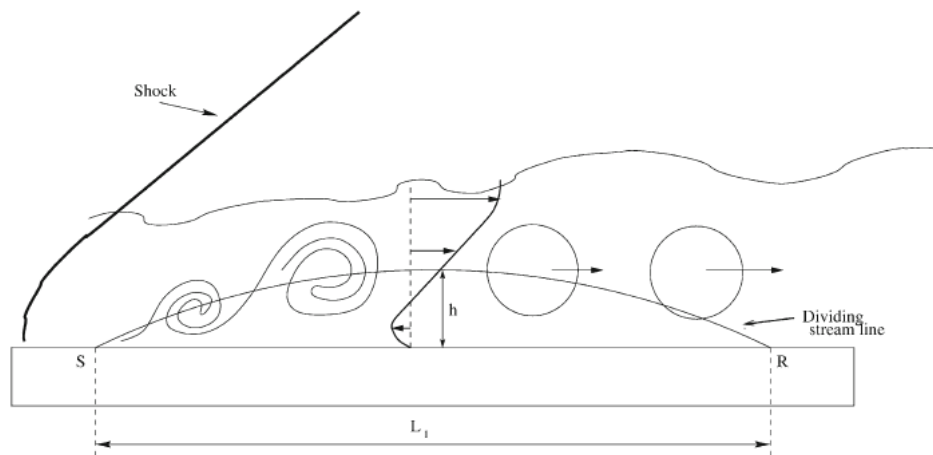## 2.9 The Adiabatic Wall Temperature

The adiabatic wall temperature, sometimes referred to as the recovery temperature, is the temperature of a surface perfectly insulated on its back side. This temperature may be explained in the following way. Since the velocity at the wall must be zero, the speed of the flow is damped by viscous forces. This results in a velocity gradient across the boundary layer. The temperature of the air near the wall is increased by viscous dissipation. In an adiabatic system no heat is transferred through the body itself; however, the rise in temperature of the wall above the main flow temperature causes conduction of heat back through the gas layers near the wall into the bulk stream. Consequently, the wall assumes a temperature value which is referred to as the adiabatic wall temperature. The adiabatic wall temperature is used in the section 2.12 on page 19. The equation

$$q_x = h(T_w - T_\infty) \tag{2.18}$$

for slow-speed flows or, in general, no-friction flows is a valid tool to evaluate the convective heat exchange, but in other cases loses all the meanings because the high-speed flows have high kinetic energy that in the laminar layer is dissipated into heat. Therefore, the energy dissipation is due to the term $\mu\left(\frac{\partial u}{\partial x}\right)^2$ (written in the laminar flow case).

The kinetic energy of the isentropic flow can be found in the difference between the stagnation temperature and the static temperature:

$$T_{kinetic} = T_t - T = \frac{V^2}{2c_p} \tag{2.19}$$

If the wall is adiabatic the temperature that the wall attains at steady equilibrium will depend on how much the kinetic energy is recovered on the wall.

This quantity is expressed as a recovery factor r, defined as

$$T_{aw} = T_\infty + r\frac{U^2}{2c_p} \tag{2.20}$$

The value of r is generally less than, but near, unity for gases.

In general the recovery factor can be expressed as $r = \sqrt{Pr}$ for laminar flows and $r = \sqrt[3]{Pr}$ for turbulent flow. The air has a Prandtl number about one which is the case in this work [15].

2.10 Sensitivity

The results of a simple simulation show the values of a certain quantity, but there are no information about the possible scenario that could happen if the external variables would change. The sensitivity is a parameter that gives useful information about the most affected zone by a variation of a parameter.

The objective here is to determine the output of the solver with respect to the input. The mathematical formulation is:

$$\frac{y_i}{x_i} = \frac{y(x_k + \Delta x_k) - y(x_k)}{\Delta x_k} + O(\Delta x_k) \tag{2.21}$$

Knowing these gradients or sensitivities helps to better design experiments and computations. [13] The advantage of this formulation is that it is conceptually simple and requires only a simple *Matlab* code to be calculated. To obtain N sensitivities $N + 1$ simulations are required.

In Figure 2.9 is represented an example of the sensitivity plot [13]. In the figure the temperature contour is shown, whilst in the figure b the influence of the inlet temperature T_i on the wall temperature can be observed.
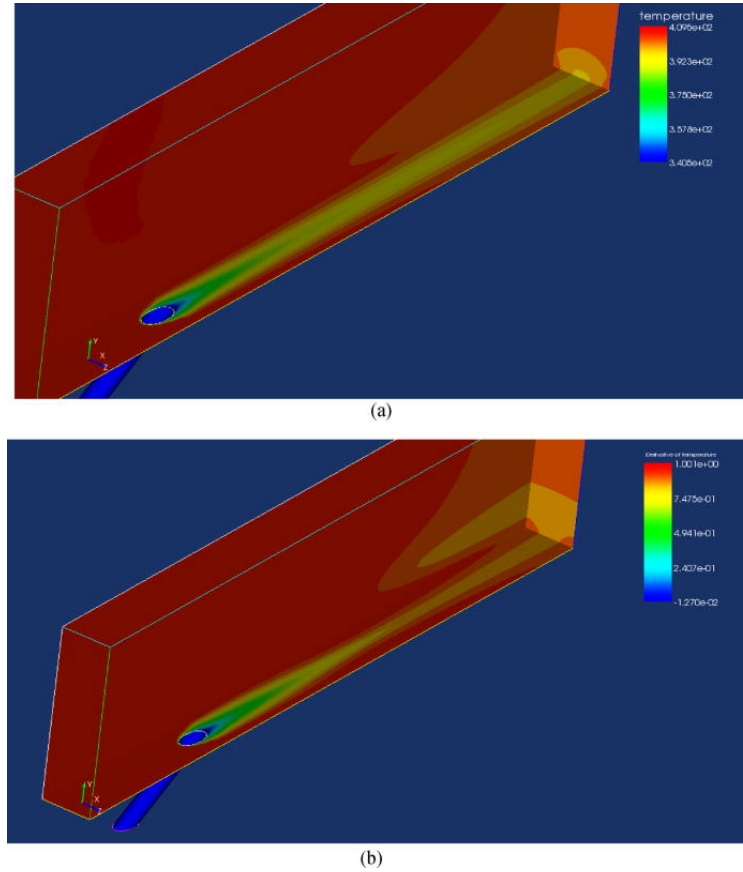
Figure 2.9: Sensitivity to hot gas inlet temperature T_i (a) Contours of a temperature on the domain boundaries (b) contours of $\frac{\triangle T}{\triangle T_i}$, [13]

The sensitivities contours are created exporting the values of the physical quantity, such as the heat flux, for two desired simulations and than applying equation 2.21 for each node of the surface. As indicated in Figure 2.10 few steps are required in order to perform the analysis in the best way. Using CFX the simulations are obtained, subsequently in CFD Post the contour of the areas of interest is exported as csv file. The csv files are, then, imported in Matlab and with a Matlab Code the sensitivities are calculated applying equation 2.21 and organised in the proper txt files. At this point the txt files are imported in CFD Post in order to capture the pictures. The final step is the visual analysis of the pictures and the research of the similitudes with respect to the other cases.
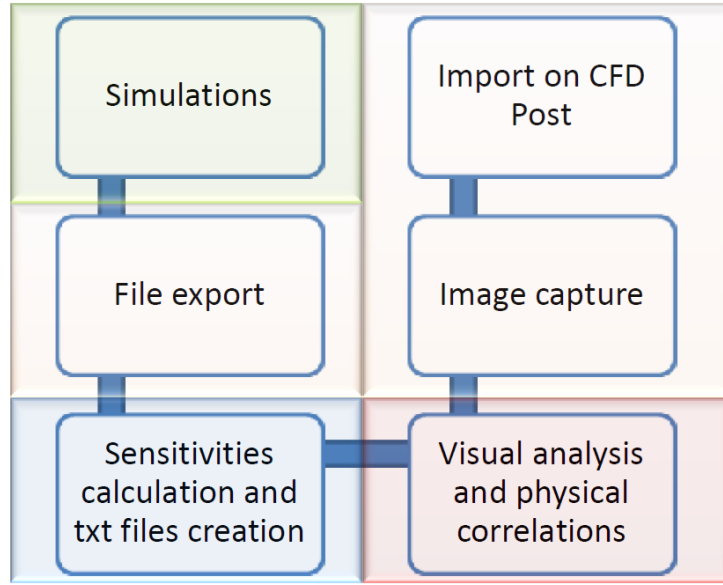
Figure 2.10: Flow chart of the sensitivity analysis

2.11 Film Cooling Performance

Film cooling is a major component of the overall cooling of turbine airfoils. Holes are placed in the body of the airfoil to allow coolant to pass from the internal cavity to the external surface. The ejection of coolant gas through holes in the airfoil body results in a layer or film of coolant gas flowing along the external surface of the airfoil. Hence, the term "film cooling" is used to describe the cooling technique. Since this coolant gas is at a lower temperature than the mainstream, the heat transfer into the airfoil is reduced. The adiabatic effectiveness has a predominant effect in the design of the overall airfoil cooling. Consequently, in this section details of film cooling performance are reviewed.

The primary measure of film cooling performance is the adiabatic film effectiveness, η, since this has a dominating effect on the net heat flux reduction.

$$\eta = \frac{T_{aw} - T_\infty}{T_{c,out} - T_\infty} \tag{2.22}$$

The adiabatic effectiveness is a parameter that rates the cooling potential that remains along a surface downstream of film cooling holes.

Another important parameter to evaluate the film cooling is the overall effectiveness

$$\phi = \frac{T_w - T_\infty}{T_c - T_\infty} \tag{2.23}$$

The overall effectiveness gives information on how much of the available cooling power is used.

Ideally a film of coolant would be introduced to the surface of an airfoil using a slot angled almost tangential to the surface in order to provide a uniform layer of coolant that remains attached to

the surface. However, long slots in the airfoil would seriously reduce the structural strength of the airfoil, and hence are not feasible. Consequently, coolant is typically introduced to the airfoil surface using rows of holes. The film cooling performance is dependent on the hole geometry and configuration of the layout of the holes. Furthermore, various factors associated with the coolant and mainstream flows, and the airfoil geometry, also significantly affects the cooling performance.

The blowing ratio, M, is the ratio of the coolant mass flux to the mainstream mass flux and is defined as follows:

$$M = \frac{\rho_c u_c}{\rho_\infty u_\infty} \tag{2.24}$$

where ρ_c and ρ_∞ are the coolant and mainstream density, respectively, and u_c and u_∞ are the coolant and mainstream velocity, respectively [5].

2.12 htc Calculation

As mentioned in the section 1 on page 1, the performance of modern gas turbine engines is strongly dependent on the maximum cycle temperature. Since the goal is to increase the turbine entry temperature, values of TET much higher than the melting limits of the vane metal are common in modern engines. Thus, accurate prediction of the heat flux and the temperature distribution is important. Normal practice for heat transfer calculations in gas turbines is to calculate external and internal htc distributions from separate CFD calculations and then solve FEM calculation using as boundary condition the external convective heat flux.

(a) *Relation between heat flux and wall temperature* **(b)** *Schematic of the linear (solid line) and non-linear (dashed line) behavior of the htc*

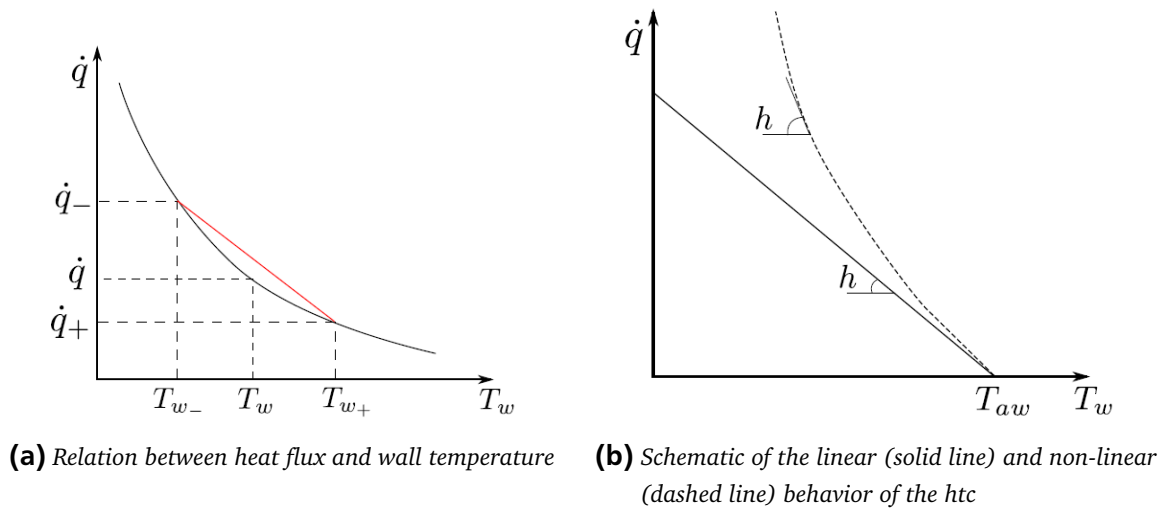**Figure 2.11:** The htc comportment and its approximation, [12]

This know-how is based on the hypothesis that aerodynamics fully determines heat transfer so that the imposed solid-side thermal boundary condition does not affect the htc. However, a two-way interaction between fluid and solid happens in reality. So that when the designer is dealing with internal cooling and film cooling the htc prediction could be distorted.

Despite the increasing popularity of coupled simulations, the classic method is still employed.
In the classic approach the approximation of a non-dependence of the htc with respect to the wall temperature is applied, but the two-way interaction clearly shows that it's not true.
The picture 2.11a on the previous page shows a presumable heat flux trend with respect to the wall temperature. Instead the picture 2.11b on the preceding page evinces the difference of the method that will be explained in the section 2.12.1.

2.12.1 Classic Method

The linear htc is used to simulate the convective heat exchange between the solid and the fluid. Usually it is calculated using a CFD simulation, but there are also empirical models. Mathematically the model can be represented in the equation 2.25

$$\dot{q} = h(T_w - T_{aw}) \tag{2.25}$$

where T_w is the wall temperature and T_{aw}[7] is the adiabatic wall temperature. This method implies that possible wall temperature dependence of the htc is neglected. This is not completely true, as shown in the 2.12.2, but it's used because it's robust and easy to implement.

2.12.2 3-Point Method

In his paper Maffulli [12] has performed a systematic study on the effect of the temperature ratio T_w/T_g on the heat flux. This investigation revealed a clear relation between the htc and the wall temperature, Figure 2.12. It can be seen that in the stagnation point region, the effect of the temperature ratio is less pronounced than in the zones close to the trailing edge. This indicates the influence of the history effect in the boundary layer. At the leading edge, where the boundary layer has just been formed, the effect of wall temperature is minimal, but it increases considerably as the boundary layer develops over the blade surface.

---

[7]   The adiabatic wall temperature is obtained running a simulation without the solid domain and using an adiabatic wall boundary condition.
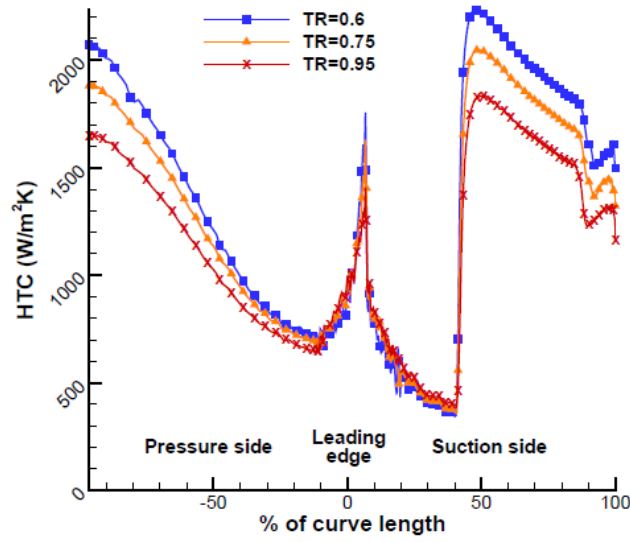
Figure 2.12: Dependency of the htc on the wall temperature, [12]

In order to evaluate the htc taking into account the wall temperature dependence the new method proposed by Maffulli is used. The mathematical formulation can be written as in Equation 2.26:

$$\dot{q} = h(T_w)[T_w - T_{aw}] \tag{2.26}$$
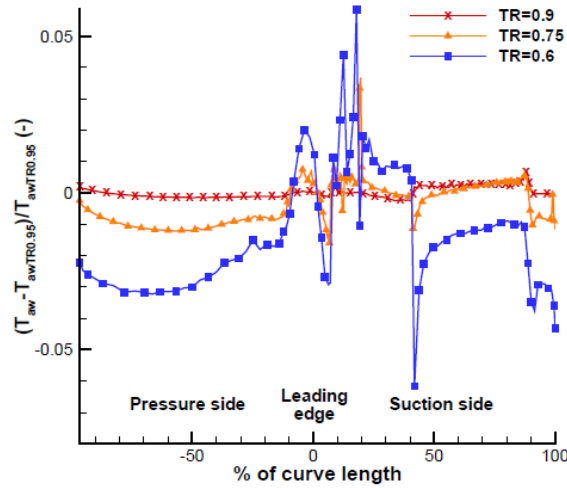
Figure 2.13: Dependency of the T_{aw} distribution on the fluid wall temperature ratio, [12]

Using this formulation, a wall temperature dependence of the adiabatic wall temperature can be seen, but in accordance with Figure 2.13 this dependence can be neglected because it leads to a very small error.

At this point, using the non-dependence hypothesis between T_w and T_{aw} , the new formulation is represented in Equation 2.27.

$$\dot{q} = (h_0 + h_1 T_w)(T_w - T_{aw}) \tag{2.27}$$

Where h_0 is the htc referred to 0 K and h_1 is a constant. This equation involves the linear relation of the htc with respect to the wall temperature.

h_0, h_1 and T_{aw} are the unknowns, which are all function of the spatial position. Reorganising the unknowns as follow:

$$C_1 = -h_0 T_{aw}$$

$$C_2 = h_0 - h_1 T_{aw}$$

$$C_3 = h_1$$

a system composed by 3 equations is required.

$$\begin{cases} \dot{q}_1 = C_1 + T_{w1}C_2 + T_{w1}^2 C_3 \\ \dot{q}_2 = C_1 + T_{w2}C_2 + T_{w2}^2 C_3 \\ \dot{q}_3 = C_1 + T_{w3}C_2 + T_{w3}^2 C_3 \end{cases} \tag{2.28}$$

To solve this system and find the three unknowns, an equal amount of simulations is required. The simulations are uncoupled and with a constant wall temperature as boundary condition.

Now the linear system can be solved. This operation must be done for each node of the mesh and, because of that, a distribution of the 3 unknowns can be imposed in a FEM solver, for example.

The proposed method requires three calculations at different wall temperatures to predict accurately htc levels at any desired wall temperature. With only 50% extra computing cost compared to the conventional way for htc calculations, the proposed method would allow for an easily usable correction on the htc-T_w dependence, leading to a much enhanced accuracy, as clearly and consistently shown for the present test cases [12].

2.13 CFD Simulations

CFD, (Computational Fluid Dynamics) is the analysis of systems including fluid flow, heat transfer and associated phenomena such as chemical reactions by means of computer-based simulations. The power of this computational analysis is very high and finds a role in a wide range of industrial and non-industrial application areas. From 1960s onwards the aerospace industry has integrated CFD techniques into the design of aircraft and jet engines. More recently, CFD simulations has been applied to the design of internal combustion engines.

The analytical solution of the Navier-Stokes equations has been found only in rare cases and, sometimes, with strong approximations. CFD simulations can solve the equations by splitting the domain into smaller regions in which the equations are solved. Hence, a mesh is produced. The dimensions and the characteristics of the grid are important to reduce numerical errors.

The simulations of fluid dynamic problems are not easy to conduct. For example, the simulations of complex turbulent flows are demanding regarding the computational power. The modern computers are not powerful enough to manage the turbulent flows with high Reynolds number. Since the computational time is strictly linked to the increase of the Reynolds number and most of the technical problems work with complex geometries, a direct solution of the Navier-Stokes equation would require a huge amount of time. To overcome this problem, the simulation of the turbulence has evolved into modelling of the turbulence. This means that the attention is now focused on the effects of the flow accepting a non-perfect solution. The model of the turbulence used in this work is based on the RANS or Reynolds Averaged Navier-Stokes Equations. In the RANS equations the velocity of the particles is split into a mean value and a fluctuation value. Averaging the equations, a new term appears in the equations. That term is called the Reynolds stress term and can be modeled using particular turbulence models. The closure models are treated in the section 2.6.

Most of the effort for this thesis was used for CHT simulations or Conjugate Heat Transfer simulations. The popularity of these particular simulations is increased during the last years because the available computer power is increased, too. CHT refers to simulations in which fluid and solid heat transfer is treated in a coupled way.
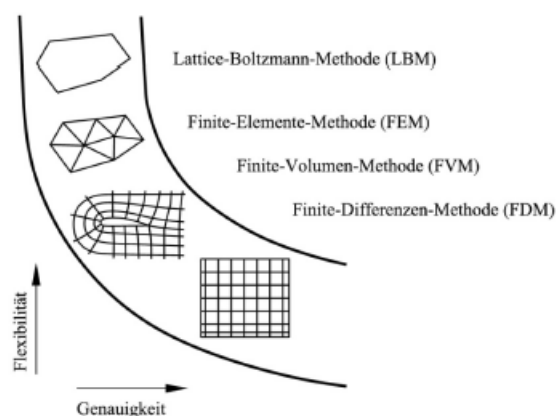

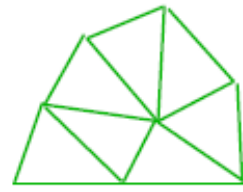**Figure 2.14:** The different type of grid

As mentioned before, the solution of the RANS equations is not possible except for simple cases. The CFD idea is to divide the domain in small volumes with simple geometry in order to solve the equations using the *finite volume method*. This means that the conservation equations of the flow are solved for a discretized rather than a continuous field. There are also other methods of discretization, but the finite volume is the most robust in CFD. The most common discretisation types can be found in Figure 2.14, where they are related in terms of their flexibility and accuracy: the finite element method (FEM), which is relatively flexible but also relatively imprecise and the finite difference method (FDM). These can achieve very high accuracies when used appropriately. It places high demands on the structure and quality of the mesh (high-quality, smooth grids). The finite volume method (FVM) is a middle way between the FEM and the FDM. It uses a derivative of the differential equation system, formulated integrally in physical space. The integral formulation benefits from the flexibility by smoothing and compensating errors and inaccuracies. This is also the reason why FVM is used primarily in numerical flow simulations today.

The first step in the discretisation of a spatial problem volume usually comprises the definition of a suitable grid. In practice, grid generation often proves to be the most time-consuming part of a numerical study, especially as the problem volume is modeled as precisely as possible, but on the other hand the calculation effort is to be minimized, which is directly proportional to the number of grid points. Ultimately, a compromise must be found between these two objectives, in which the user also has to ask the question, what accuracy is required for the calculation, and how much time is planned for grid generation [15].

2.13.1 Mesh Quality

After the grid generation, the obtained mesh must be analysed because the mesh structure influences the results. The stability and the errors are strongly related to the mesh quality. The parameters that ensure the mesh quality are:

- Skewness: The skewness of a grid is an indicator of the mesh quality and suitability. Large skewness compromises the accuracy of the interpolated regions. (see the subsection 2.13.1)

- Smoothness: The change in size should also be smooth. There should not be sudden jumps in the size of the cell because this may cause erroneous results at nearby nodes. (see Figure 2.15)

- Aspect Ratio: It is the ratio of longest to the shortest side in a cell. Ideally it should be equal to 1 to ensure best results. For multidimensional flow, it should be near to one. Also local variations in cell size should be minimal, i.e. adjacent cell sizes should not vary by more than 20%. Having a large aspect ratio can result in an interpolation error of unacceptable. (see Figure 2.16) magnitude.
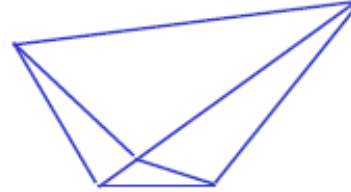
Figure 2.15: Ideal and Skewed triangles, [3]
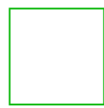
Figure 2.16: Ideal and Skewed triangles, [3]

Skewness

The skewness is the value of how close to the ideal is a face or a cell. The definition of skewness states that the perfect cell has a value of 0, whilst a value of 1 indicates a completely degenerated cell. The figure below shows the difference between a perfect triangle and a high skewed one.
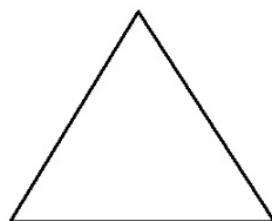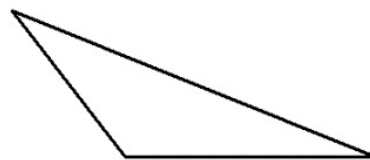
Figure 2.17: Ideal and Skewed triangles, [3]

There are two method to characterise the skewness of a cell: based on equilateral volumes (applies only to triangles and tetrahedra) and based on the deviation from a normalized equilateral angle

(This method applies to all cell and face shapes, e.g., pyramids and prisms). In the equilateral volume deviation method, skewness is defined as

$$Skewness = \frac{Optimal\ Cell\ Size - Cell\ Size}{Optimal\ Cell\ Size}$$

In the normalized angle deviation method, skewness is defined (in general) as

$$max\left[\frac{\theta_{max} - \theta_e}{180 - \theta_e}, \frac{\theta_e - \theta_{min}}{\theta_e}\right]$$

Where θ_{max} is the largest angle in the face or cell, θ_{min} is the smallest angle in the face or cell and θ_e is the angle for an equiangular face or cell (e.g., 60 for a triangle, 90 for a square) [3].

3 Simulation Settings

In this section the different models are introduced paying attention to geometry, mesh and boundary conditions. A mentioned in the introduction, three cases of studies are used.

(a) *Mark II vane* **(b)** *MT1 NGV*
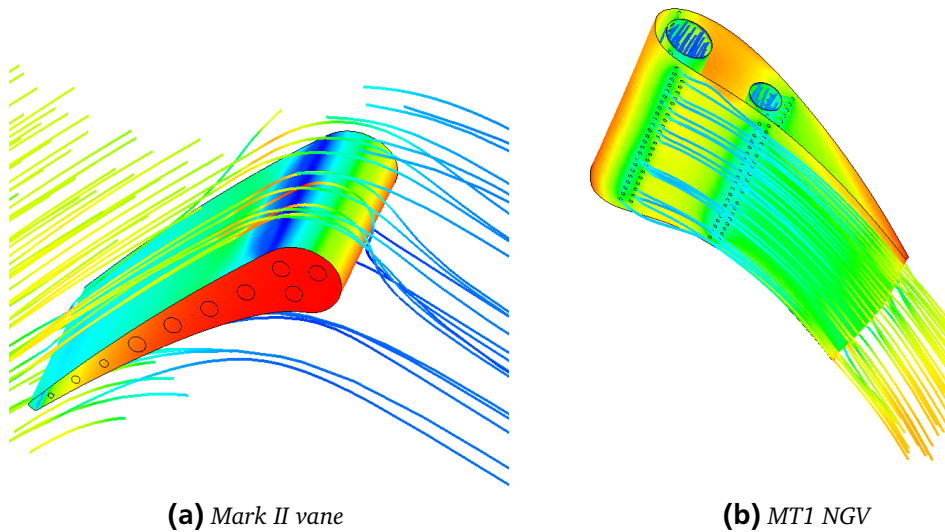
Figure 3.1: The MarkII test case and the MT1 NGV

The pictures 3.1b and 3.1a show two of the three simulation models. The Mark II is a very simple linear vane with constant geometry, moreover ten internal ducts are present to cool the vane. The cooling ducts have a simple geometry, too. In the Mark II case the influence of the internal cooling on the vane internal surface is investigated. In this vane a shock leads to a separation of the fluid.

The MT1 is a more realistic vane. In this case both internal cooling and film cooling are present.Two internal ducts feed the cooling holes with the cooling flow. The findings obtained with the low fidelity test cases are compared with the results of this case.

The film cooling influence is compared with a leading edge model, Figure 3.2. The main flow incidence is zero in this case, this means that the stagnation hole is directly invested by the main flow. The off stagnation holes provide cooling flow, too.
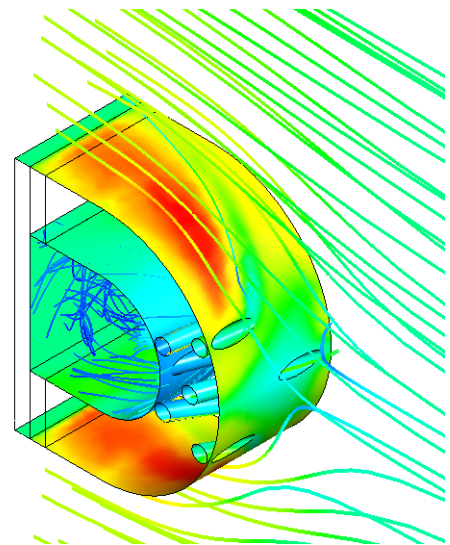
Figure 3.2: The low fidelity leading edge test case

All the meshes used in this thesis were created by J. Hilgert, moreover a mesh sensitivity analysis has been done.

3.1 Mark II

This computational model is based on the experimental and numerical study of Hylton et al. [11]. The model consists of a MARK II vane cooled by air flow through 10 internal cooling tubes. The geometric characteristics are shown in Table 3.1a In order to obtain an overview of the sensitivity

$Setting\ angle\ [deg]$	63,69
$Air\ exit\ angle\ [deg]$	70,96
$Throat\ [cm]$	3,983
$Vene\ heigth\ [cm]$	7,620
$Vane\ spacing\ [cm]$	12,974
$Suction\ Surface\ Arc\ [cm]$	15,935
$Pressure\ Surface\ Arc\ [cm]$	12,949
$True\ Chord\ [cm]$	13,622
$Axial\ Chord\ [cm]$	6,855

(a) Geometric Characteristics

$Flow\ Regime$	Subsonic
$Relative\ Pressure\ [bar]$	3.37
$Turbulence$	Intensity and Eddy Viscosity Ratio
$Fractional\ Intensity$	0,065
$Eddy\ Viscosity\ Ratio$	10
$Total\ Temperature\ [K]$	788

(b) Inlet Boundary Conditions

Table 3.1: Mark II geometry and border conditions, [11]

influence of the external quantities, some values of the inlet boundary conditions are changed. The original setting of the vane is shown in Table 3.1b . The results are compared with the original case that was validated by Hilgert.

To prove the validation the isentropic Mach number and the wall temperature distribution at half span are compared with measured data. In Figure 3.3 on the next page is shown the isentropic Mach number, whilst in the figure 3.4 is shown the temperature distribution.

Since only the variation of the input parameters is planned to be investigated, the outlet and the cooling tubes boundary conditions are kept constant. Hence, the other input parameters are changed in order to obtain the different Mach number or Reynolds number desired.

The solutions for mass momentum, energy and turbulence closure transport equations are solved using ANSYS CFX. The air is modelled as a perfect gas with constant specific heat, thermal conductivity and viscosity.
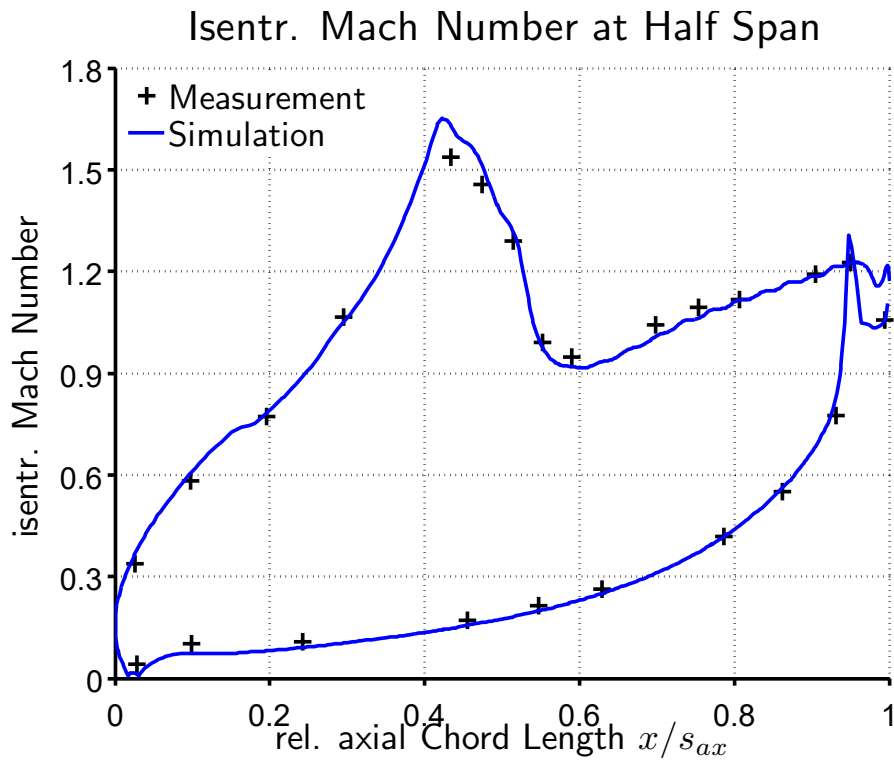
Isentr. Mach Number at Half Span

Figure 3.3: Isentropic Mach number on the vane half span, Hilgert
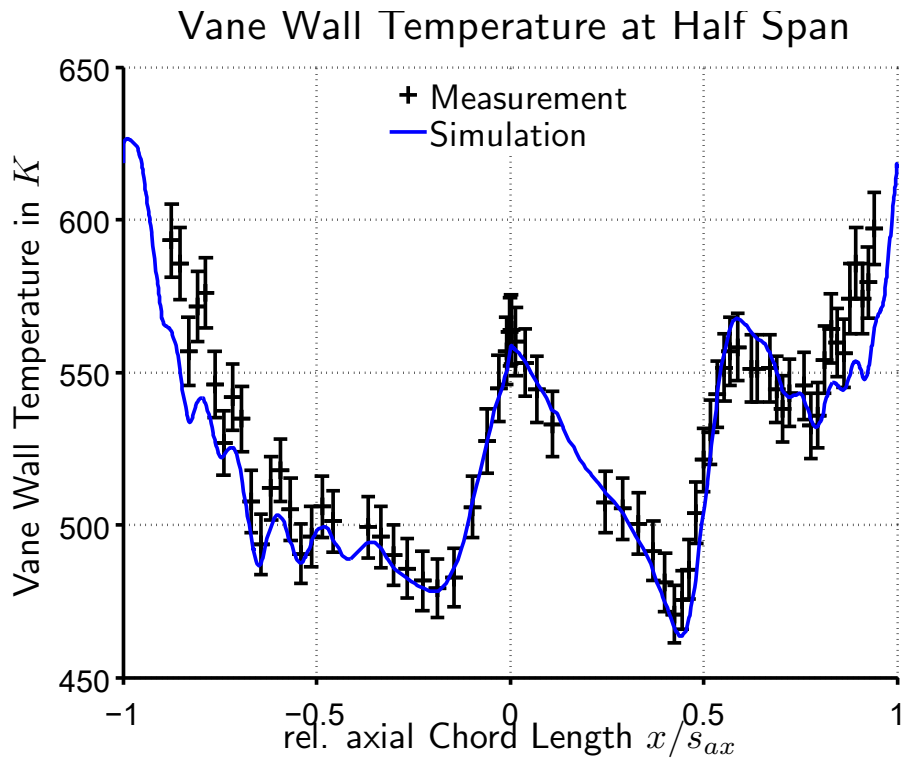
Vane Wall Temperature at Half Span

Figure 3.4: Temperature distribution on the vane half span, Hilgert

The vane material is ASTM 310 stainless steel with constant specific heat capacity while the thermal conductivity was modelled with the following formulation:
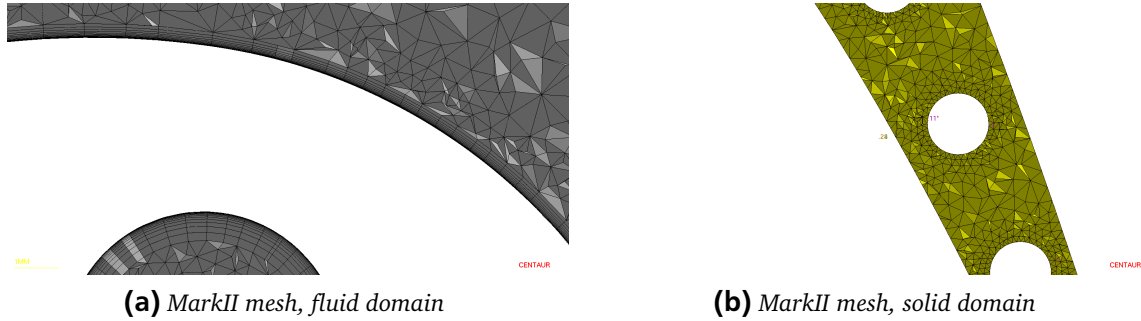
$$\lambda = 6,811 + 0.020176 \cdot Temperature$$

(a) *MarkII mesh, fluid domain*

(b) *MarkII mesh, solid domain*

Figure 3.5: Particular of the solid and fluid domain of the MarkII vane, Hilgert

Centaur Mesh was used by Hilgert to obtain the mesh files. Solid and fluid constitute two different domain. Concerning the solid, figure 3.5b, the number of nodes are 405959 and the number of elements are 1992220. The fluid domain is constituted of 2971547 nodes, 9259130 Elements of which 5305084 tetrahedric elements and 3954046 prismatic elements. In order to simulate in the best way the boundary layer, 20 layers of prism/hex mesh are used close to the vane.

The boundary condition prescribed at the hot gas path inlet are total pressure and temperature, turbulence intensity and eddy viscosity ratio , Table 3.1b. Mass flow rate and static temperatures are prescribed at the inlet of the radial cooling channels. The mesh interface has been set in auto mode in the cases of the solid-fluid interface. Moreover a periodic boundary condition with 1:1 nodal connectivity along the mid pitch interface in order to simulate an infinite cascade is specified. The Shear Stress Transport (SST) turbulence model is used in order to perform better in case of adverse pressure gradient and reproduce better the separation. In Figure 3.2 on the next page are shown the different boundary conditions.

In general, the figure 3.6 indicates boundary layer separation an re-attachment starting at about 20% of the arc length due to strong adverse pressure gradients. In his paper Hylton compared the different results obtained changing the Re and the Mach number. From this test comes out that the separation and re-attachment are strongly influenced by the Mach Number as well as the quantities such as the htc, figure 3.8. Whilst, the influence of the Re is negligible, figure 3.9. This observation gives some support to the contention that the large variations in suction surface quanti-

Figure 3.6: Shock and separation in the Mark II case

ties are caused by separation/re-attachment phenomena rather then simple transition behaviour.

Figure 3.7: MarkII boundary conditions
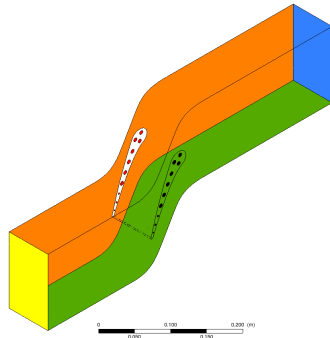
🟦	Main Flow Inlet
🟨	Main Flow Outlet
🟩	Periodic
🟥	Coolant Inlet
⬛	Coolant Outlet
🟧	Adiabatic Wall[a]

Table 3.2: MarkII boundary conditions

[a] The BCs of the uncolored surfaces are those in front of them
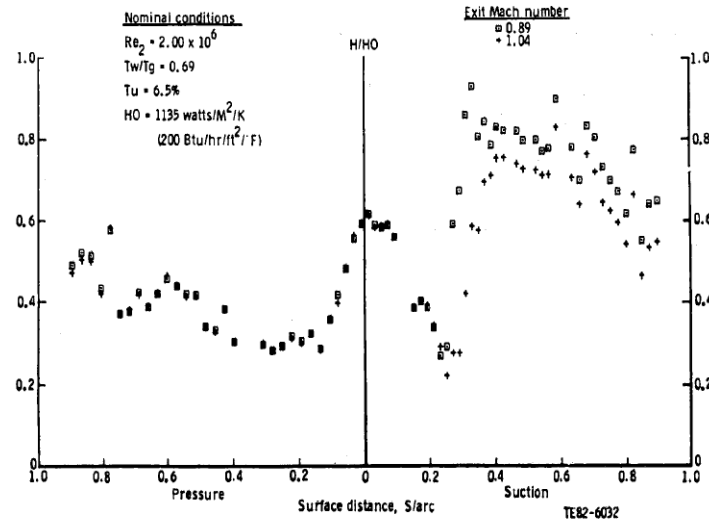
Figure 3.8: Effect of The Exit Mach Number on the htc distribution on the Mark II Airfoil, [11]

Because of these considerations the separation/re-attachment zone have to be the most susceptible, so that the highest values of the sensitivity must be in this zone. Obviously, the highest values of the sensitivity have to occur for the Mach number variation, instead very small values are expected for the Reynolds number change.

In Figure 3.10 on the next page the htc distributions for different wall temperature/inlet gas temperature ratio are represented . A very similar trend can be seen in the figure 4.8 on page 46 in the section 4.2.

Figure 3.9: Effect of The Exit Reynolds Number on the htc distribution on the Mark II Airfoil, [11]

Figure 3.10: Effect of the T_w/T_g ratio on the htc distribution on the Mark II Airfoil, [11]

3.2 Leading Edge Model

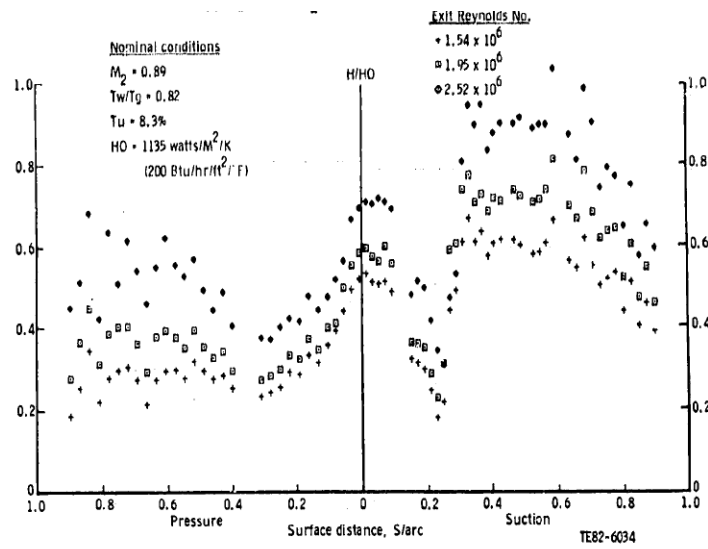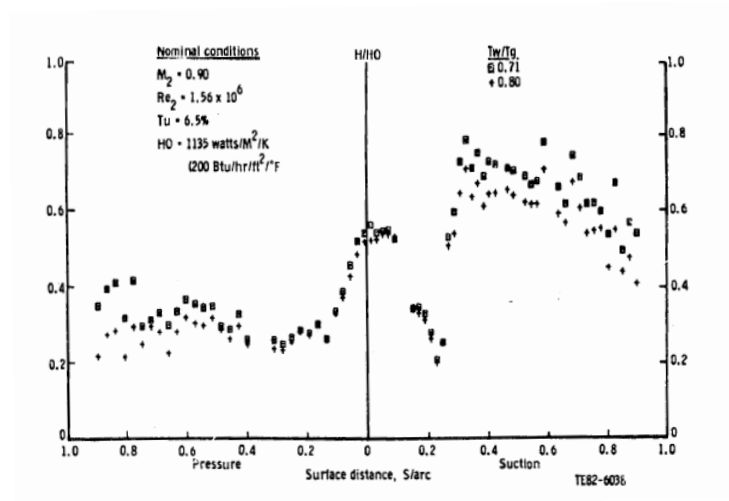The model used for this purpose was the same used by Ravelli et al. [14] as indicated in the figure
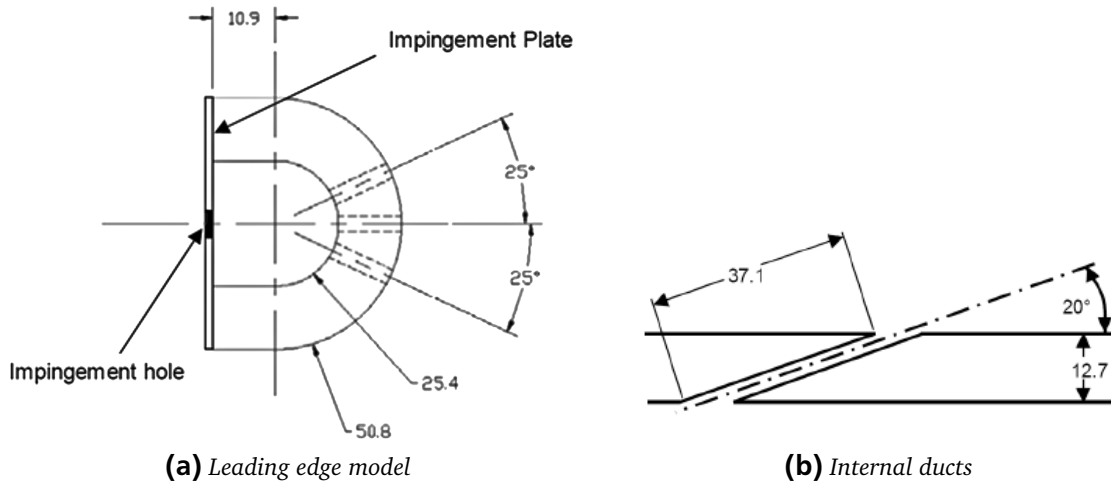3.11a. Furthermore, the mesh file and the Pre file were generated by Hilgert. The dimensions of

(a) *Leading edge model*   **(b)** *Internal ducts*

Figure 3.11: Leading Edge Model, [14]

the model are: the outer diameter and the inner diameter are respectively 50.8 mm and 25.4 mm,
the film cooling configuration included three rows of holes positioned along the the stagnation
line and at $\pm 25^o$ from the stagnation line, the diameter of each hole is $d = 3,15mm$, the hole are
angled from the surface of an angle of 20° and oriented normally to the flow direction (Figure
3.11b), the hole-to-hole pitch is $p = 24,2mm$ resulting in a $p/d = 7,7$, the impingement plate is
10.9 mm far from the cylindrical part and the impingement hole is $d_{ip} = 5mm$. Considering the
impingement plate, it is 3,18 mm thick.

d_{hole}	d_{outer}	d_{inner}	p	$\frac{p}{d}$	imp	d_{ip}
3.15 mm	50,8 mm	25,4 mm	24,2 mm	7,7	10.9 mm	5 mm

Table 3.3: Leading edge model dimensions recap

The CFD analysis is carried out by means of ANSYS CFX. The SST turbulence model is selected
and the Gamma-Theta model is used to simulate the transition. The air is modelled as perfect gas
with constant specific heat, thermal conductivity and viscosity. Different mesh regions are created
in order to simulate the fluid, the glue, the impingement plate and the solid. The solid material is
a PC 287 with molar mass of 250 $kg\ kmol^{-1}$, density of 1190 $kg\ m^{-3}$ and constant specific heat
capacity $0,35\ BTU\ lb^{-1}$. The impingement plate material is Aluminium and the glue is modelled
with the same properties of the solid. The boundary conditions are summarized in the figure 3.4
The meshes used consist of 1609571 nodes and 7639501 elements (6873837 tetrahedra, 2891
prism and 762773 Wedges) in the fluid domain, 90564 nodes and 439121 tetrahedral elements in
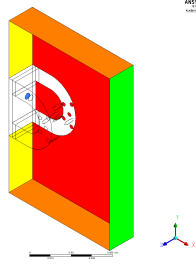the solid domain, 1475 nodes and 5791 tetrahedral elements in the glue domain and in the im-

Figure 3.12: Leading edge model and boundary conditions

Coolant Inlet	
Main Flow Outlet	
Main Flow Inlet	
Periodic	
Adiabatic Wall	

Table 3.4: Boundary Conditions

pingement plate domain 5969 nodes and 26047 tetrahedral elements. The interfaces fluid-solid, glue-impingement plane, periodic solid and glue-solid are setted as GGI, whilst the fluid periodic interface is set as 1:1. This set of interfaces are chosen in order to obtain an ideal infinite rows of holes.

Following the studies of Ravelli, particular attention was used regarding the speed and the direction of the coolant.

(a) *Overall Effectiveness M=1*   **(b)** *Overall Effectiveness M=2*
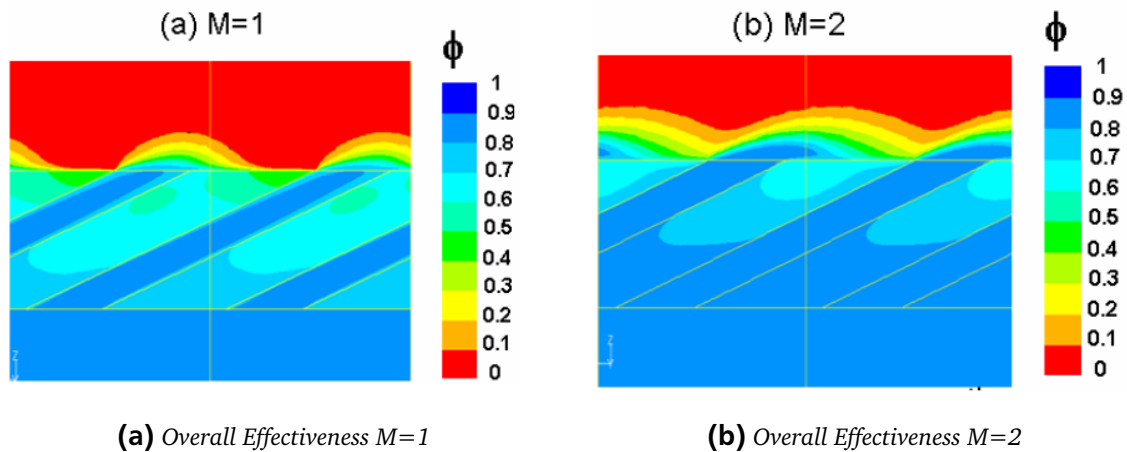
Figure 3.13: The influence of the blowing ratio on the overall effectiveness, [9]

According to the pictures 3.13a and 3.13b, by decreasing the blowing ratio the influenced zone of the coolant flow decreases, too, as a consequence of a decreased cooling mass flow. This happens because the higher the blowing ratio the higher is the inertia and the momentum of the coolant. As a result, in the cases with high blowing ratio, a detachment of the coolant flow could occur.

By increasing the inlet Mach number the blow-

Figure 3.14: LE fluid mesh, Hilgert

ing ratio decreases and this leads to an influence on the speed direction of the flow, as can be seen in Figures 3.15a and 3.15b on the next page. Regarding the sensitivity analysis, the most affected

zone will be in this area of the leading edge model and the physical reasons for the movement of the sensitivity zone are the influence of the velocity direction and the detachment of the coolant flow. Whilst, regarding the MT1 case the influence on the exit velocity direction of the coolant flow is negligible since the velocity of the main flow is parallel to the coolant exit flow.

(a) *Exit direction blowing ratio M= 3*   **(b)** *Exit direction blowing ratio M= 1*
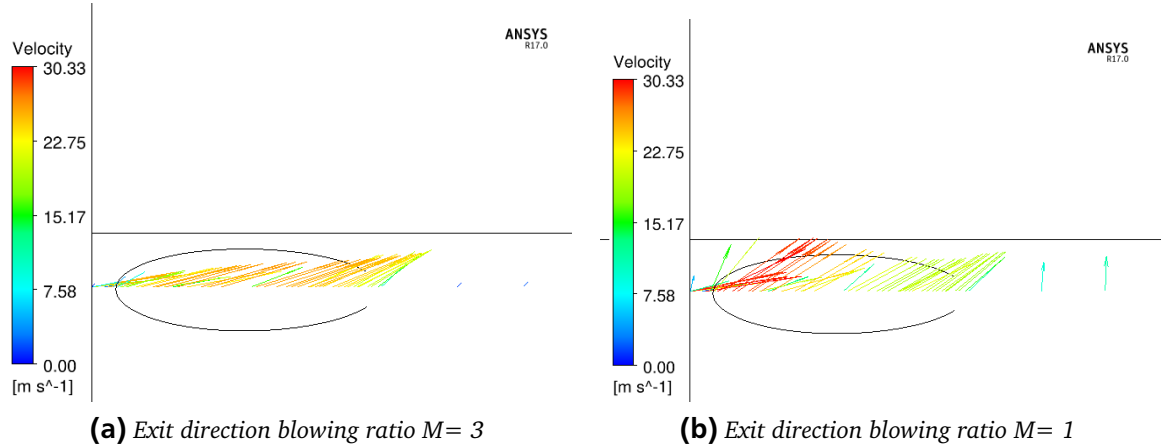
Figure 3.15: The influence of the blowing ratio on the coolant velocity direction

The Figure 3.15 shows the exit velocity direction of the off-stagnation holes for two different blowing ratios. By decreasing the blowing ratio, the inertia of the coolant is reduced with respect of the main flow. This leads to a different exit velocity and direction of the coolant.

3.3 MT1

Internal cooling and film cooling in the MT1 nozzle guide vane are both present. The aim of the thesis is to superimpose the results obtained by the low fidelity test cases on the MT1 case. The separation and re-attachment can be seen in this case, too, and the film cooling holes in the pressure side close to the leading edge can be compared with the leading edge test case.
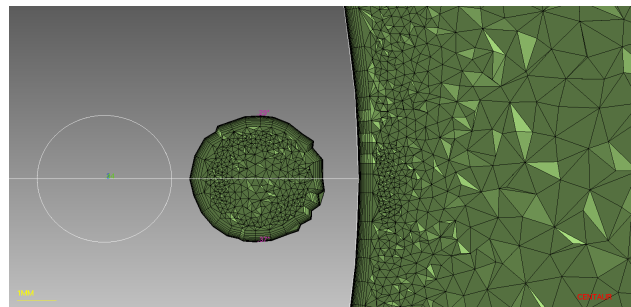

Figure 3.16: MT1 fluid mesh, Hilgert

The mesh files and the Pre file were created by Hilgert. Two different domains are defined, one for the solid and one for the fluid. Regarding the fluid domain, Figure 3.16, 7576013 nodes and 23145283 elements (12874217 tetrahedra , 61016 pyramids and 10210050 wedges) are created, 15 layers are used for the boundary layer. In the solid domain 408628 nodes and 2023817 tetrahedral elements are created. To couple the two domains a fluid-solid CHT interface is created. The CHT interface between solid and fluid is set as GGI, whilst the periodic interface is set 1:1.

The set of boundary condition are similar with respect to the Mark II case.

The results are compared with the findings of Chana et al. [7] and are shown in Figure 3.18. There is a good agreement with the experimental results. From 70% of the chord length the data

Figure 3.17: MT1 geometry and boundary conditions

Table 3.5: Boundary Conditions
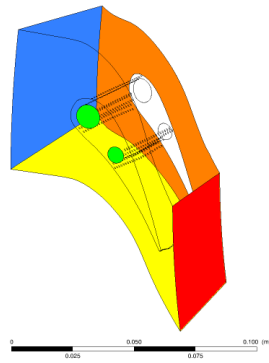
🟦	Main Flow Inlet
🟨	Periodic
🟩	Coolant Flow Inlet[a]
🟥	Main Flow Outlet
🟧	Adiabatic Wall

[a] The 2 Inlet had different values of BCs

separate with regard to the simulation results, this error can be related with the unsteady rotating potential field of the rotor[1].
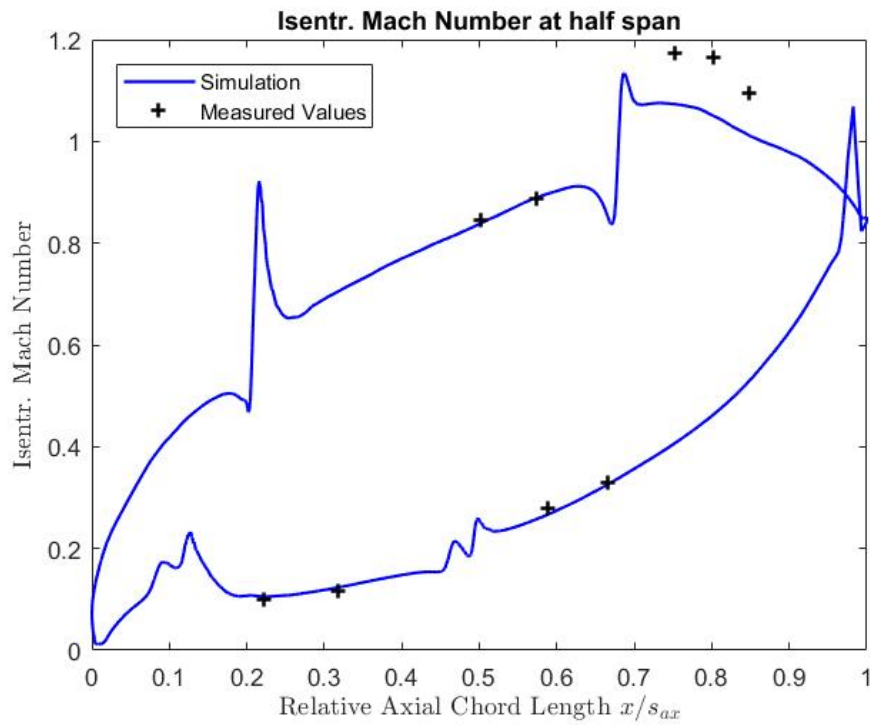
Figure 3.18: Isentropic Mach number distribution at half span

In order to compare the sensitivity obtained in the LE model, the same physical phenomena should be present also in this case, in particular the detachment, because the influence of the exit velocity direction can be neglected.

---

[1]   In that zone the Mach number decreases and this means a deceleration due to vane geometry.

(a) *Adiabatic effectiveness M = 0, 56*   **(b)** *Adiabatic effectiveness M = 0.22*
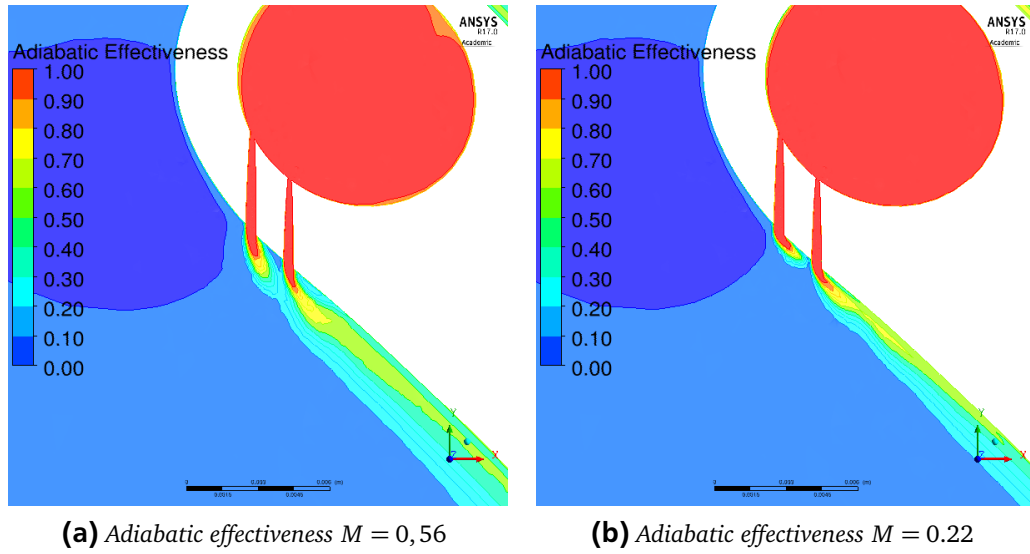
Figure 3.19: The effect of the blowing ratio on the adiabatic effectiveness

The plane in Picture 3.19 is a plane that cuts two lines of cooling holes in the pressure side. The adiabatic effectiveness behavior is the same shown in Figure 3.13. The highest inertia of the coolant flow in the case of high blowing ratio leads to the detachment of the flow. However, the separation of the flow does not occur when decreasing the blowing ratio.

The figure on the right side shows the separation of the flow, but in this case the phenomenon is not caused by the shock. As a matter of fact, the pressure ratio used in the MT1 simulation is such that the shock happens outside the nozzle. Hence, the factor that leads to separation is the geometry that creates adverse pressure gradients.

The pressure field used as outlet boundary condition is obtained averaging the pressure field from an unsteady solution, as shown in Figure 3.21 on the following page.
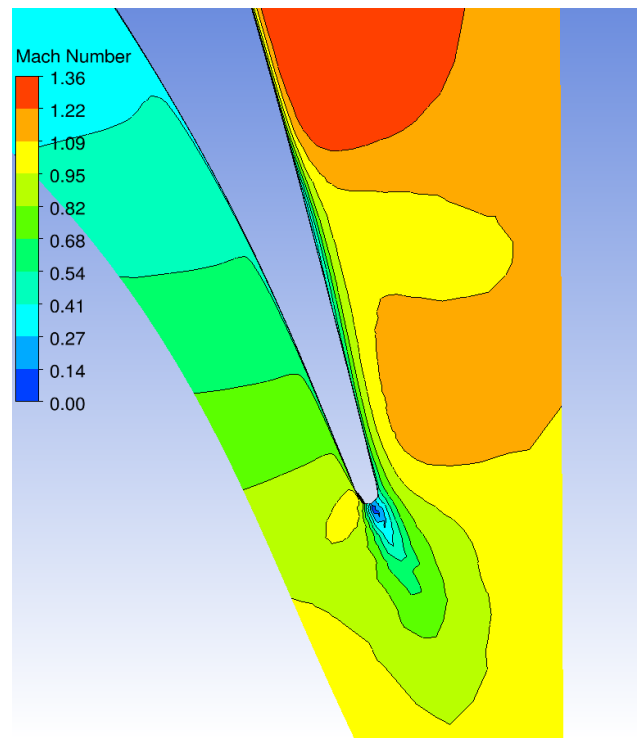
Figure 3.20: The separation in the MT1 vane
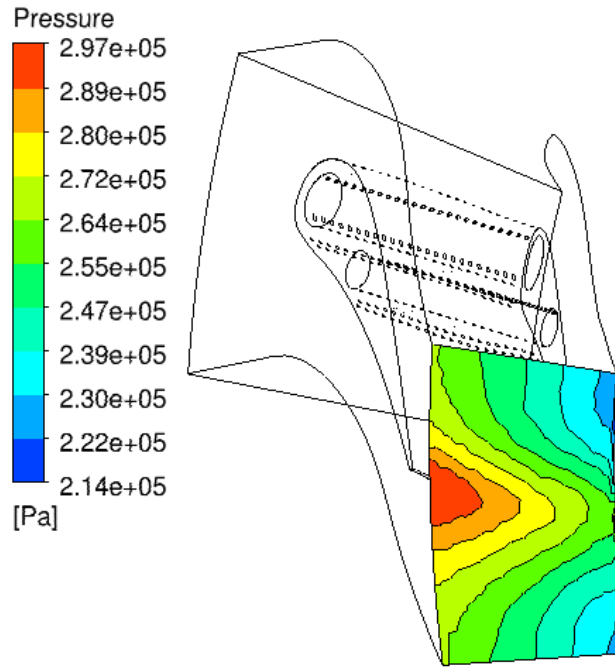
Figure 3.21: The outlet pressure distribution in the MT1 vane

3.4 Simulation Strategy

The main focus of this thesis is placed on the sensitivity of the physical quantities on the vane regarding the variation of the inlet parameters. The strategy is the same for all the cases: the inlet pressure, velocity [2] and turbulence intensity are changed in order to obtain the desired Reynolds or Mach number. In the Mark II case the inlet total pressure is in Table 3.6. In the LE model the temperature variation does not lead to a high change of Mach number, because of that only the table of the inlet velocity is shown 3.7b on the facing page. In the MT1 case the inlet conditions are shown in Table 3.7a.

The blowing ratio is used to compare the film cooling efficiency. Moreover, the Mach number and the Reynolds number are used to understand the influence of the separation.

Total Inlet Pressure [bar]	Inlet Re	Exit Ma
2,7	$9,35 \cdot 10^5$	0,91
3	$9,49 \cdot 10^5$	0,94
3,3	$1,05 \cdot 10^6$	1,02
3,5	$1,11 \cdot 10^6$	1,07
4	$1,27 \cdot 10^6$	1,18
4,3	$1,37 \cdot 10^6$	1,23
4,7	$1,50 \cdot 10^6$	1,30
5	$1,59 \cdot 10^6$	1,34
6	$1,91 \cdot 10^6$	1,47
9	$2,87 \cdot 10^6$	1,75
10	$3,18 \cdot 10^6$	1,82

Table 3.6: The Reynolds number and the Mach number for each inlet total pressure, Mark II

---

[2]   In the LE model.

Pressure [bar]	Exit Ma	Blowing Ratio
4,6	0,94	0,61
5,1	1,03	0,56
5,6	1,10	0,5
6,1	1,17	0,45
6,6	1,23	0,40
8	1,38	0,32
9	1,46	0,26
10	1,53	0,22
12	1,65	0,15

(a) The Reynolds number, the Mach number and blowing ratio for each inlet total pressure, MT1

Inlet Velocity [bar]	Inlet Ma	Blowing Ratio
5	0.014	5,88
10	0.029	2,94
15	0.043	1,96
20	0.058	1,47
25	0.072	1,17
30	0.086	0,97
35	0.101	0,83
36	0.104	0,81
37	0.107	0,79
38	0.109	0,76
40	0.115	0,73

(b) The Mach number for each inlet Velocity, LE model

Table 3.7: The Reynolds number, the Mach number and blowing ratio for each inlet total pressure

The inlet turbulence intensity influence is also analysed and the inlet conditions are summarized as follows

Inlet Turbulence Intensity Mark II	Inlet Turbulence Intensity MT1	Inlet Turbulence Intensity LE
5	5	5
10	10	10
15	15	15
20	20	20
25	25	25

Table 3.8: The inlet turbulent intensity

4 Results

4.1 Mark II Results

The sensitivity's cause of the Mark II vane is imputable to the separation of the flow due to the shock in the suction side of the vane. As evidenced by Hylton [11], the variation of the Reynolds number does not influence the distribution of the physical quantities on the wall. The parameter responsible of the location and magnitude of the high sensitivity zones is the Mach number.

By increasing the exit Mach number the shock position moves towards the trailing edge. Since

(a) *Heat flux sensitivity* $Ma = 0.94 \div 0.90$ **(b)** *Heat flux sensitivity* $Ma = 1.02 \div 0.94$

(c) *Heat flux sensitivity* $Ma = 1.07 \div 1.02$ **(d)** *Heat flux sensitivity* $Ma = 1.18 \div 1.07$
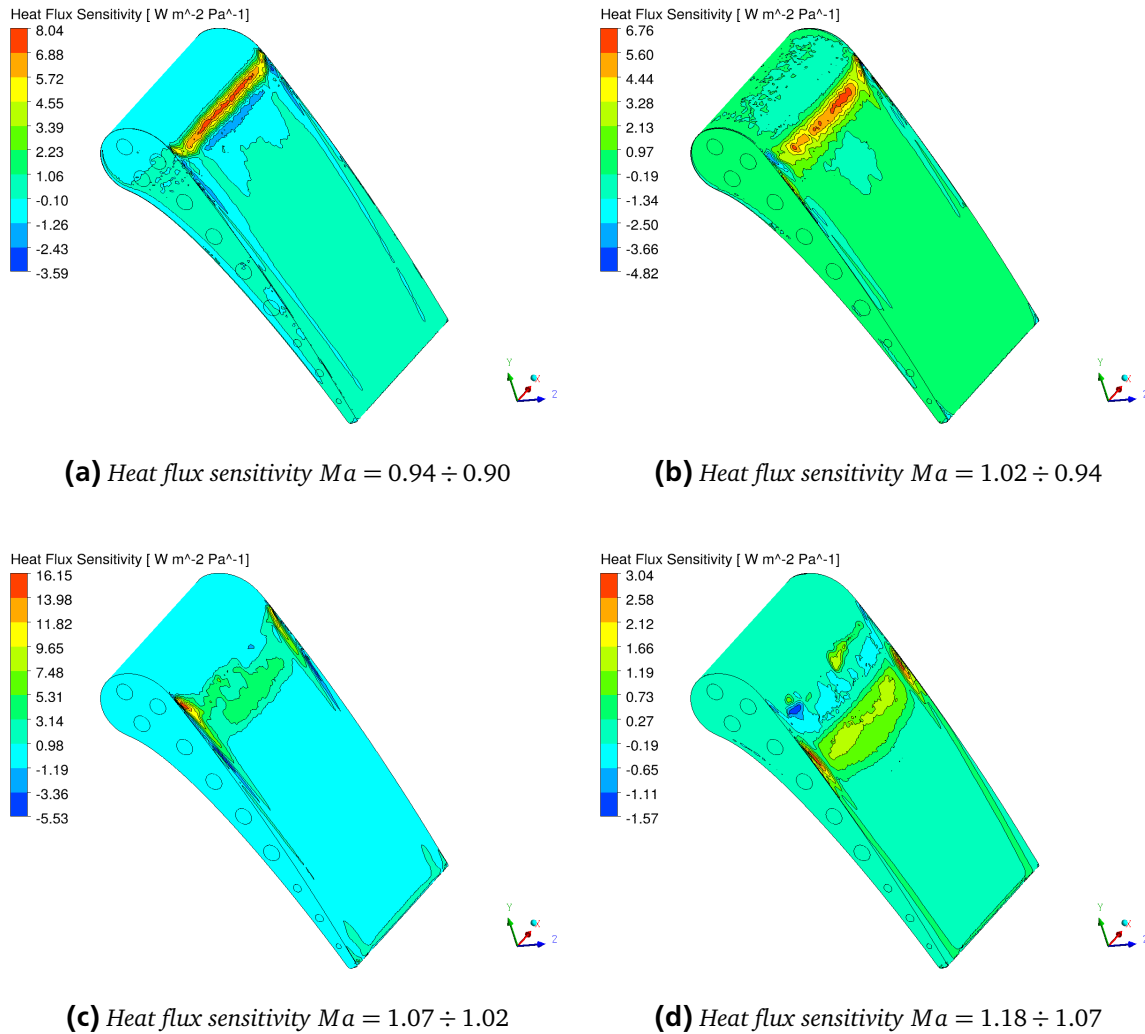
Figure 4.1: The movement of the sensitivity in the heat flux case, Mark II

the shock and the separation of the flow are linked phenomena, due to the deceleration imposed

by the shock, the most affected areas will form because of the shock movement.

It can be seen in the picture 4.1 that the most affected zone moves towards the leading edge.

The magnitude of the sensitivity decreases by increasing the exit Mach number. In the picture, the maximum value of the contour has a random behavior, but in some cases the secondary flow vortex influence is higher than the separation influence (for example the figure 4.1 c).

The high sensitivity zones of the temperature increase their magnitude. However, the sensitivity

(a) *Temperature sensitivity $Ma = 0.94 \div 0.90$*

(b) *Temperature sensitivity $Ma = 1.02 \div 0.94$*

(c) *Temperature sensitivity $Ma = 1.07 \div 1.02$*

(d) *Temperature sensitivity $Ma = 1.18 \div 1.07$*
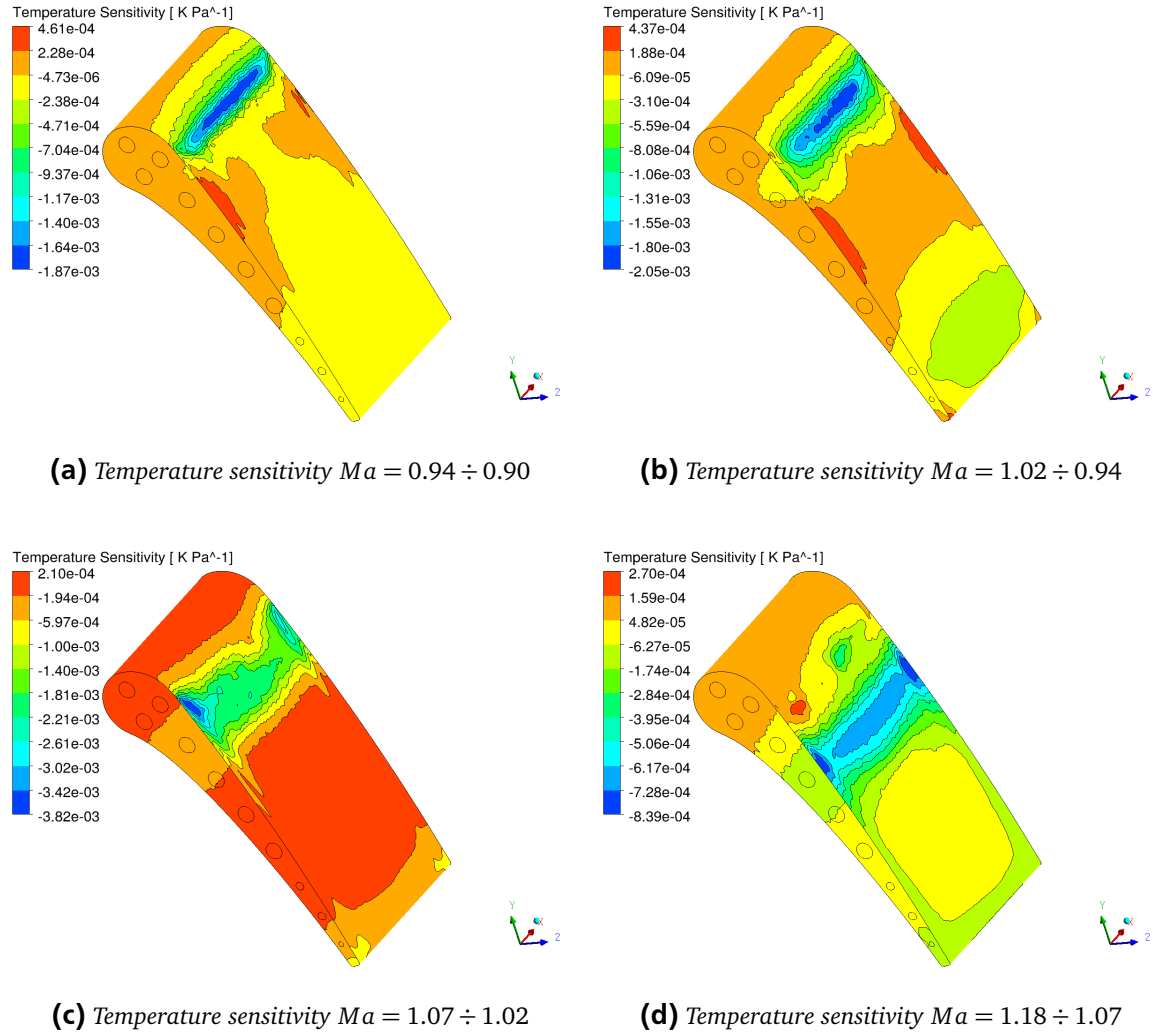
Figure 4.2: The movement of the sensitivity in the temperature case, Mark II

absolute value is negative, this means that the separation leads to a reduction of the temperature on the wall and, as a consequence, the heat flux increases in magnitude. The next pictures show the movement of the sensitivity at half span. Also in these figures can be seen the movement of the high sensitivity zone due to the shock movement.
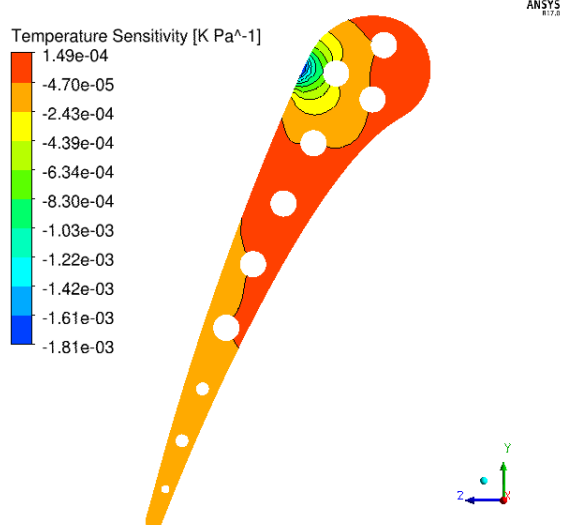
(a) *Temperature sensitivity $Ma = 0.94 \div 0.90$*
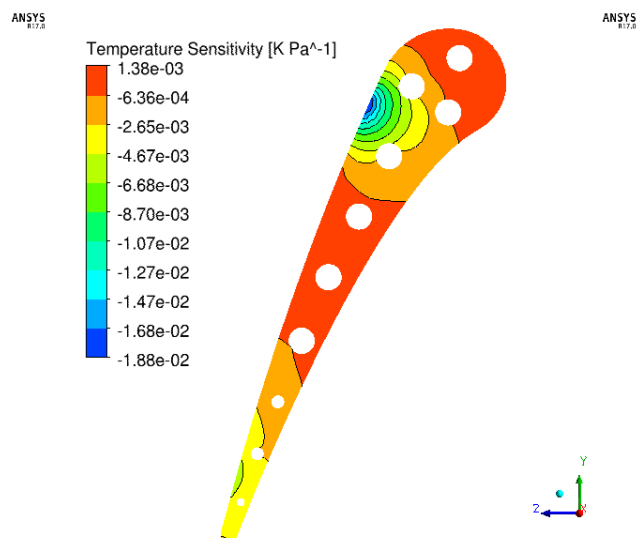
(b) *Temperature sensitivity $Ma = 1.02 \div 0.94$*
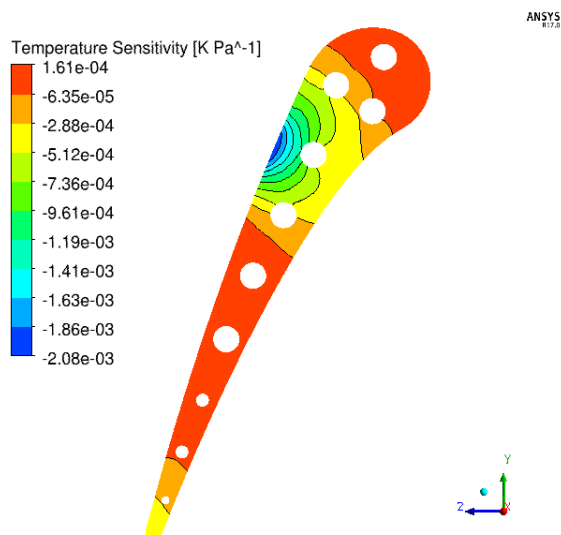
(c) *Temperature sensitivity $Ma = 1.07 \div 1.02$*
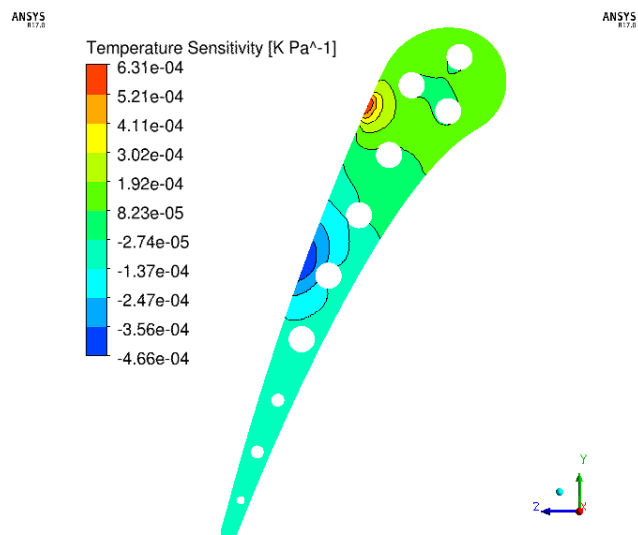
(d) *Temperature sensitivity $Ma = 1.18 \div 1.07$*

Figure 4.3: The movement of the sensitivity in the temperature case, Mark II midspan

The last inlet parameter to be analysed is the inlet turbulence intensity. The value of the turbulence intensity characterises the amount of fluctuation of the inlet flow. The Figures 4.4 show the sensitivity of the heat flux.

(a) *Inlet turbulent intensity $I = 10\% \div 5\%$*

(b) *Inlet turbulent intensity $I = 15\% \div 10\%$*

(c) *Inlet turbulent intensity $I = 20\% \div 15\%$*

(d) *Inlet turbulent intensity $I = 25\% \div 20\%$*
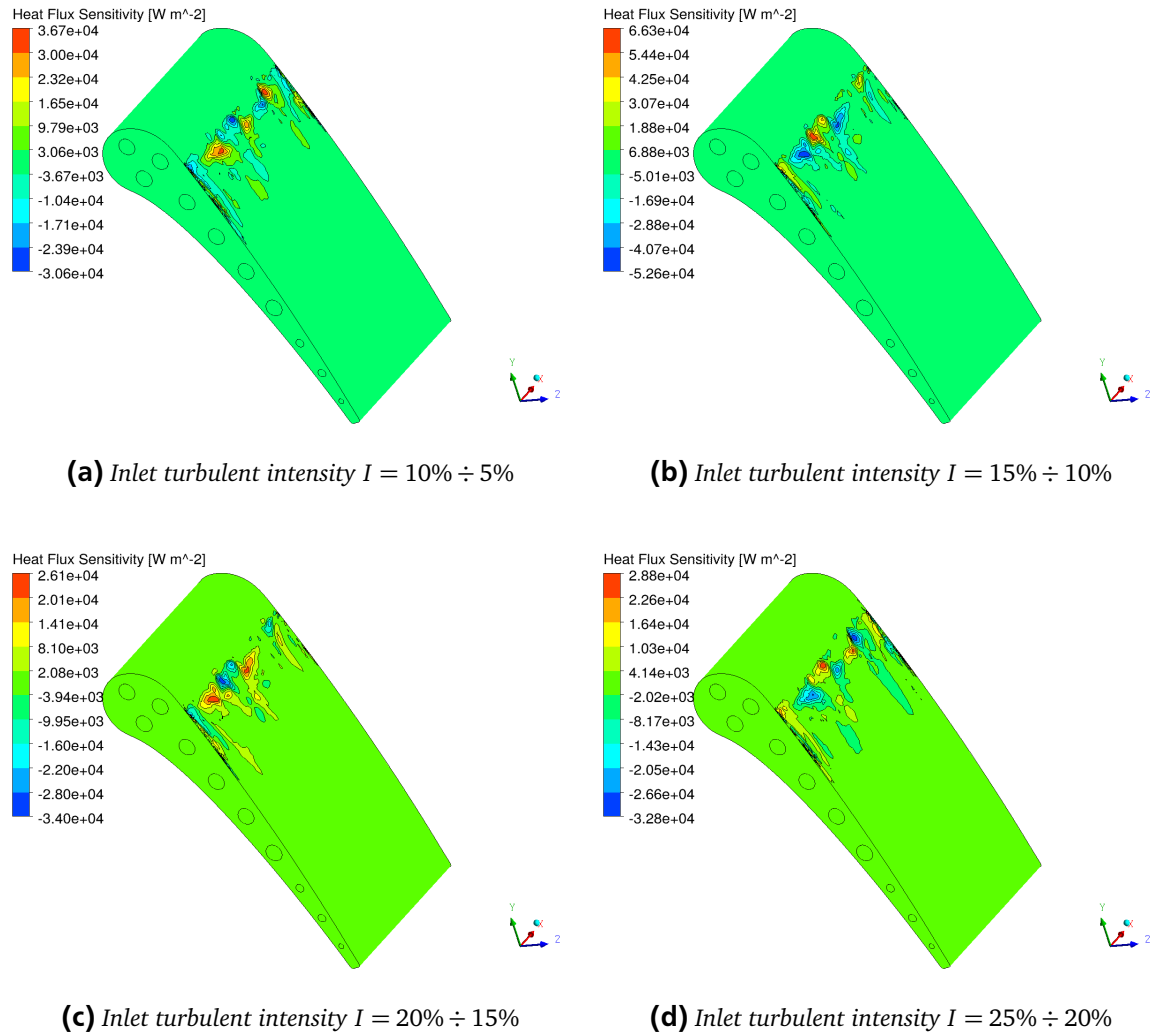
Figure 4.4: Heat flux sensitivity in the turbulence case

As can be seen, the position of the most affected zones seems fixed for all the cases. The turbulent intensity influences the transition of the flow, because the higher the intensity the higher is the tendency to change the flow regime.

It is also important to notice that the turbulent intensity does not influence the position of the shock and separation. As a consequence, the sensitivity looks fixed and the position of the most affected zones are randomly positioned at the suction side.

The creation of these sensitivity zones in the transition area are caused by the instability of the flow. However, an exact and precise analysis of the phenomenon can not be done, because, as explained in the section 2.5, the formation of the turbulence spots occurs at random time and position.

In the appendix more pictures for each case with different Mach number steps are attached.

4.1.1 Temperature Distribution on Mark II Mid Span

In this section the influence of the inlet temperature is investigated. A series of simulations are performed changing only the inlet temperature.

The temperature's values have been summarized in the table 4.1:

Plotting the midspan temperature distribution it seems clear that there is a correlation between

Simulated Inlet Temperature [K]						
773	778	783	778	793	798	803

Table 4.1: Hot Gas Inlet Temperature

the wall temperature and the inlet temperature, figure 4.5.
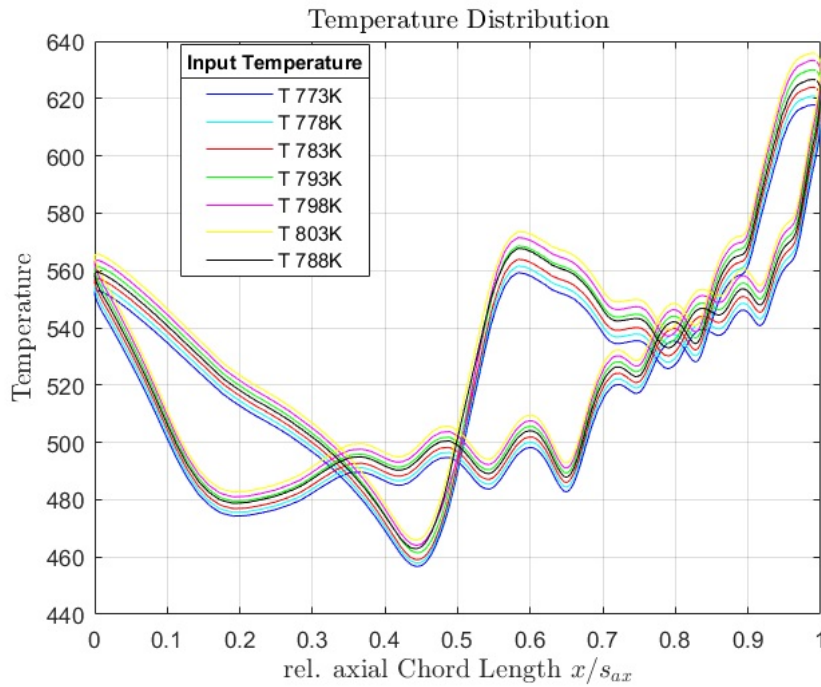
Figure 4.5: Temperature distribution on the Mark II midspan for different Inlet Temperatures

The picture evidences that the lines are shifted. Thus, the aim is to calculate a linear relation between the temperature of the validated test case and the temperature of each node on the vane wall for the other inlet temperature cases.

$$Factor = \frac{T_i - Tref,i}{Tref,i} \qquad (4.1)$$

The equation 4.1 is implemented in *Matlab* and several temperature distributions are obtained by multiplying the values of the validated test case by the calculated factor. The next step to take is to

compare the CHT temperature distribution and the temperature distribution obtained in *Matlab*. Figure 4.6 shows the results: The first picture compares the CHT temperature distribution with the
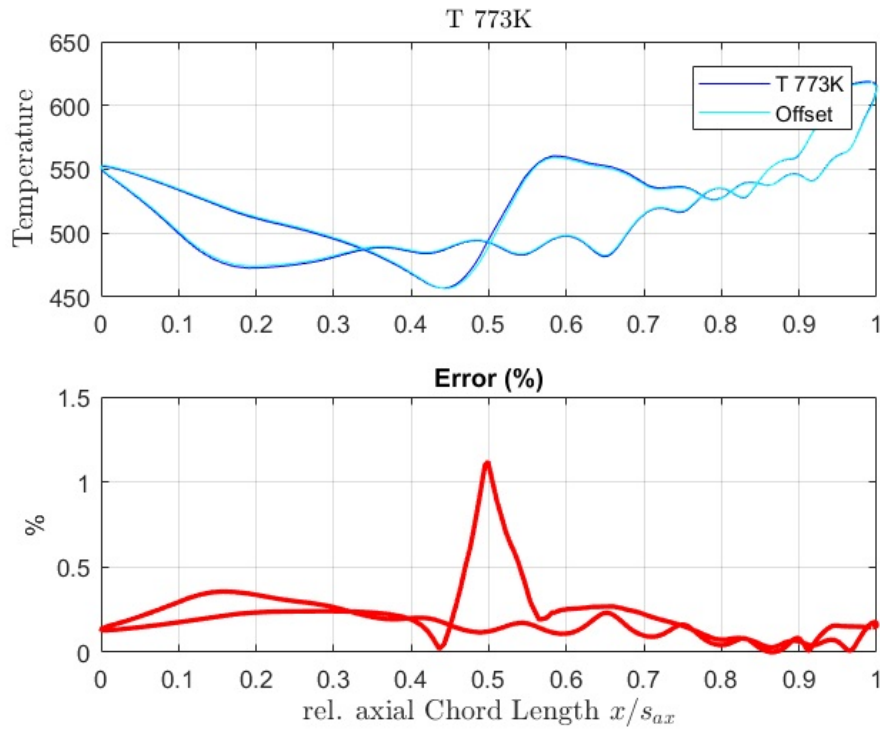
Figure 4.6: CFD calculated temperature vs *Matlab* calculated temperature distributions and the relative error, $T_{in} = 773K$

derived temperature distribution, whilst the second evidences the error with respect to the coupled simulation.
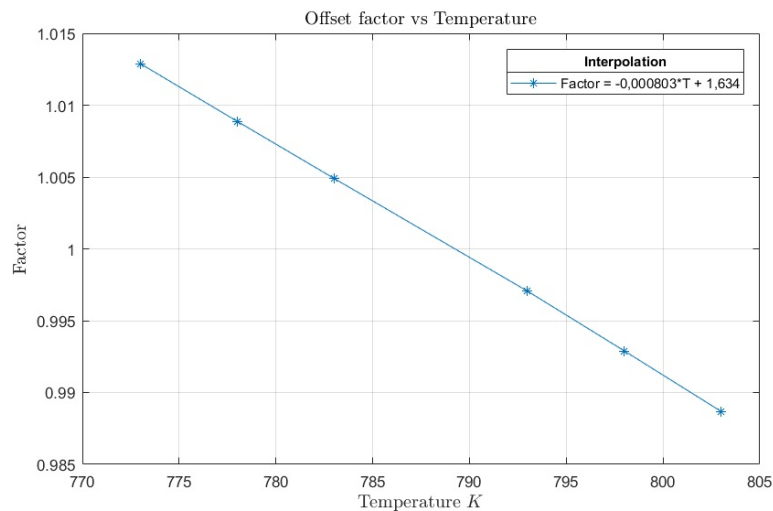
Figure 4.7: Offset Factor vs Wall temperature of the validated test case

The relative error is very small towards the leading edge and trailing edge for the pressure and suction side, while it has the maximum in the separation/re-attachment zone of the suction side.

This trend was expected, as explained in the section 3.1 and in particular in Figure 3.9 in which the experimental results seem to be grouped only in the separation/re-attachment area. The same results are obtained for the other inlet temperatures, see the section A on page 73. Considering the error acceptable, the offset factor is represented in the figure 4.7.

4.2 Heat Transfer Coefficient Calculation on the MarkII Vane

The assumption that the heat transfer phenomenon is just regulated by the aerodynamics of the vane, implies that the heat transfer coefficient is not a be function of the vane wall temperature. However, in a particular condition this assumption loss a little bit of its power. Regarding the Mark II vane, the Nusselt number distribution can be seen in the picture 4.8. The Figure shows different Nusselt number distributions for different temperature ratios. It is shown that on the pressure side and on the suction side before the laminar to turbulent transition, the values of the Nusselt number coincide. But, after the shock zone, the lines seem to be shifted. In this part of the Nu-distribution, the temperature wall dependence becomes important. This topic was also discussed by Maffulli [12] who found a clear dependence in his paper. The simple geometry of the vane
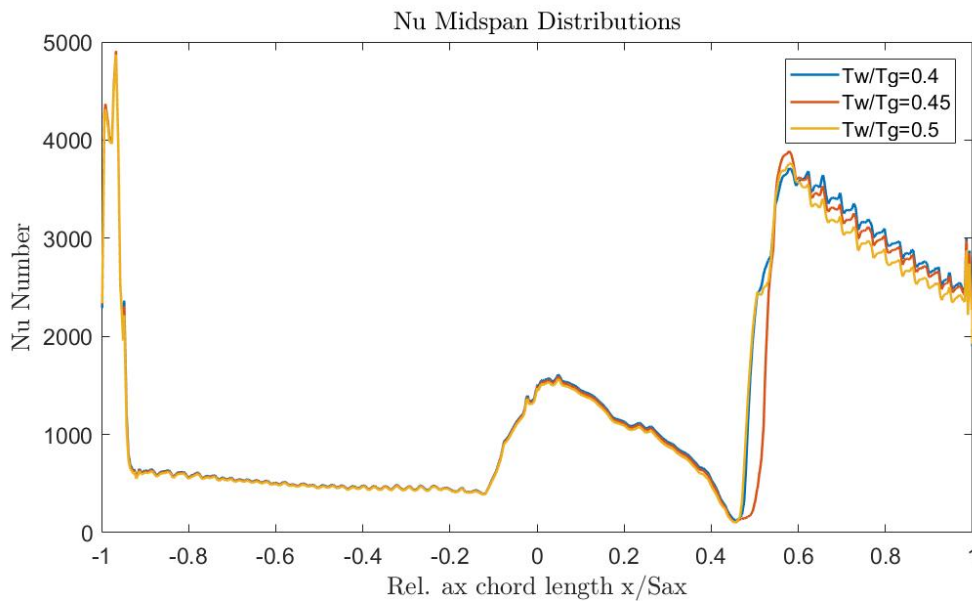
Figure 4.8: Nusselt number trend vs relative chord length

makes the classic method very robust.

Figure 4.9 shows the comparison between the heat flux calculated with the 2 point method and the heat flux obtained by another uncoupled simulation using a different temperature ratio (other pictures are available in the appendix). The error is very high in the separation zone. Regarding the classic method, it seems that the hypothesis of the constancy of the htc is not accurate. In fact the error in the picture 4.9 is high. Moreover, the error increases in magnitude in the separation zone, this could be attributed to the fact that the classic method is not efficient to describe the heat flux in the separation case.

The picture 4.10 shows the comparison between the heat flux calculated using the Maffulli method and the heat flux obtained by an uncoupled simulation. The error seems to be very low, except in

the separation zone. However, the Maffulli method works very well in a very large temperature range, but also in this case it seems to be not accurate to simulate the separation phenomenon.
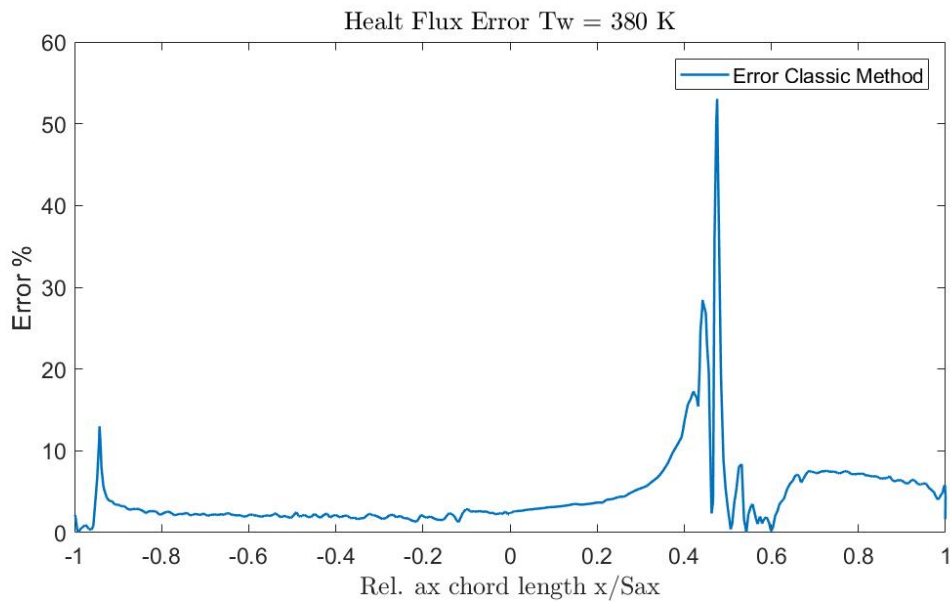
Figure 4.9: The error on the heat flux using the classic method

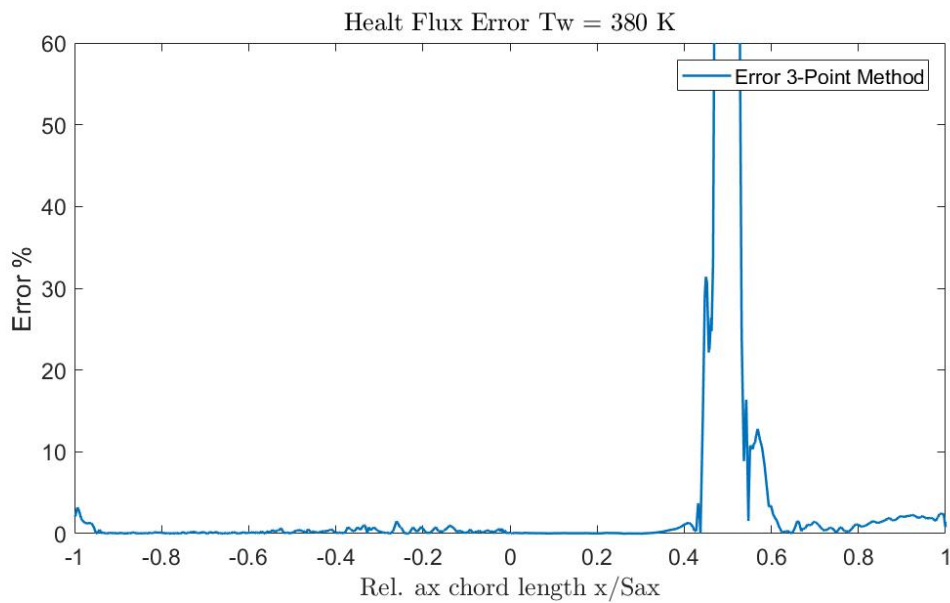**Figure 4.10:** The error on the heat flux using the Maffulli method

To conclude, the Maffulli method very precise compared to the classic one, but it overestimates the heat flux in the separation zone. Furthermore, the Maffulli method works in a large range of temperatures, whilst the htc calculated using the classic method seems to be valid in a limited range of temperatures.

In order to verify the efficiency of the classic method, the results of a simulation with only the solid domain are evaluated. The htc distribution calculated in the previous section is used as boundary condition for the external wall of the vane and for the internal cooling ducts. Moreover, a reference temperature is required to close the problem. Hence, the adiabatic wall temperature is chosen. In order to compare the findings with a coupled simulation, the adiabatic wall temperature used is obtained by running a simulation with the same boundary conditions as the coupled simulation, without the solid domain and using the adiabatic condition at the wall. Thus the adiabatic simulation is run with only the fluid domain.

Concerning the simulation setting, only the solid domain is used. The adiabatic wall condition is set for the vane hub and shroud. The htc distribution and the adiabatic wall temperature distribution are used for the external and internal walls. The mesh of the solid is the same as described in the section 3.1.

The adiabatic temperature calculated using the setting described previously is the link between the coupled and the uncoupled simulations. This means, since the htc is not influenced by the wall temperature, that the coupling is created using the adiabatic wall temperature calculated in order to set the same boundary condition as the CHT simulation case.

The first impression suggest that in the coupled simulation, in the picture 4.11a, it is possible to

(a) *Heat flux calculated using the coupled simulation* **(b)** *Heat flux calculated using the uncoupled simulation*
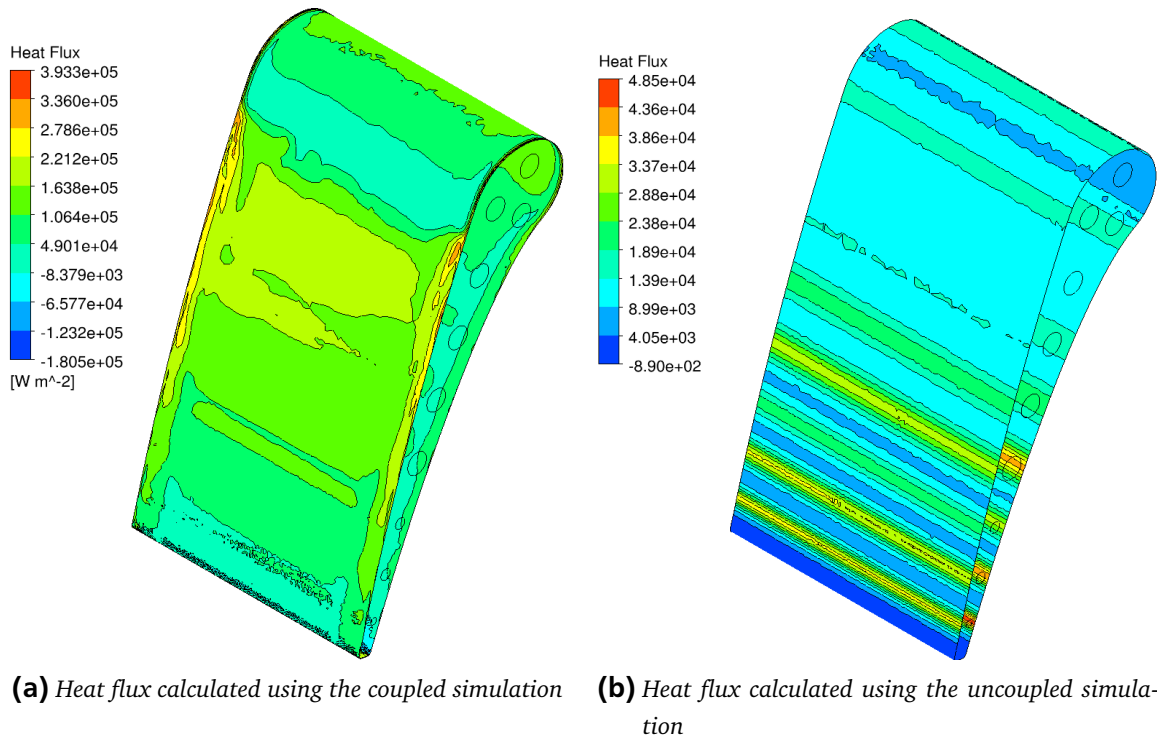
Figure 4.11: Heat flux simulation between the coupled and uncoupled simulation

notice the effects of the vane aerodynamic for example, in the shock zone. Whilst, in the uncoupled it is not possible; the influence of the cooling ducts is more pronounced in the uncoupled, this not

happens in the coupled. Another important consideration is, in the uncoupled simulation, the value of the heat flux seems to be constant in the radial direction, see Figure 4.11. Another detail
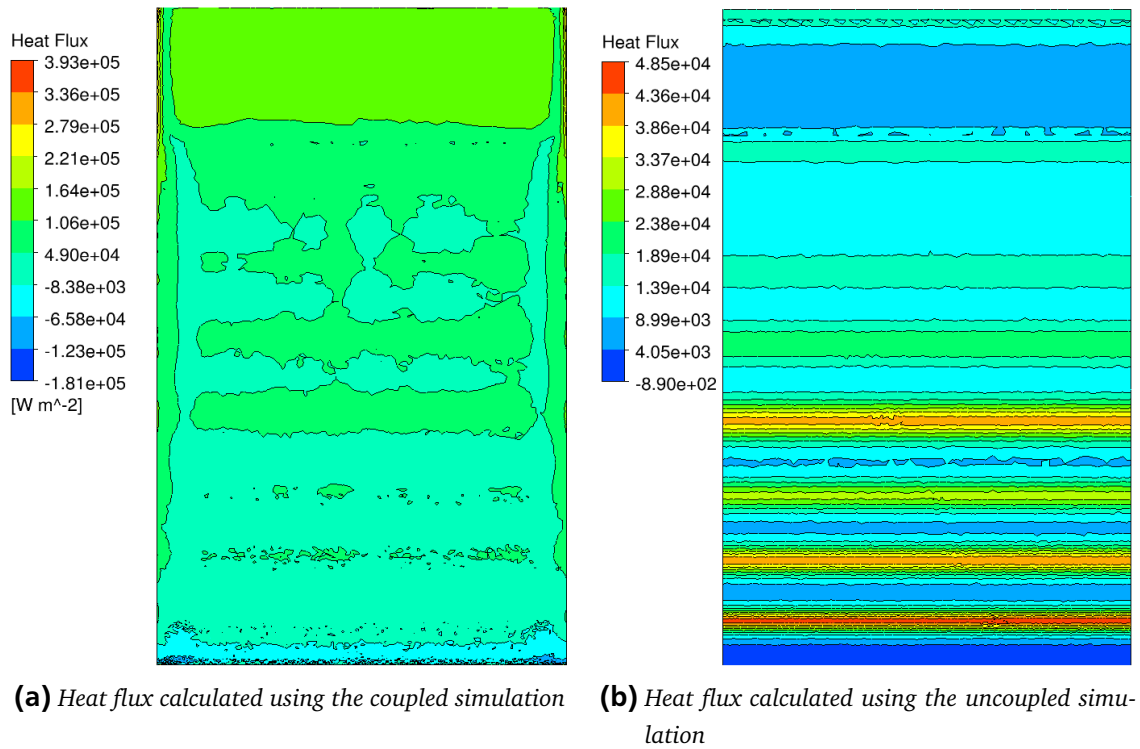

(a) *Heat flux calculated using the coupled simulation*   **(b)** *Heat flux calculated using the uncoupled simulation*

Figure 4.12: The heat flux in the pressure side for the coupled and uncoupled simulation

that can be appreciated in Figure 4.12 is the different heat flux values in the stagnation zone. An additional difference between the cases is the secondary flow induced heat flux which is not present in the uncoupled simulation.

Regarding the temperature contours, the same trend can be found. The influence of the cooling ducts is overestimated and also in the stagnation and shock zone the temperature values are very different.

The figures of this chapter show the difference between the CHT simulations and the classic simulations. The difference is very high and the CHT simulation is much more precise with respect to the classic simulations. However, the results obtained with the classic simulation should be iterated by using the heat flux, for example, to calculate a new htc distribution and then run a new simulation till the convergence is reached.
Usually the iteration of the results takes time and, because of that, the vane designers use the first result that they get. On the other hand, the CHT simulation gives much more precise information on the vane heat exchange. The influence of the stagnation or the shock, in this case, is taken into account.

At the end of the day, the coupled simulations are computationally power demanding, but the obtained results simulate in a better way the aerothermal behavior of the vane. The influence of
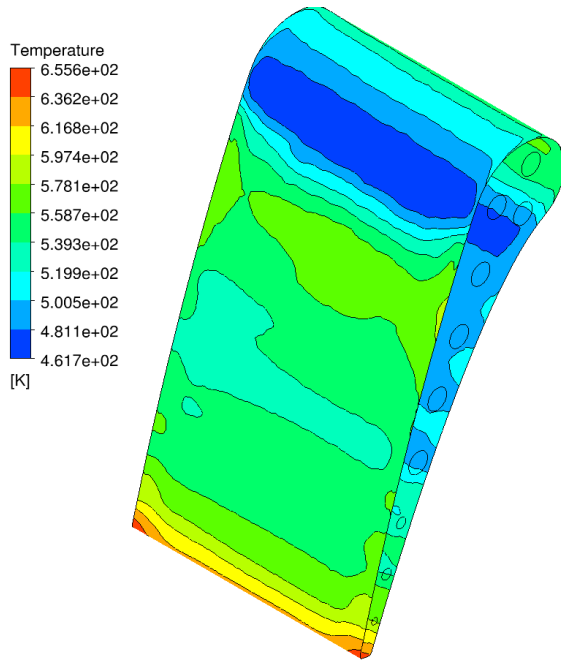
(a) *Temperature distribution calculated using the coupled simulation*
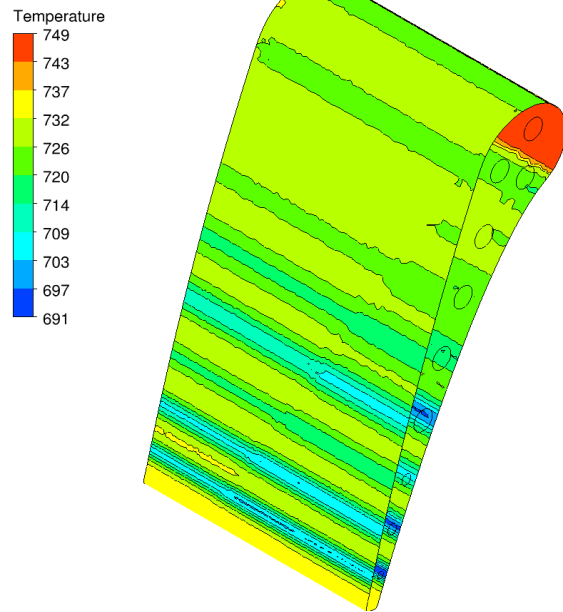
(b) *Temperature distribution calculated using the uncoupled simulation*

the aerodynamic phenomena can not be simulated using the classic method. However, the classic method requires an iteration process to get better results, but this requires time and at this point the desirability of the CHT simulations grow.
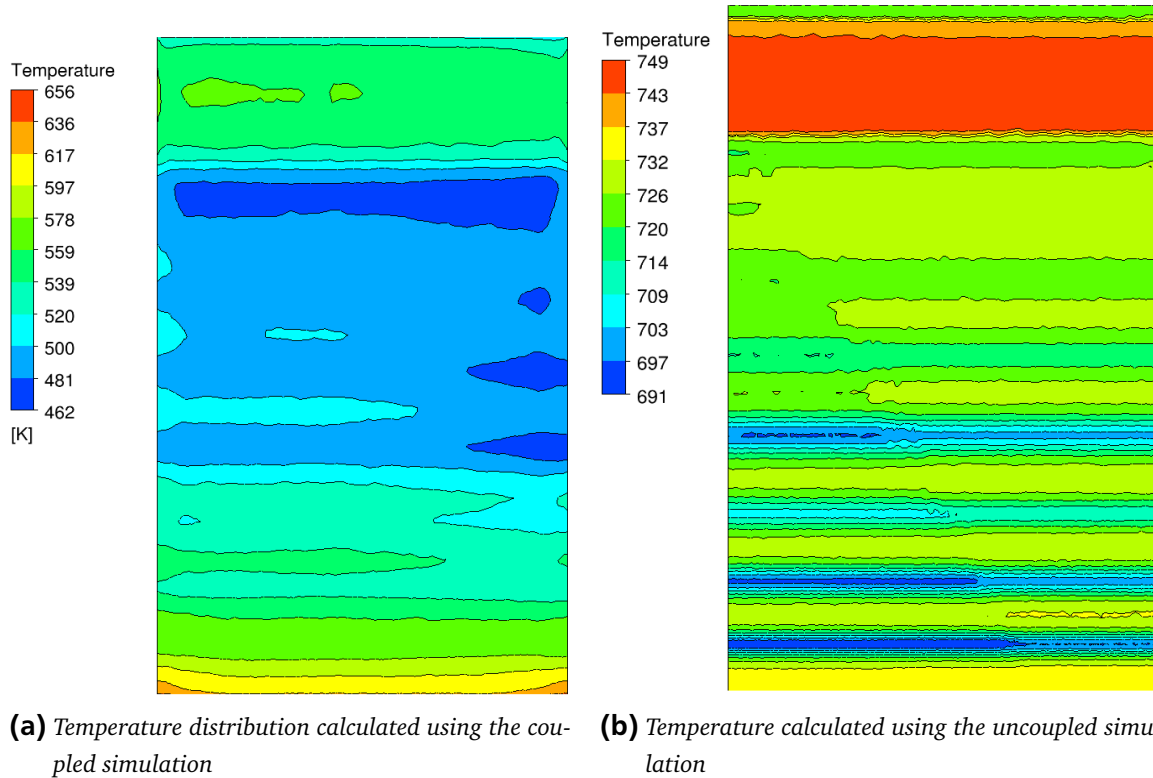
(a) *Temperature distribution calculated using the coupled simulation*

(b) *Temperature calculated using the uncoupled simulation*

Figure 4.13: The temperature distribution in the pressure side for the coupled and uncoupled simulation

4.3 Summary

The Mark II vane is a simple geometry vane, using ten internal ducts. The vane is cooled by fresh air. On the suction side a transition from laminar to turbulent flow happens, but the main factor that influences the sensitivity analysis is the separation of the fluid. The flow, due to the shock, detaches from the wall causing the variation of the physical quantities. Moreover, the separation zone position is strongly influenced by the exit Mach number, because, according to the isentropic nozzle theory, the situation corresponds to a different pressure ratio across the vane. Consequently, by increasing the exit Mach number the position of the separation moves downstream. Furthermore, the heat flux values on the vane surface decrease by decreasing the exit Mach number, whist the temperature values tend to increase.

The shock leads to an increase of the pressure, temperature and density due to the transformation of the total pressure into heat. Taking into account the Figure 4.1, it is possible to notice that the highest sensitivity values of the heat flux are in the separation zones. The extension and the position of the high sensitivity zone depends on the exit Mach number level. When the Mach number is high the sensitivity magnitude decreases, this means that the effect of the separation tends to attenuate. The values of the sensitivity in the rest of the vane are very low.

On the other hand, a positive heat flux sensitivity corresponds to negative sensitivity values of the temperature in Figure 4.2, whilst in the other regions of the vane the temperature sensitivity is

positive. The movement of the sensitivity can be seen in Figures 4.3 in which the temperature gradients are shown. The movement of the shock and, thus of the separation zone, leads to a decrement of the temperature in a particular node in the separation zone.

Regarding the inlet turbulence intensity, the position of the separation zone is not influenced. On the contrary, the transition from laminar to turbulent flow is affected by the turbulence intensity. Consequently, the position of the highest sensitivity values is fixed, but there is a randomly disposition of higher values due to the casual transition nature. However, the magnitude of the heat flux sensitivity, Figure 4.4, is significantly lower than the sensitivity values obtained changing the Mach number. This means that the influence of the transition is negligible compared with the influence of the separation.

Concerning the htc calculation, the pictures show that the result obtained with the CHT simulation are very precise and that it is difficult to find the aerodynamic coupling in the classic method. In order to get much better results using the classic method, iterations are required.

4.4 Leading Edge Model Results

In the section 3.2, the physical reason of the expected high sensitivity zones are described: the detachment and the influence on the direction of the coolant exit velocity.

As expected, the pictures 4.14 show the influence of the blowing ratio on the exit velocity direc-
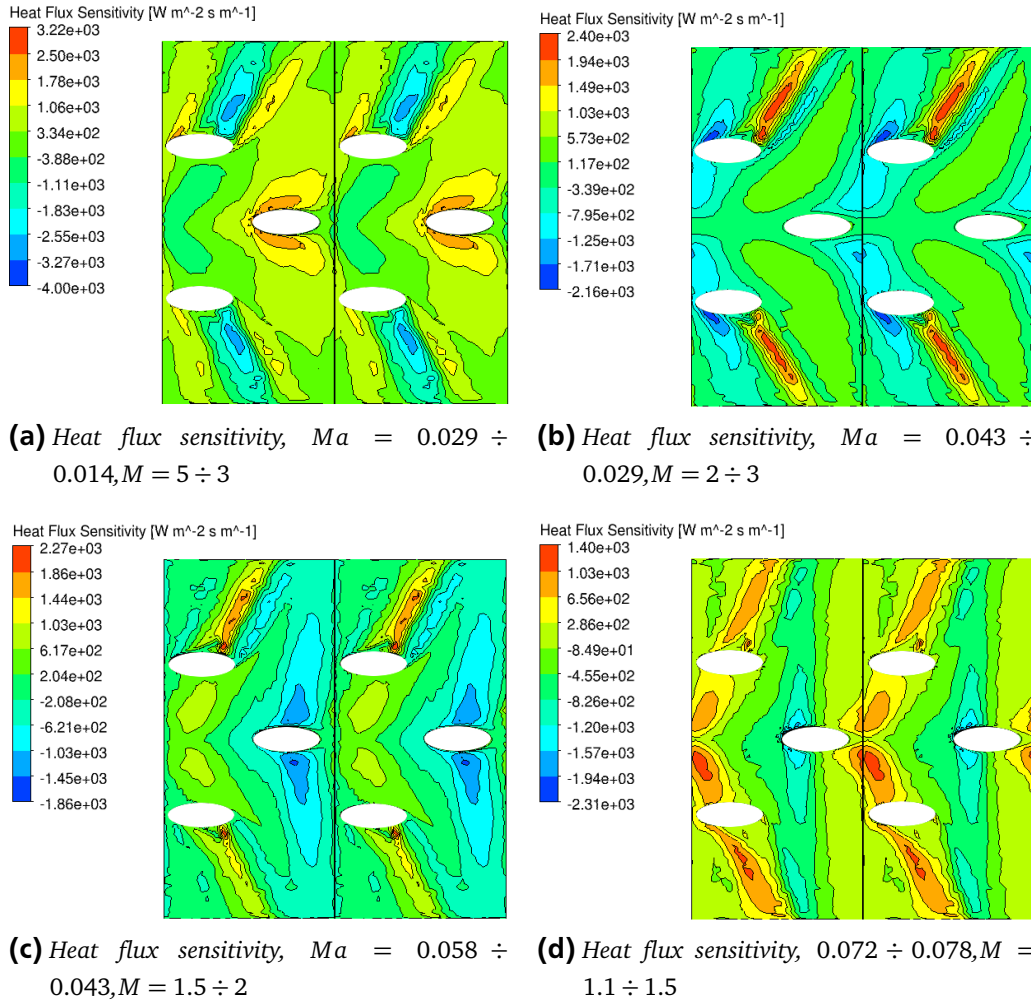

(a) *Heat flux sensitivity, $Ma = 0.029 \div 0.014, M = 5 \div 3$*

(b) *Heat flux sensitivity, $Ma = 0.043 \div 0.029, M = 2 \div 3$*

(c) *Heat flux sensitivity, $Ma = 0.058 \div 0.043, M = 1.5 \div 2$*

(d) *Heat flux sensitivity, $0.072 \div 0.078, M = 1.1 \div 1.5$*

Figure 4.14: The movement of the sensitivity in the heat flux case, LE

tion, and also the influence on the detachment. In the figures caption is indicated the inlet Mach number steps, but the two values are correlated.

By decreasing the blowing ratio, since the high inertia of the main flow, the velocity direction of the fresh flow tends to be parallel to the main flow velocity direction. Furthermore, when the blowing ratio is particularly low the separation of the flow does not occur. So that the influence on the region close to the holes is caused by a different cooling mass flow.

In Figure 4.15 are represented two cases with a low blowing ratio, the result is that the influence on the detachment can be considered neglectable, the high sensitivity zones are due to secondary flows.
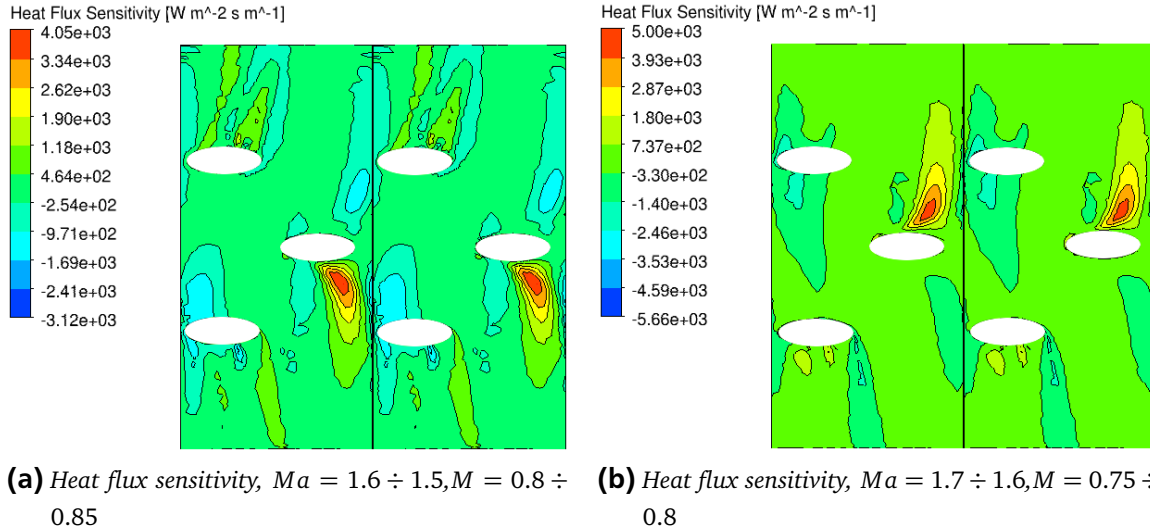
(a) *Heat flux sensitivity, $Ma = 1.6 \div 1.5, M = 0.8 \div 0.85$*

(b) *Heat flux sensitivity, $Ma = 1.7 \div 1.6, M = 0.75 \div 0.8$*

Figure 4.15: Heat Flux sensitivity in the heat flux case, LE

Figure 4.16 shows the sensitivity calculated for the temperature on the vane. As it happens in the Mark II case, a positive heat flux sensitivity corresponds to a negative temperature sensitivity and vice versa. The movement of the sensitivity is clear here, too. For low blowing ratios the influence of the exit direction can be neglected. The inlet turbulence intensity is now investigated. In this case, the exit direction of the coolant is fixed in direction. The sensitivity for low inlet turbulent intensity is lower than the other case. Whilst by increasing the turbulence intensity the sensitivity increase in magnitude in the vane. Since the flow with high turbulent intensity tends to be much more susceptible to the variation in the flow regime, the secondary flows are influenced. About the rest of the vane, the sensitivity values tend to zero.

In the Appendix other figures are available.

4.5 Heat Transfer Coefficient on the Leading Edge Model

Unlike the Mark II vane and the MT1 vane, for the leading edge model another strategy of htc calculation is used. The htc is calculated using two isothermal wall simulations. This means that in a possible uncoupled simulation, the reference temperature is the one calculated using two isothermal simulations. This process is much precise. By dealing with complex geometry such as in the cases of the MT1 and Mark II, no satisfactory results could be obtained. In order to obtain the htc three isothermal wall simulations are set: the temperatures of the wall are 235 K, 255 K and 275 K.

Figure 4.18 shows the htc distribution on the LE model calculated using different range of wall temperature.

The htc distribution in the figures seems to be fixed. Hence, there is not a relation between the wall temperature and the htc.
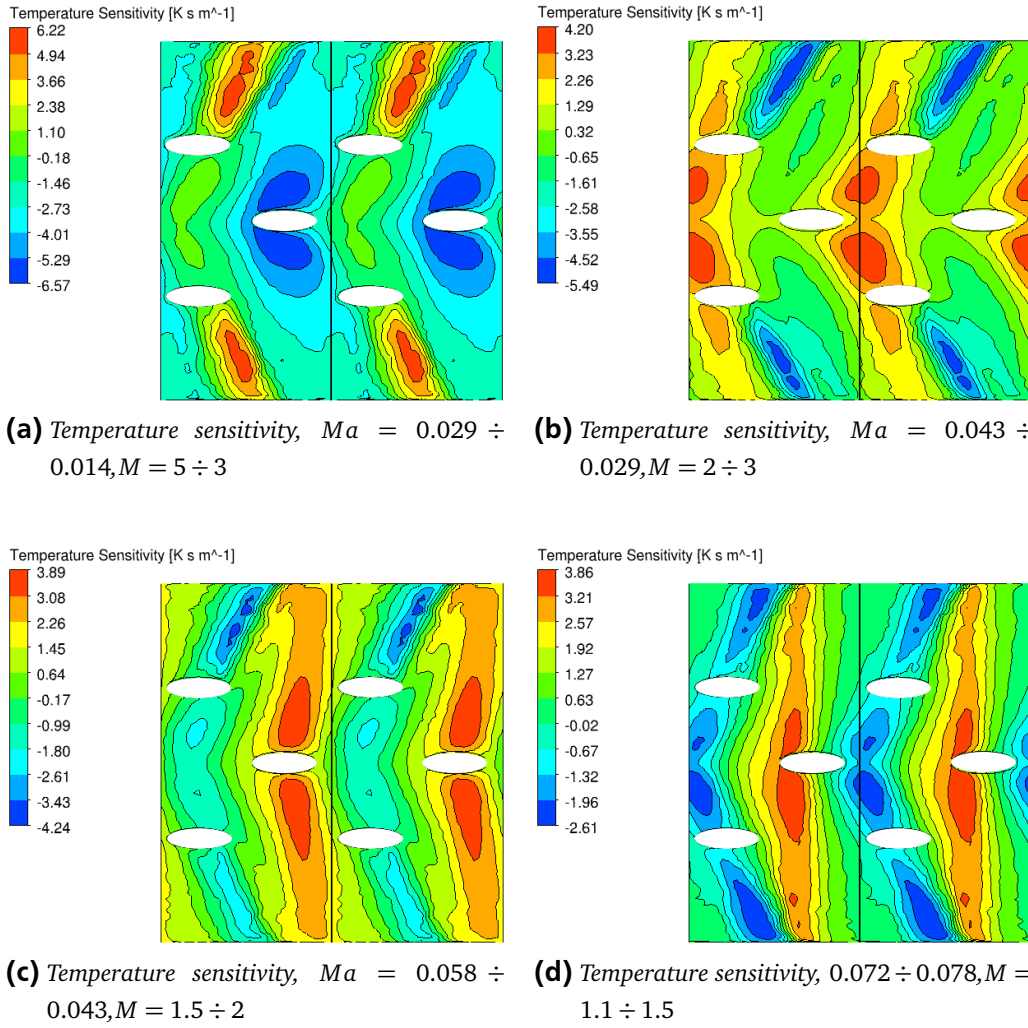
(a) *Temperature sensitivity, $Ma = 0.029 \div 0.014, M = 5 \div 3$*

(b) *Temperature sensitivity, $Ma = 0.043 \div 0.029, M = 2 \div 3$*

(c) *Temperature sensitivity, $Ma = 0.058 \div 0.043, M = 1.5 \div 2$*

(d) *Temperature sensitivity, $0.072 \div 0.078, M = 1.1 \div 1.5$*

Figure 4.16: The movement of the sensitivity in the heat flux case, LE

4.6 Summary LE

The geometry characteristics of the leading edge model are very simple in order to understand the phenomena that occur during the simulation. The sensitivity analysis of this case is based on the inlet Mach number variation. By changing the inlet Mach number, the blowing ratio of the holes changes also, this leads to a variation of the heat flux, overall effectiveness and temperature on the vane.

The influence of the blowing ratio can be expressed as follows: the higher the blowing ratio the higher is the inertia and the momentum of the coolant flow with respect to the main flow. When the blowing ratio is particularly high, the coolant fluid has got such an inertia that it can detach from the surface. Moreover, since the velocity of the coolant and the main flow are orthogonal also the coolant exit velocity direction is influenced. Hence, for low blowing ratios the coolant is directed towards the main flow and the most sensible zones are oriented in the horizontal direction. The influence on the detachment and the velocity direction can be seen in Figure 4.14.
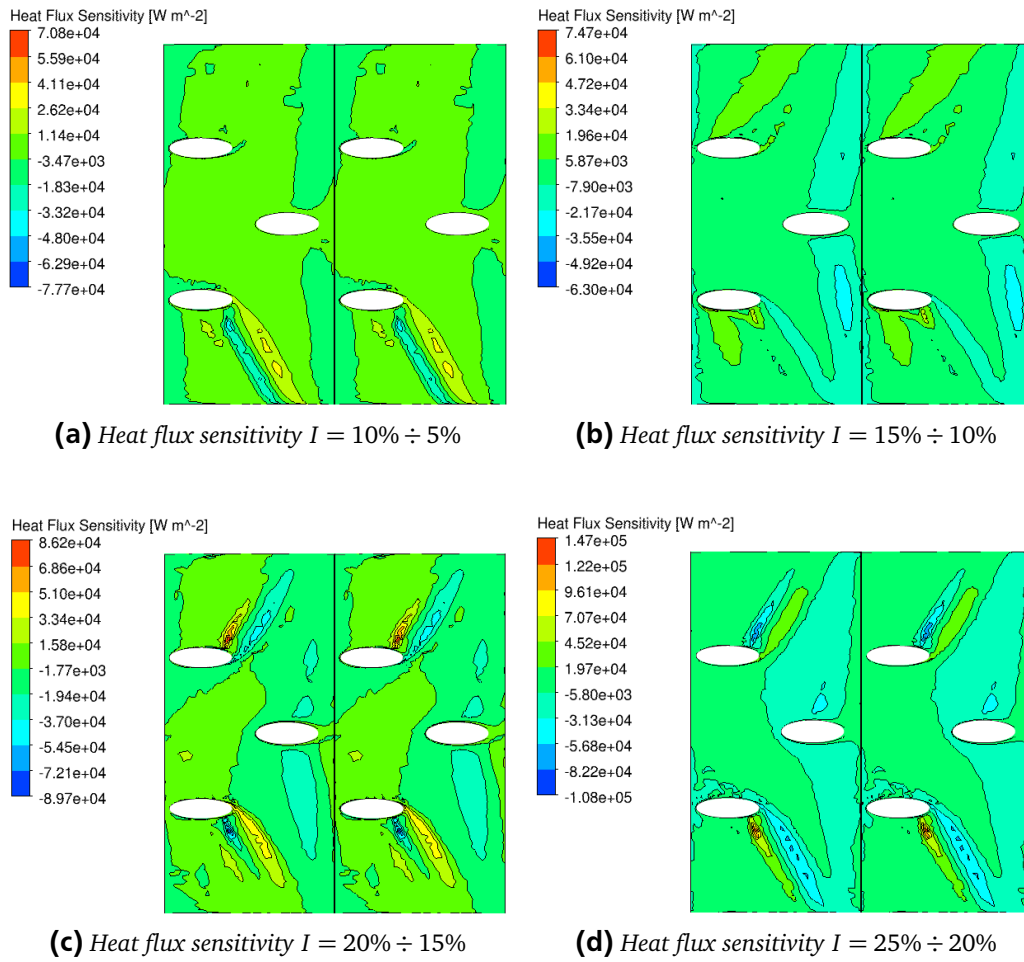
(a) *Heat flux sensitivity* $I = 10\% \div 5\%$

(b) *Heat flux sensitivity* $I = 15\% \div 10\%$

(c) *Heat flux sensitivity* $I = 20\% \div 15\%$

(d) *Heat flux sensitivity* $I = 25\% \div 20\%$

Figure 4.17: The heat flux sensitivity respect the inlet turbulence, LE

The turbulence intensity seems to increase only the secondary flow sensitivity. The secondary flows that form in the coolant jets are influenced thus the values of the physical quantities change.

The htc distribution on the vane surface seems to be fixed and the wall temperature influence is not present. The areas of sensitivity follow the behavior of the heat flux and the temperature figures. The greatest magnitude of the htc are close to the off stagnation holes.
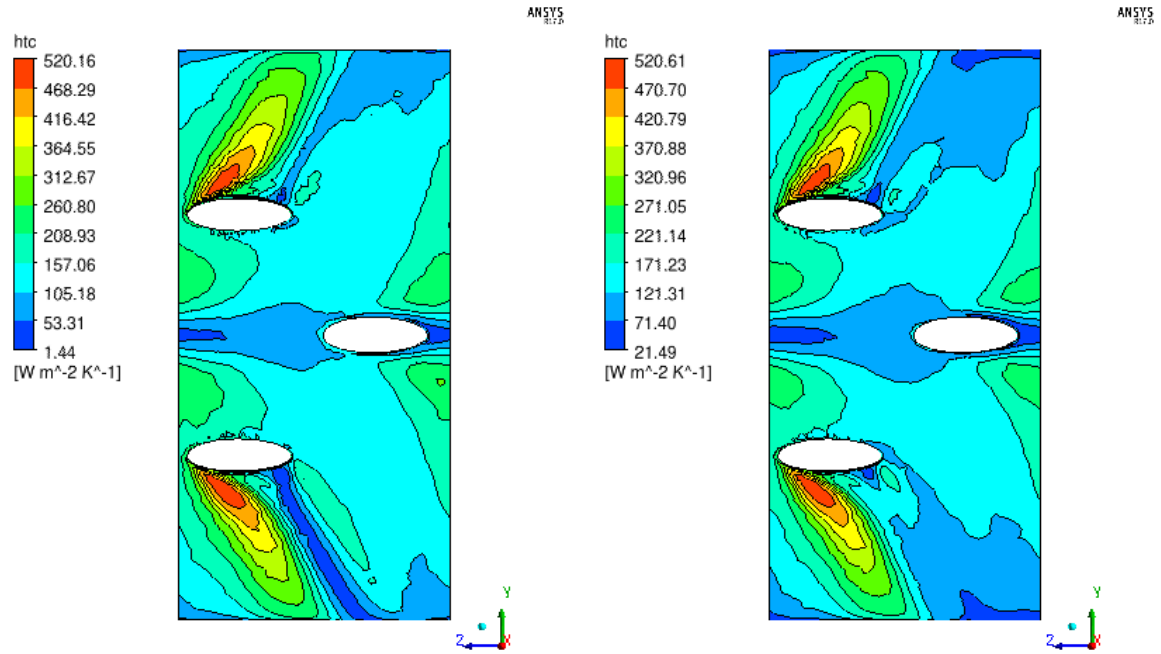
(a) *LE htc using the wall temperature 255 K -235 K in the isothermal wall simulation*

(b) *LE htc using the wall temperature 235 K -275 K in the isothermal wall simulation*

Figure 4.18: htc distribution on the leading edge model for different wall temperature levels

In this section the findings obtained for the MT1 are shown. The MT1 has the separation on the suction side and the film cooling holes influence the formation of the boundary layer. However, in Figures 4.19 it becomes clear that the most effected zone is the separation area. In this case, as for the Mark II, the higher sensitivity zone moves downstream by increasing the pressure ratio. In this case the cause of the separation is not attributable to the shock, because it happen outside the vane. Hence, the detachment of the flow is due to the adverse pressure gradients caused by the vane geometry.
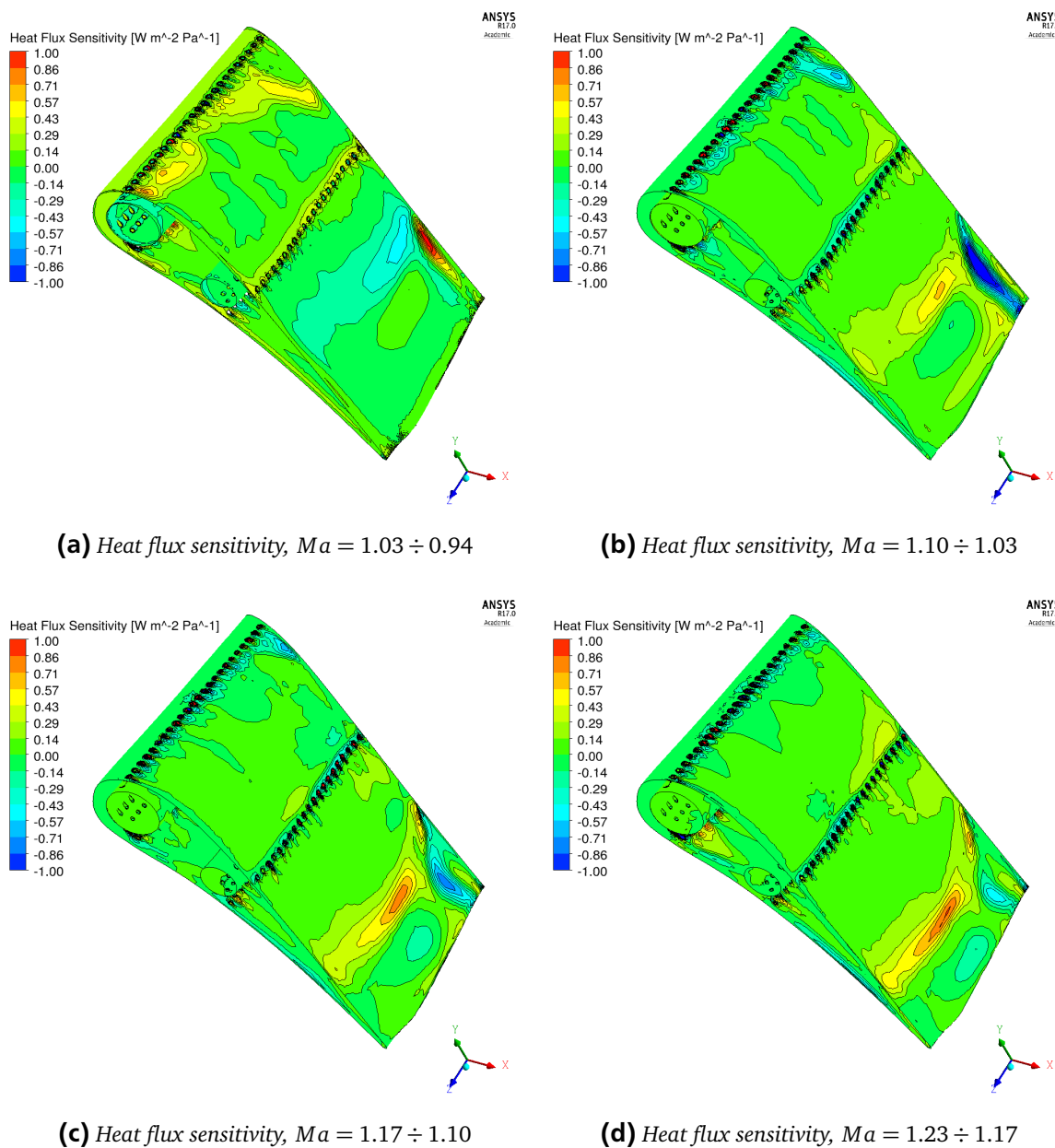

(a) *Heat flux sensitivity,* $Ma = 1.03 \div 0.94$ **(b)** *Heat flux sensitivity,* $Ma = 1.10 \div 1.03$

(c) *Heat flux sensitivity,* $Ma = 1.17 \div 1.10$ **(d)** *Heat flux sensitivity,* $Ma = 1.23 \div 1.17$

Figure 4.19: The movement of the sensitivity in the heat flux case

The figures use the same legend. It can be seen that the sensitivity magnitude increase by increasing the exit Mach number. In the first picture the Mach number step is such that the separation phenomenon does not occur. Because of that, the values of the sensitivity are due to the growth of the boundary layer thickness. Only in this case it is possible to find the Reynolds number influence. According to the pictures in Figure 4.19, the most affected zone is the separation area; By increasing the Mach number the movement of the high sensitivity zone is evident. Towards the trailing edge of the suction side, it can be seen the influence of the secondary flow, which starts from the separation zone.
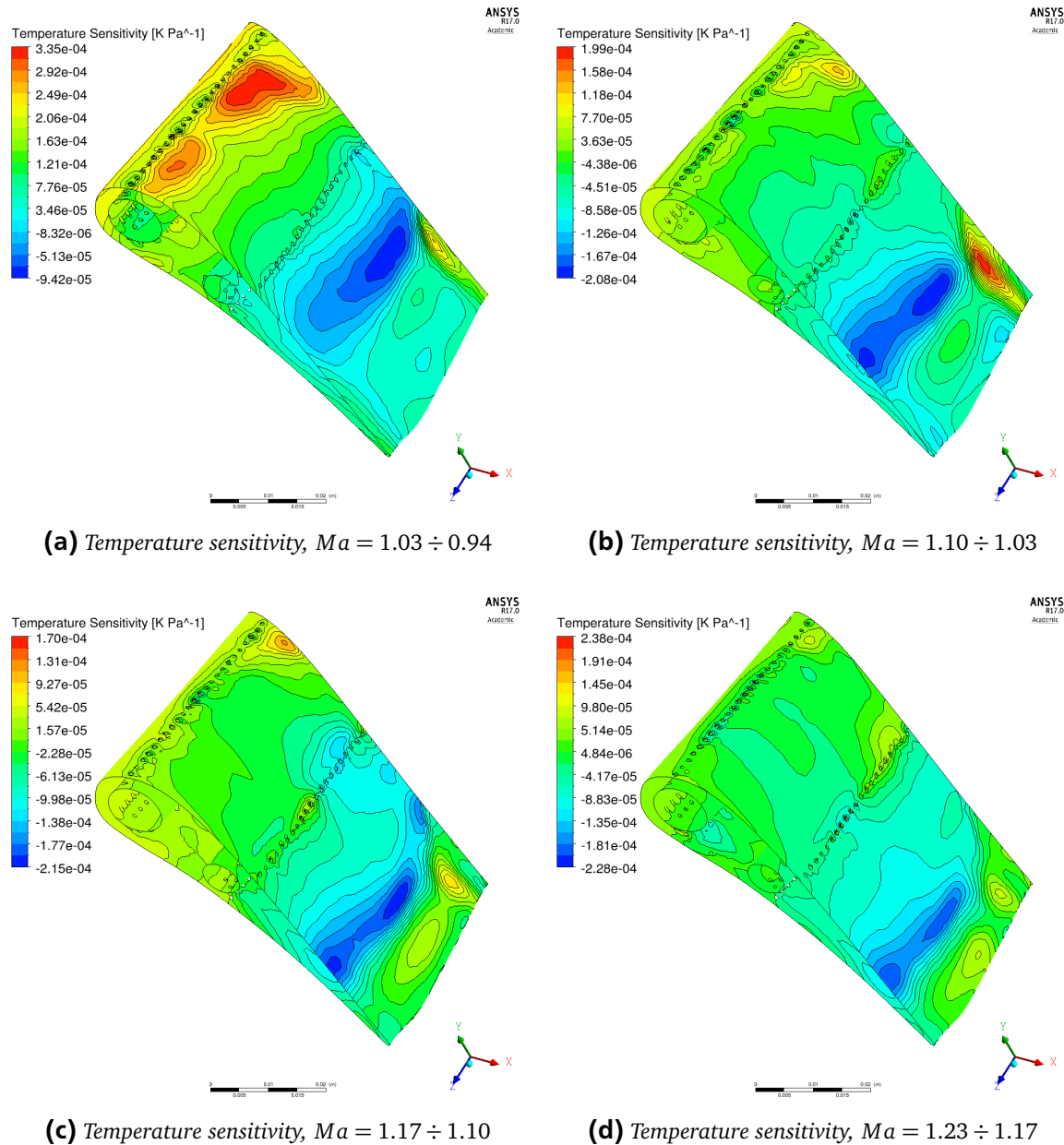

(a) *Temperature sensitivity, $Ma = 1.03 \div 0.94$*

(b) *Temperature sensitivity, $Ma = 1.10 \div 1.03$*

(c) *Temperature sensitivity, $Ma = 1.17 \div 1.10$*

(d) *Temperature sensitivity, $Ma = 1.23 \div 1.17$*

Figure 4.20: The movement of the sensitivity in the temperature case

The relation between heat flux and temperature is still present in the MT1 case. In fact, increasing the heat flux the temperature sensitivity decreases.

The last inlet parameter investigated is the inlet turbulent intensity. The Picture 4.21 shows that there is no influence on the separation zone position, because the turbulent intensity affects phenomena such as the laminar to turbulent transition. The most affected zone is the region close to the leading edge and the first row of film cooling holes. The secondary flows that form in the cooling jets is thus affected by the highest fluctuation of the particles in the flow. In order to compare
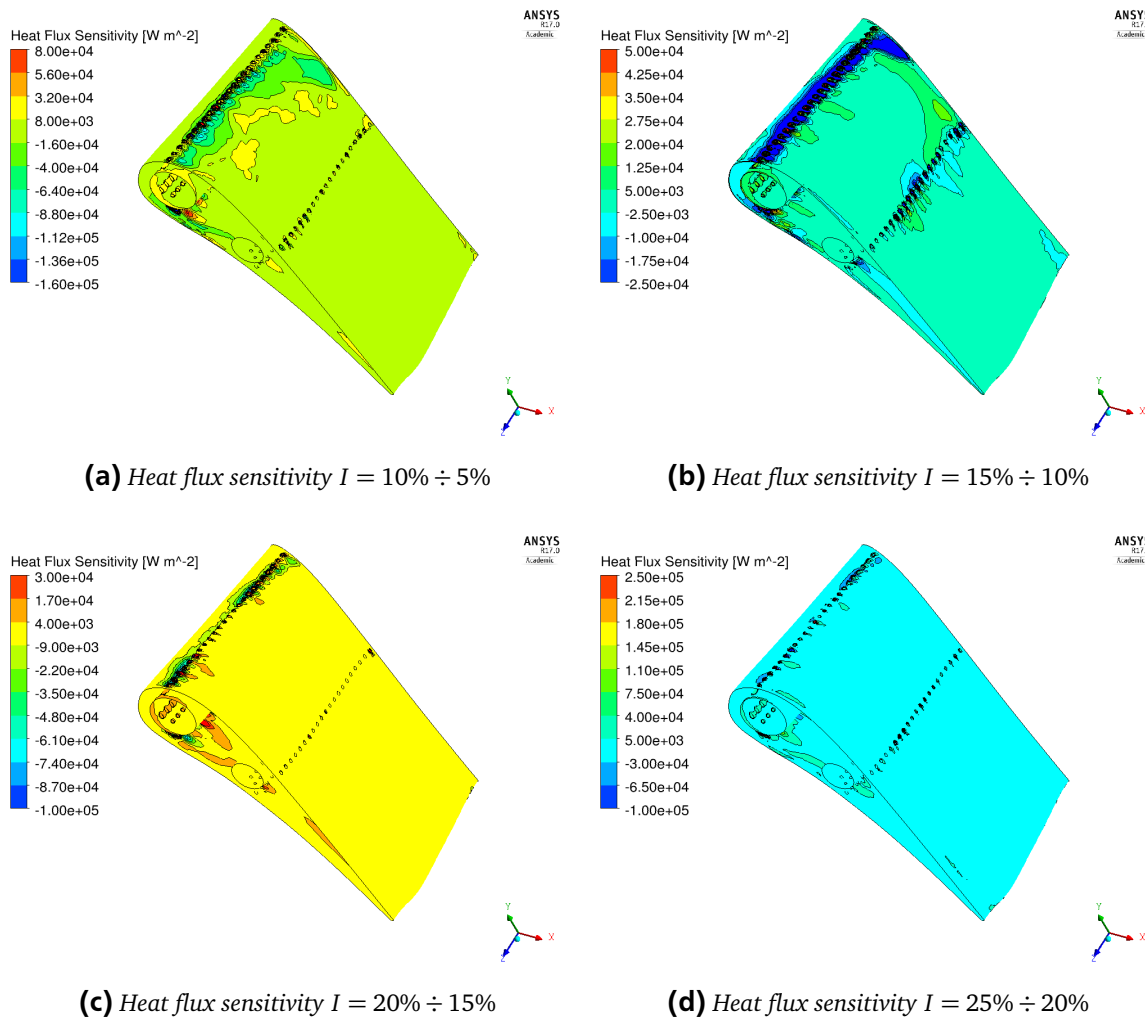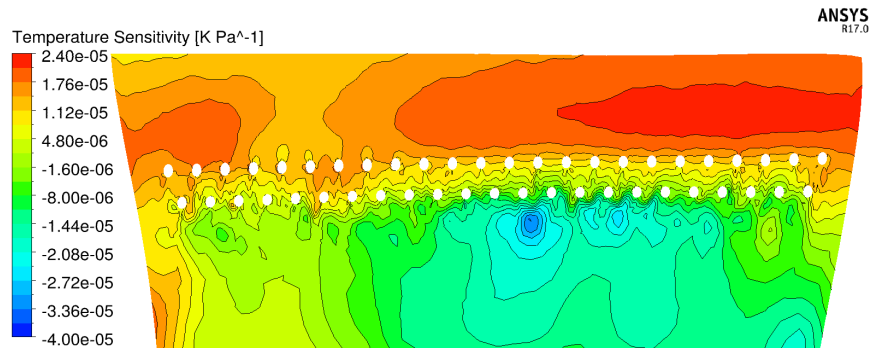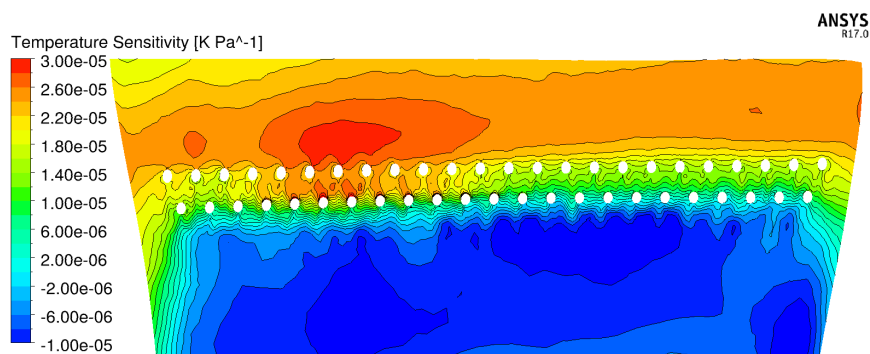

(a) *Heat flux sensitivity I = 10% ÷ 5%*

(b) *Heat flux sensitivity I = 15% ÷ 10%*

(c) *Heat flux sensitivity I = 20% ÷ 15%*

(d) *Heat flux sensitivity I = 25% ÷ 20%*

Figure 4.21: The inlet turbulent intensity influence on the sensitivity

this case with the leading edge model, the inlet Mach number is varied.

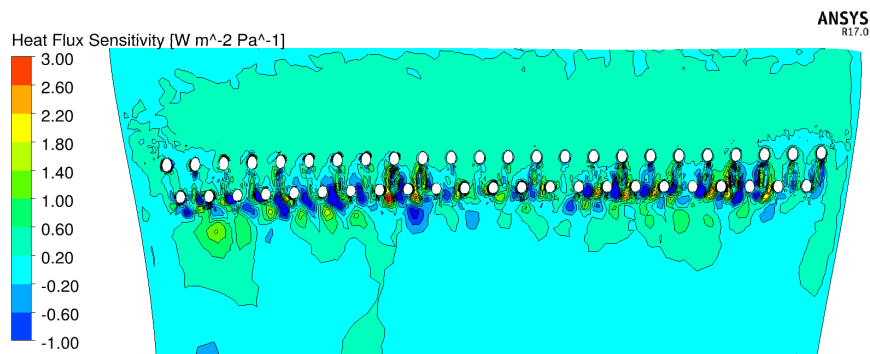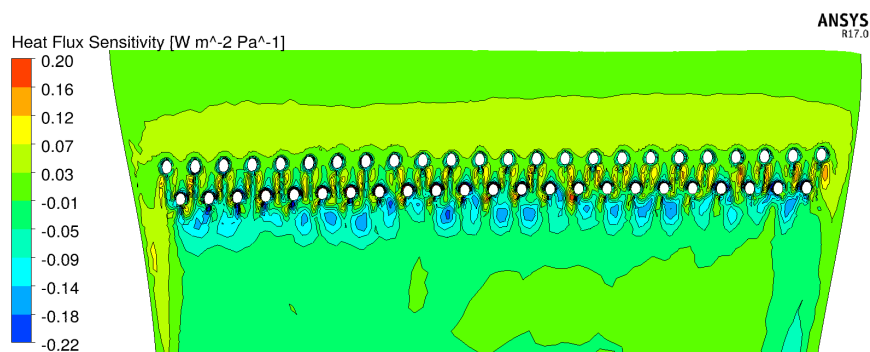**(a)** *Temperature Sensitivity, $Ma = 1.38 \div 1.03$*

(b) *MarkII Sensitivity, $Ma = 1.65 \div 1.03$*

Figure 4.22: Temperature sensitivity on the MT1

(a) *MT1 Sensitivity , $Ma = 1.38 \div 1.03$*

(b) *MT1 Sensitivity, $Ma = 1.65 \div 1.03$*

Figure 4.23: Temperature sensitivity on the MT1

From these Figure 4.22 and 4.23 comes out that the influence of the inlet Mach number is not so strong. Because in the simulation setups for the MT1, the blowing ratio is low, hence the detachment can not be seen. As a consequence, the high sensitivity zones seem to be placed close to the hole and the areas have a form of stripes. The physical reasons which lead to the formation of the high sensitivity areas are the different mass flow that comes out from the cooling holes. Moreover, the secondary flows are also influenced by means of a different coolant mass flow.

Also in Figure 4.22, can be found the same influence as in the case of the heat flux. The variation of the Mach number leads to a change of the blowing ratio, too. However, since there is no separation for these cases, the effect of the inlet parameter is represented in the stripes downstream of the cooling holes. Even though the inlet Mach number influences the secondary flows, in the temperature contour its effect is not much visible.

Other Figures of the sensitivity are attached in the appendix.

4.8 Heat Transfer Coefficient MT1

The distribution of the htc, calculated with the 2point method, at the half span of the MT1 vane is shown in Figure 4.24
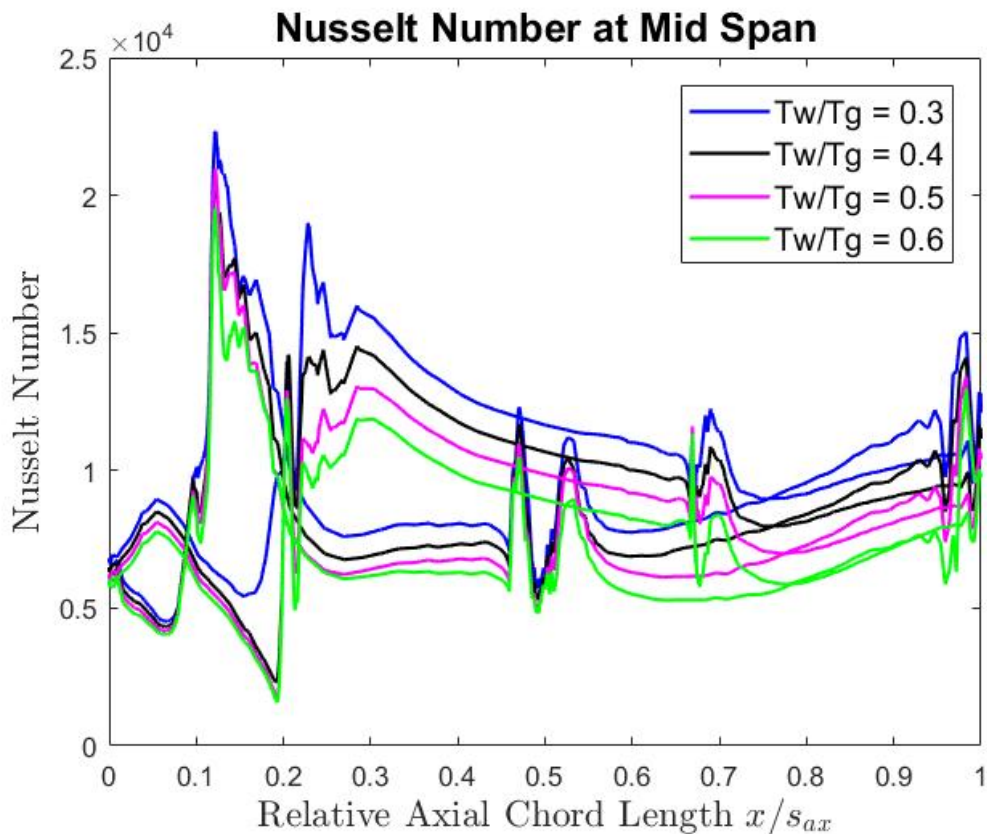

Figure 4.24: The Nu number distribution at mid span

It implies the dependence of the Nu number on the temperature wall-temperature gas ratio. The temperature ratio dependence means that the aerodynamic configuration of the vane is not the

only factor that influences the htc. Because of the film cooling, the classical method for the htc prediction is not adequate in certain conditions. The complexity of the vane due to geometry and the cooling holes makes the classic prediction less secure.

In this case, the method proposed by Maffulli [12] could give better results, but as shown in Figure 4.25, the prediction of the Nusselt number overestimates the values.

By concerning this high error the method fails in its purpose, as can be seen in the other figure in the appendix. Using this method for the simple cases, the agreement is very satisfying, but when the complexity of the vane is important and when the film cooling is present the Maffulli method differs from the classic method. The coefficients h_0 and $h1$ are calculated using isothermal simulations. The $\frac{T_w}{T_g}$ ratio is changed by varying the T_w. Moreover, an adiabatic simulation is also run in order to get the adiabatic wall temperature distribution. To obtain the coefficients the system 2.28, is solved in Matlab for each node of the mesh using the relative heat flux. However, even if another temperature and heat flux set are used the error of the Nu number is high, too.
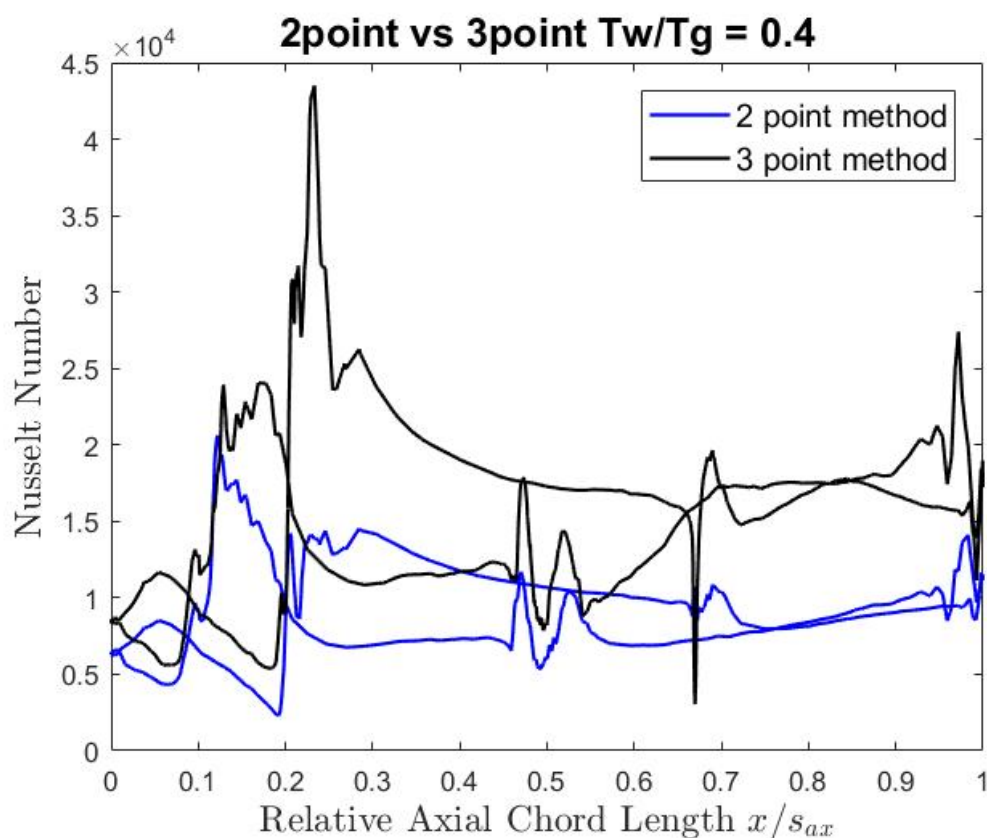

Figure 4.25: The Nu number distribution comparison between the classic method and the Maffulli Method, $\frac{T_w}{T_g} = 0.4$

Finally, the Nusselt number is very difficult to predict when the film cooling is used in the vane. The CHT simulation could be a very useful tool to estimate the heat transfer. Whilst, the prediction in the simple cases does not require this effort. The Nusselt distributions for different temperature ratios are available in the appendix.

The MT1 NGV is analysed during the thesis. In this case, there is no shock within the vane, but a separation is, however, present. The separation happens due to the adverse pressure gradients on the suction side of the vane. Moreover, film cooling holes are situated in the pressure and suction side. The inlet Mach number is varied in the simulation in order to compare the findings with the other cases.

Dealing with the separation, it can be seen that the heat flux sensitivity, Figure 4.19, has the same behavior as seen in the Mark II section. The greatest values of the sensitivity are situated in the separation zone, that moves towards the trailing edge when increasing the Mach number. The heat flux sensitivity tends to increase by increasing the inlet Mach number. In the first picture of Figure 4.19, the sensitivity magnitude is negative in the separation zone; this happens because the main flow does not separate from the wall and the negative values are due to the growing thickness of the boundary layer. Taking into account the vane in Figure 4.26, in particular the suction side, the flow is laminar after the stagnation thus the boundary layer starts to increase and the htc decreases. Then, the transition occurs and there is a strong increment in the htc distribution since the turbulent regime allows higher heat flux. Subsequently, the boundary layer increases its thickness and the htc decreases.
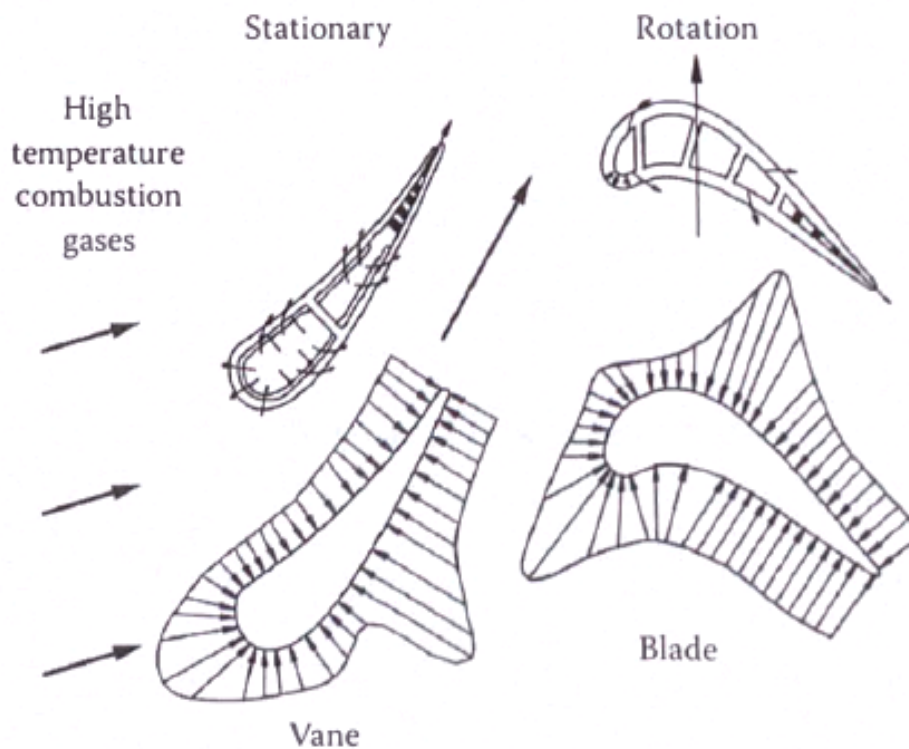

Figure 4.26: htc distribution on a vane and a rotor, [10]

Varying the inlet turbulent intensity, the MT1 vane shows a constant value of the sensitivity in the major part of the vane, but close to the film cooling holes it is possible to see some sensitivity zones. These areas are formed because of the influence of the secondary flows which form in the cooling jets.

Since this wall temperature dependence, the 3 point method, proposed by Maffulli, should work in a better way. However, the values of the Nusselt number differ from the classic method htc distribution. The 3 point method follows the dependence of the wall temperature, but the values of the htc are overestimate.

5 Cases Comparison

At this point, the influence of the parameters that affect the sensitivity were analysed. Now the purpose is to compare the cases using the same inlet parameters.

5.1 MT1 vs Mark II

The parameter used for the comparison is the exit Mach number. The aim of the thesis is to compare the results using the same inlet properties, but in this case, in order to stick with the Hylton et al. experimental results, the exit Mach number is used. Furthermore, the gradients obtained with the inlet Mach number and the outlet Mach number variation are similar. The strategy is to use a reference state and than to understand the sensitivity behavior. The reference state is $Ma = 1.02$.

In the following pictures the behavior of the sensitivity for the MT1 and Mark II cases is shown. Figure 5.1 points out that the sensitivity magnitude of the temperature in the separation zone is
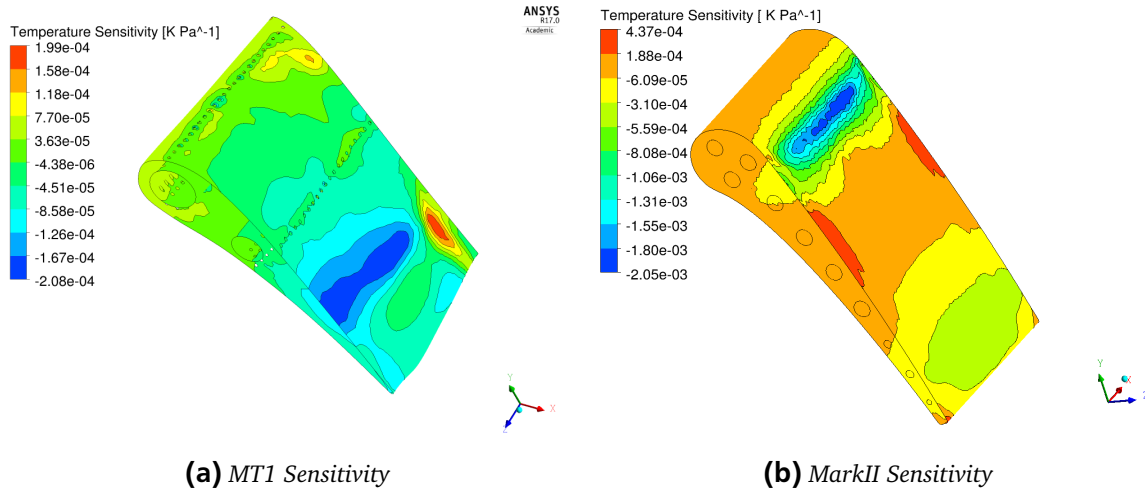

(a) *MT1 Sensitivity*   **(b)** *MarkII Sensitivity*

Figure 5.1: Temperature sensitivity comparison $Ma = 1.02 \div 0.94$

negative. The same happens in the Mark II figure. The same trend is found in the Figures 5.2a and 5.2b. It is important to emphasise that the magnitude of the sensitivities decreases, in absolute value, and the most affected zone moves downstream for both cases. Moving away from the reference state, the magnitude keeps decreasing and most affected zones keep moving downstream. This means that the separation moves downstream by increasing the exit Mach number and the value of the temperature absolute value tends to decrease. As a consequence, the most affected zones have lower magnitudes. In the appendix it is possible to find the sensitivity pictures for the
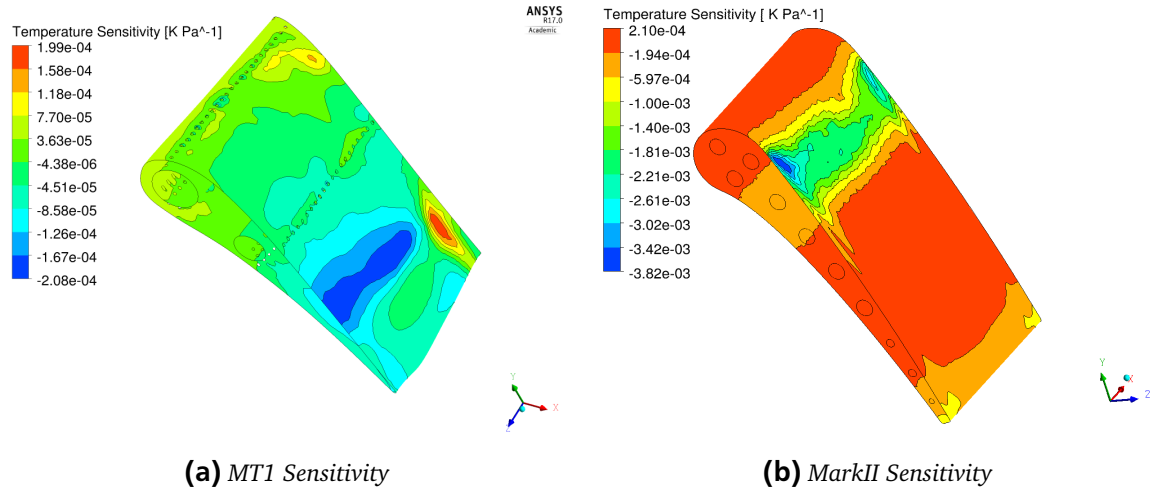
(a) *MT1 Sensitivity* **(b)** *MarkII Sensitivity*

Figure 5.2: Temperature sensitivity comparison $Ma = 1.07 \div 1.02$

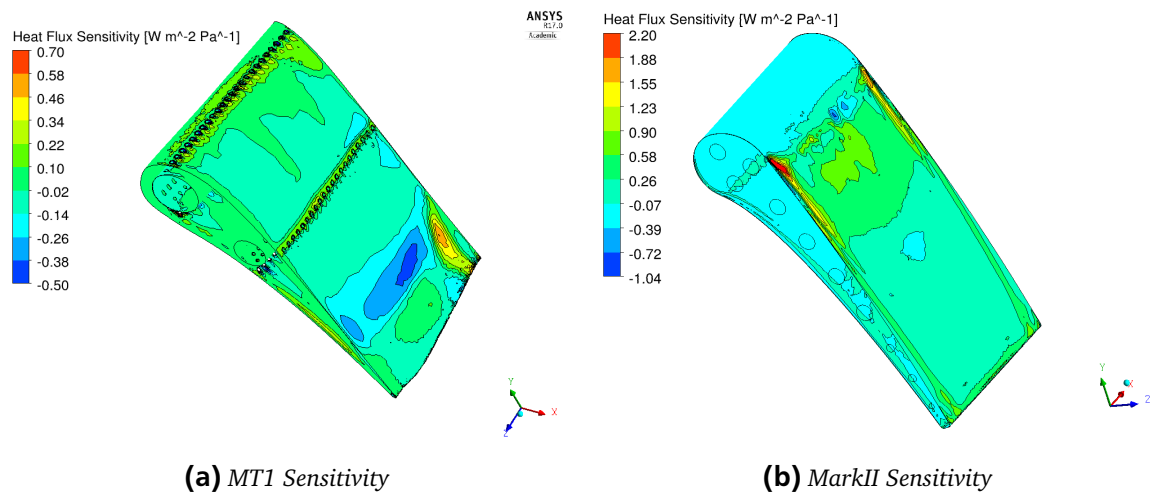**(a)** *MT1 Sensitivity* **(b)** *MarkII Sensitivity*

Figure 5.3: Heat flux sensitivity comparison $Ma = 1.23 \div 1.07$

heat flux.

5.2 MT1 vs LE Model

The simulations performed for the MT1 and LE model are now compared in order to find a possible correlation between the phenomena that occur in the low fidelity test case LE, see section 4.4, and the findings of the MT1.

The way to proceed is the same as the previous section: a reference state is set and the variation of the sensitivity from the reference is analysed. The reference Mach number is $Ma = 1.04$. In this case the inlet Mach number influence is evaluated.
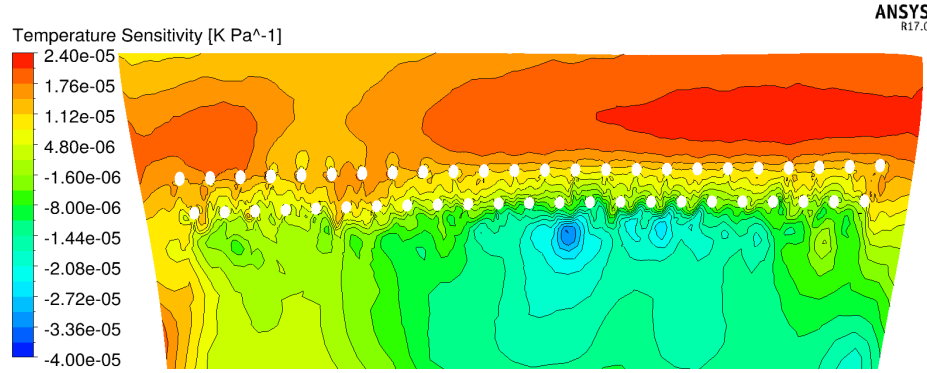
(a) $Ma = 1.07 \div 1.04$.
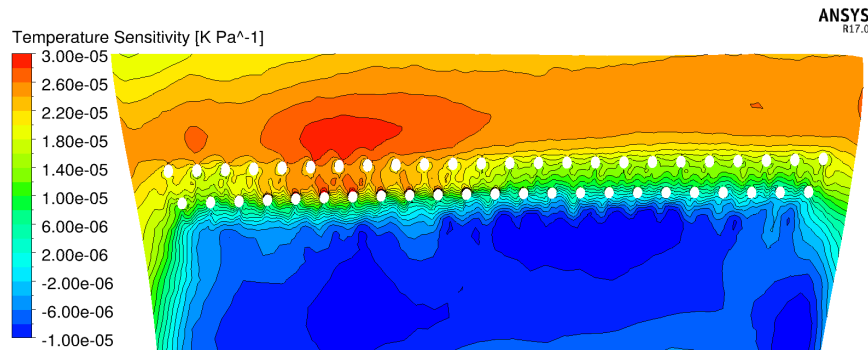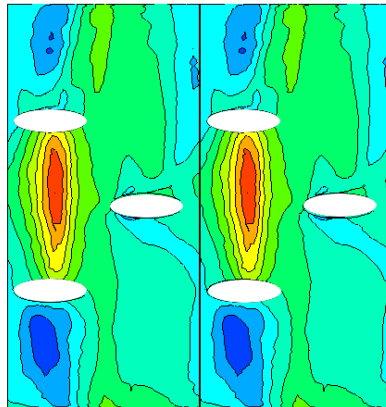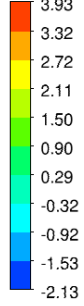

(b) $Ma = 1.10 \div 1.04$.

Figure 5.4: Temperature sensitivity comparison, MT1

In both cases, the blowing ratio is low. So that, the detachment does not occur and the velocity direction of the coolant is very close to the main flow velocity.

In the temperature contours of the MT1 vane it is not possible to see the stripes of sensitivity. However, there is a gradually decrease of the temperature. The goal of the film cooling is to cool the vane. Moreover, the presence of high sensitivity zones means that there are areas in the vane in which the temperature increases more than other vane regions. This leads to temperature gradients which can create mechanical stress on the vane.
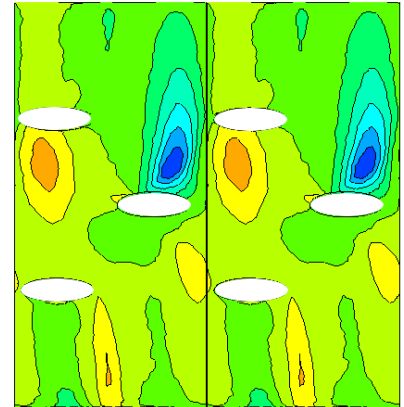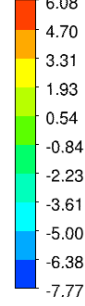
The temperature contours of the leading edge model, and in particular in the zone downstream of the stagnation holes, the magnitude of the sensitivity is lower compared to the other case. The uniformity of the sensitivity is an advantage in order to avoid thermal stresses.

(a) $Ma = 1.07 \div 1.04$

(b) $Ma = 1.10 \div 1.04$

Figure 5.5: Temperature sensitivity comparison, LE

Other figures are available in the appendix.

6 Final Summary and Conclusion

The aerothermal prediction is very important in turbine vanes, nowadays. The TET is growing in order to achieve a greater turbine efficiency and the vanes are called to support very high thermal load. The material used in the industry is not strong enough to hold the thermal load, hence a vane cooling system is required in order to avoid failures. The most important cooling systems in a high pressure turbine vane is internal cooling and film cooling. The fresh air passes through the internal cooling ducts and then feeds the film cooling holes. The coolant comes out of the cooling holes forming a film around the vane that isolates the vane.

At this point, the numerical simulations are required to simulate the vane load. In this thesis conjugate simulations are used. These simulation are precise because they can predict the heat conduction and convection by dealing with the influence of the solid domain. However, the computational power required in this simulation is very high. In spite of this negative aspect, the popularity of the CHT simulation is growing. Industries use the classic method to simulate the thermal load because it is very robust and in a lot of cases the predictions are good enough. This thesis has also the aim to evidence that the precision of the CHT simulation is greater.

To achieve these objectives three numerical models are used. The first is a vane with a constant profile along the radial direction. The vane is cooled by ten internal ducts in which the fresh fluid can go across. Hylton et al. [11], has performed an experimental work in order to estimate the influence of the outlet parameters on the heat transfer of the vane. The vane is identified as Mark II.

Since the film cooling is also a matter of interest of the thesis, the second numerical setup is a leading edge model with one hole in the stagnation line and two off stagnation holes arranged at $\pm 25^o$ from the stagnation line. The case was analysed by Dobrowolski [9] and published by Ravelli [14]. The last case is the MT1 NGV in which it is possible to find the film cooling and the internal cooling at the same time.

The findings obtained in the two low fidelity test cases, the Mark II and the leading edge model, are evaluated in order to find similarities in the MT1 results. The aim of this process is to understand the main sources of influence.

To estimate the influence of the parameters variation, the sensitivity value is used. The information that the sensitivity gives is related to the susceptibility of a certain zone to a variation of a parameter. It is gradient derived for an inlet parameter.

Concerning the case of the Mark II [11], the influence of the exit parameter was evaluated in Hylton's paper. He demonstrates that the influence of the exit Reynolds number is constant for the whole vane. In particular there is a shift of the physical values, Figure 3.9, but there is not a region in which it is possible to find a marked growing in a physical quantity. Moreover, the exit Mach number influence is more interesting, Figure 3.8. Hylton concludes that, since the Mach number

influence is stronger than the Reynolds influence, the effect is caused by a separation phenomenon rather than a laminar-turbulent transition.

In the leading edge model, Ravelli has drawn attention on the influence of the blowing ratio. In the thesis case, the inlet Mach number is varied, but, as a consequence, also the blowing ratio changes. The most important factor of influence are the detachment of the coolant, due to a higher inertia compared to the main flow, and the influence of the velocity direction of the fresh flow.

The results of the MT1 are now elaborated. The effect of the separation of the flow in the suction side is present. However it happens not for a shock, as in the case of Mark II, but the reason can be attributed to adverse pressure gradients due to the geometry. Regarding the film cooling, since the blowing ratio of the simulation is low, it is not possible to see the separation of the flow. The only influence on the sensitivity value can be attributed to the different coolant mass flows.

6.1 Conclusion

By means of the factors of influence explained previously it is possible to say that, in the case of the Mark II vane, the influence of the Mach number is interesting because it predicts a very high sensitivity in the separation zone. This zone moves towards the trailing edge by increasing the exit Mach number as supposed to be. The inlet turbulence intensity is also evaluated, but the high sensitivity zone is fixed. This happens because the parameter affects the laminar-turbulent transition, but since the transition influence is lower than the separation phenomenon, the sensitivity value is low. By varying the inlet turbulence intensity, the position of the shock is not influenced and thus the high sensitivity zones are fixed.

The simulation performed in the case of the leading edge show a great influence of the detachment and the velocity direction. But this happens only for high blowing ratios. In fact, by decreasing the value of the blowing ratio, the sensitivity on the vane seems to be much more homogeneous. Concerning the inlet turbulence intensity, the secondary flows of the coolant are affected. Hence, the zones close to the holes show the stripes of sensitivity due to the variation of the secondary flow properties.

Now, the findings obtained are superimposed on the MT1 vane. Also in this case it is possible to notice the movement of the sensitivity in the suction side of the vane. The movement is influenced by the exit Mach number, in this case too.
Concerning the film cooling, since the cooling ratio is low in the case comparison, it is not possible to see the stripes of the sensitivity. As in the leading edge model, it is possible to notice a gradual decrement of the temperature sensitivity, for example. Hence, the gradual sensitivity reduction means that, in these zones there are no strong temperature gradients. So that, the thermal load on the vane is not so strong.

Another important goal of the thesis is the calculation of the htc. As it is possible to read in the uncoupled simulation done for the Mark II case, the distribution of the temperature or the heat flux does not show a dependence on the aerodynamics of the vane. For example, there is no influence of the shock on the vane surface and also the value of the physical quantities seems to be

constant along the radial direction. Moreover, the Figure 4.8 shows a very clear temperature wall dependence and this, in theory, should not occur. The Maffulli method [12] is used to take into account this dependence. The results obtained, show that the Maffulli method works for a large range of temperature, whilst the classic method loses its power when it is used to simulate wall temperature that are far from those used to calculate it.

Whilst, in the case of the leading edge model the htc distribution seems not to be affected by wall temperature changes. This means that in this case the htc can be considered constant.

In the MT1 case, Figure 4.24 shows the dependence of the htc from the wall temperature. In this complex case, the htc is not easy to predict and also the Maffulli method overestimates the value of the htc. However, the 3-point method follows the dependence of the wall temperature. In the end, the classic htc calculation method works only in easy cases and, sometimes, even if much more complex methods are used the thermal prediction is not satisfactory. Hence, in order to better estimate the heat transfer, the CHT simulation can be used. The advantages are a better prediction of the aerodynamics and also to better understand the aerothermal behavior of the vane.
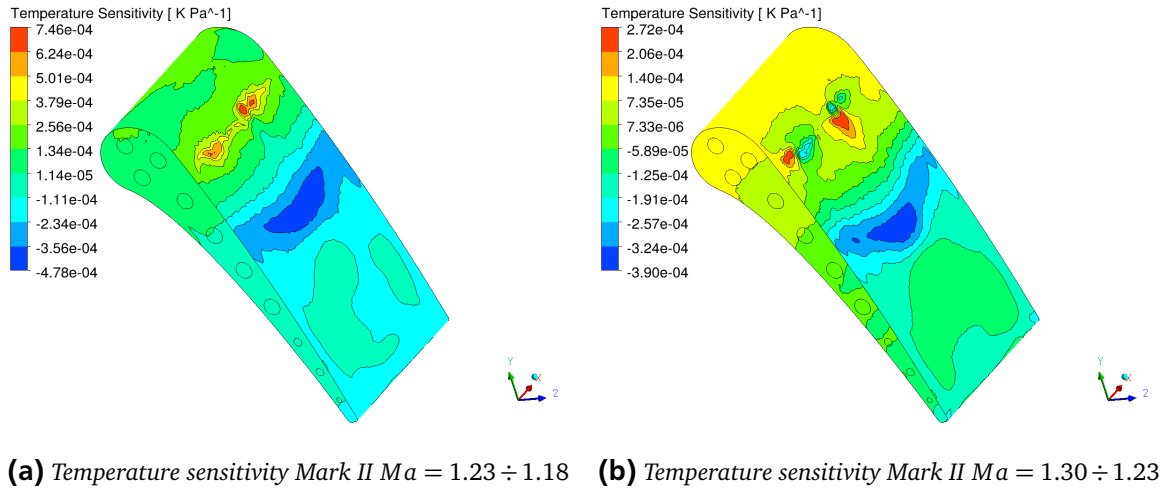
A Appendix

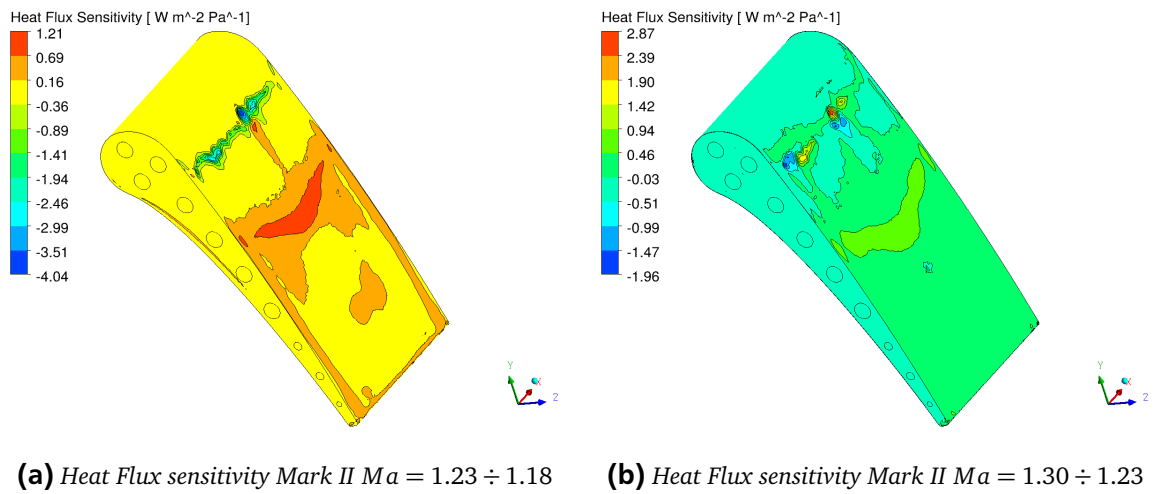## A.1 Mark II Results

(a) *Temperature sensitivity Mark II $Ma = 1.23 \div 1.18$* **(b)** *Temperature sensitivity Mark II $Ma = 1.30 \div 1.23$*

Figure A.1: Temperature sensitivity in the Mark II

(a) *Heat Flux sensitivity Mark II $Ma = 1.23 \div 1.18$* **(b)** *Heat Flux sensitivity Mark II $Ma = 1.30 \div 1.23$*

Figure A.2: Heat Flux sensitivity in the Mark II
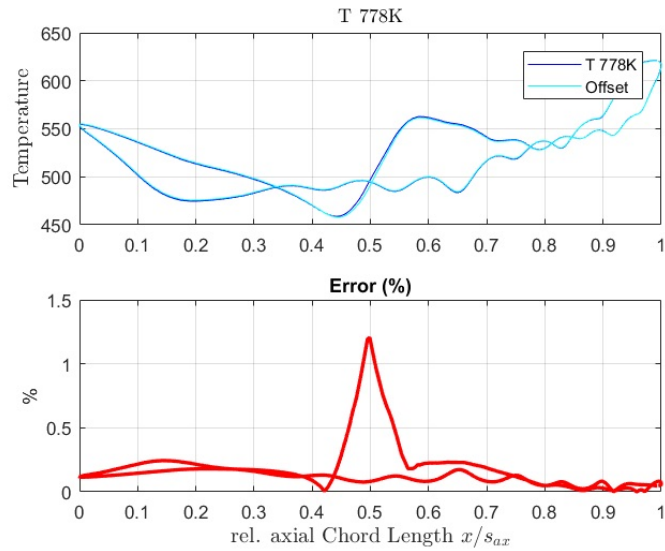
Figure A.3: CFD calculated temperature vs *Matlab* calculated temperature distributions and the relative error, $T = 778K$
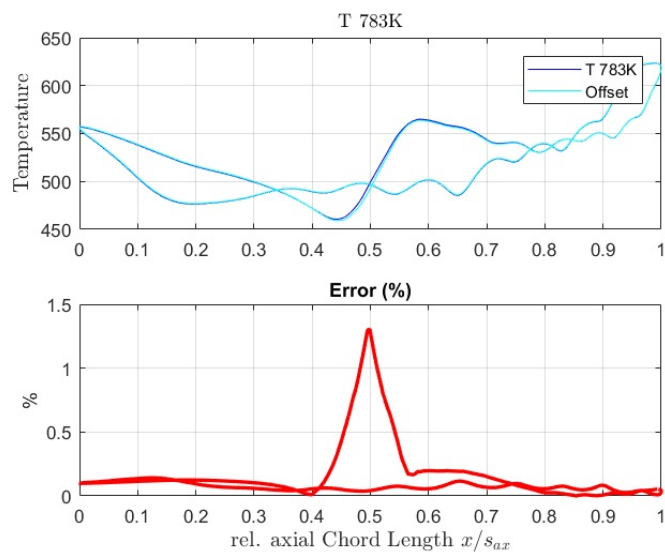
Figure A.4: CFD calculated temperature vs *Matlab* calculated temperature distributions and the relative error, $T = 783K$
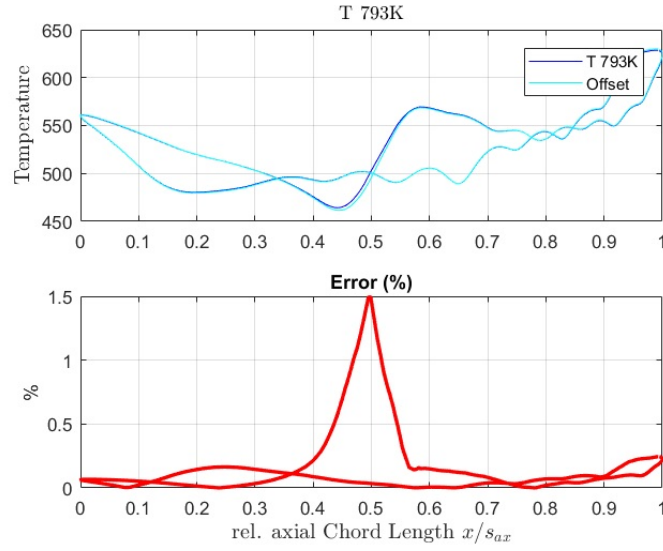
Figure A.5: CFD calculated temperature vs *Matlab* calculated temperature distributions and the relative error,$T = 793K$
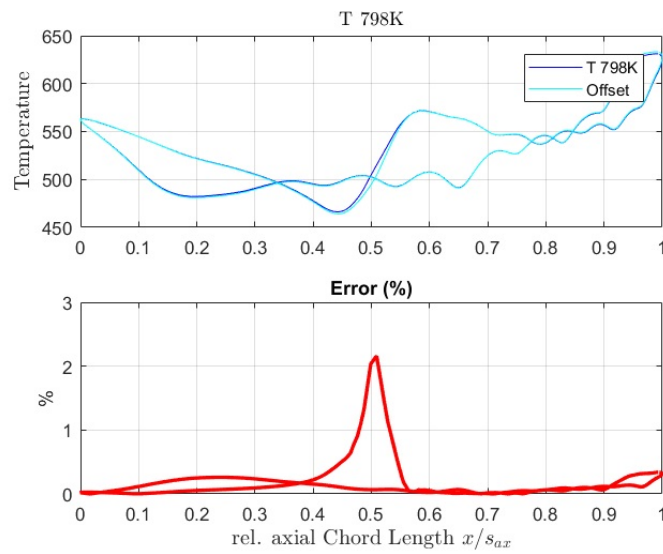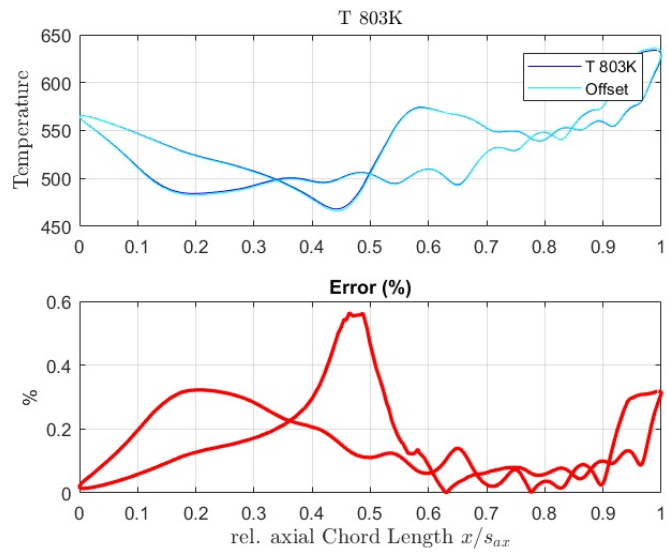

Figure A.6: CFD calculated temperature vs *Matlab* calculated temperature distributions and the relative error, $T = 798K$

Figure A.7: CFD calculated temperature vs *Matlab* calculated temperature distributions and the relative error, $T = 803K$
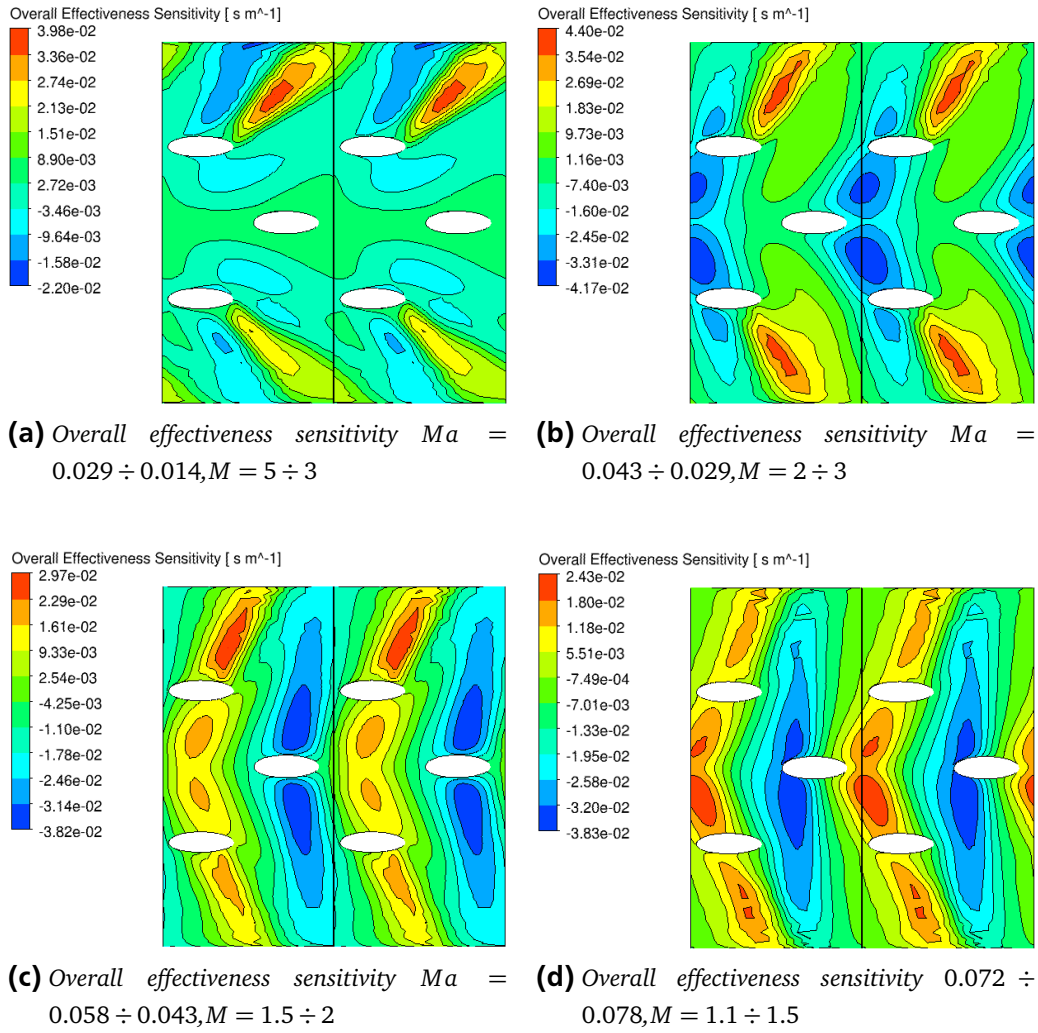
A.3 Leading Edge Result

(a) *Overall effectiveness sensitivity* $Ma = 0.029 \div 0.014, M = 5 \div 3$

(b) *Overall effectiveness sensitivity* $Ma = 0.043 \div 0.029, M = 2 \div 3$

(c) *Overall effectiveness sensitivity* $Ma = 0.058 \div 0.043, M = 1.5 \div 2$

(d) *Overall effectiveness sensitivity* $0.072 \div 0.078, M = 1.1 \div 1.5$

Figure A.8: Overall effectiveness in the leading edge model

(a) *MT1 heat flux sensitivity $Ma = 1.38 \div 1.23$*   **(b)** *MT1 heat flux sensitivity $Ma = 1.46 \div 1.38$*
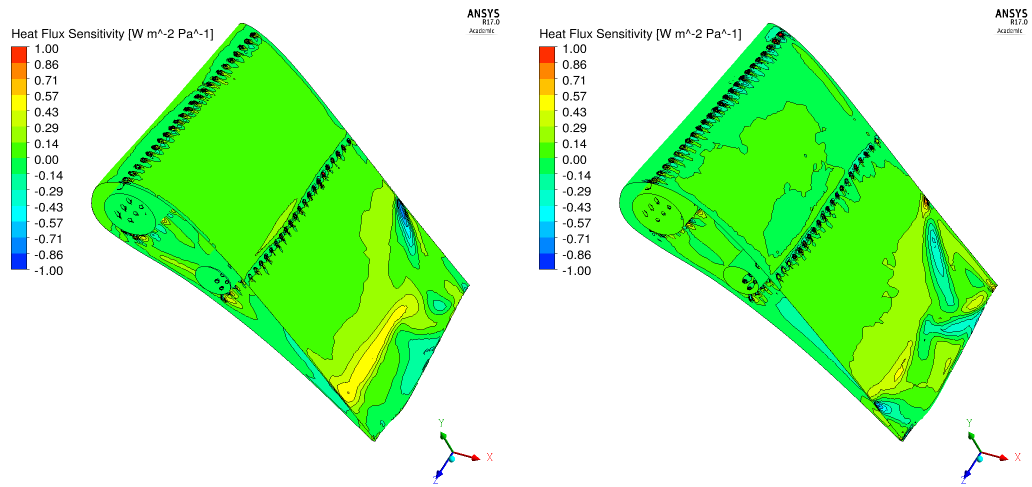
Figure A.9: Heat flux sensitivity in the case MT1

(a) *MT1 temperature sensitivity $Ma = 1.38 \div$ 1.23*   **(b)** *MT1 temperature sensitivity $Ma = 1.46 \div$ 1.38*
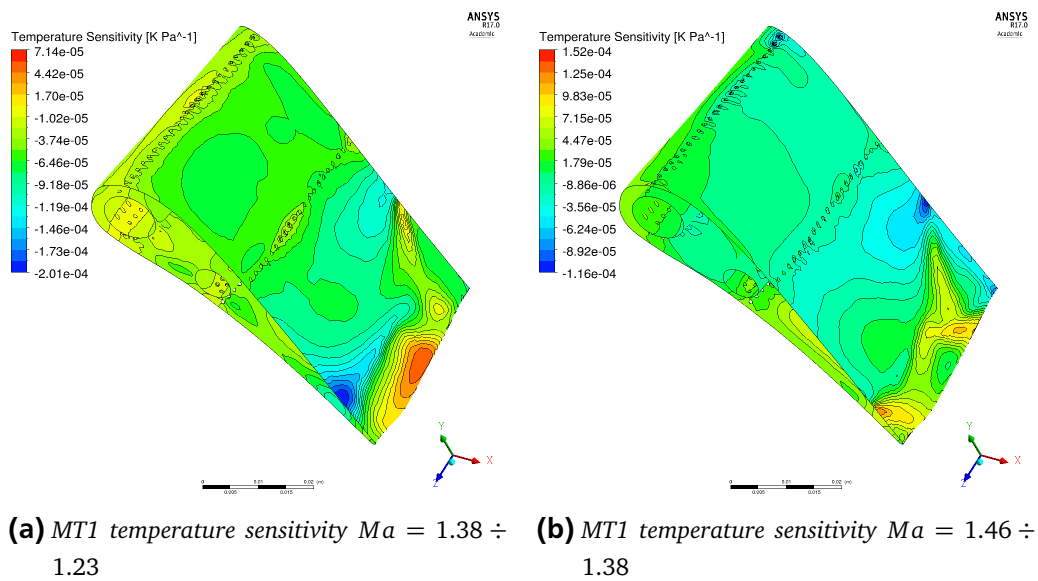
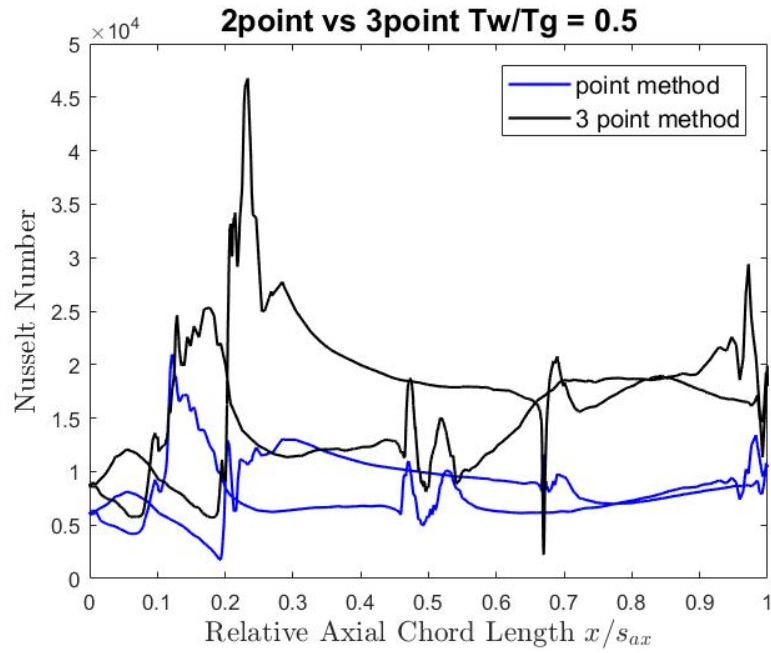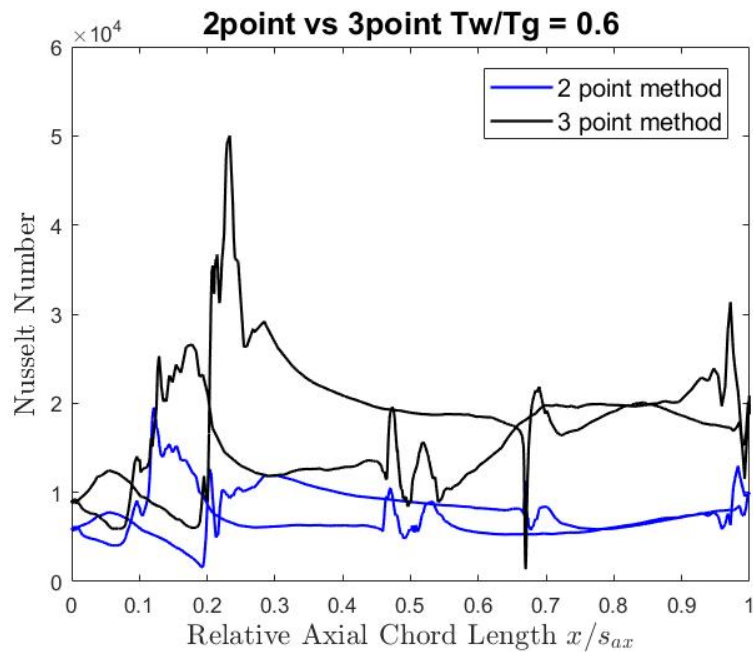**Figure A.10:** Temperature sensitivity in the case MT1

Figure A.11: The Nu number distribution comparison between the classic method and the Maffulli Method, $T_w/T_g = 0.5$
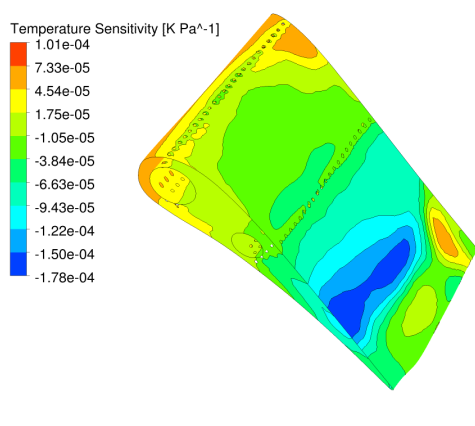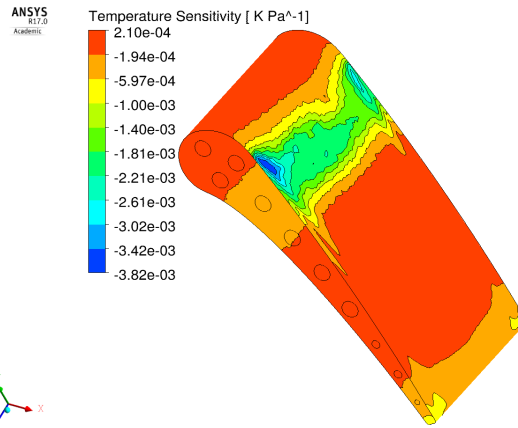

Figure A.12: The Nu number distribution comparison between the classic method and the Maffulli Method, $T_w/T_g = 0.6$
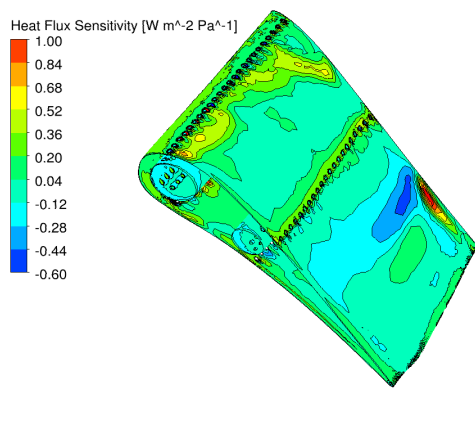
A.6 MT1 vs Mark II
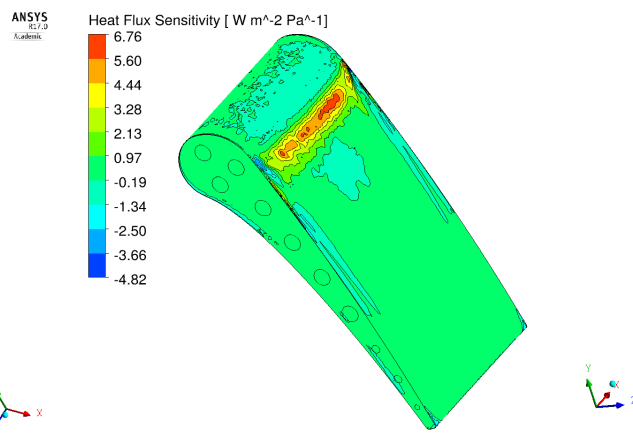
(a) *MT1 Sensitivity*   **(b)** *MarkII Sensitivity*

Figure A.13: Temperature sensitivity comparison $Ma = 1.23 \div 1.02$

(a) *MT1 Sensitivity*   **(b)** *MarkII Sensitivity*

Figure A.14: Heat flux sensitivity comparison $Ma = 1.02 \div 0.94$

(a) *MT1 Sensitivity*

(b) *MarkII Sensitivity*

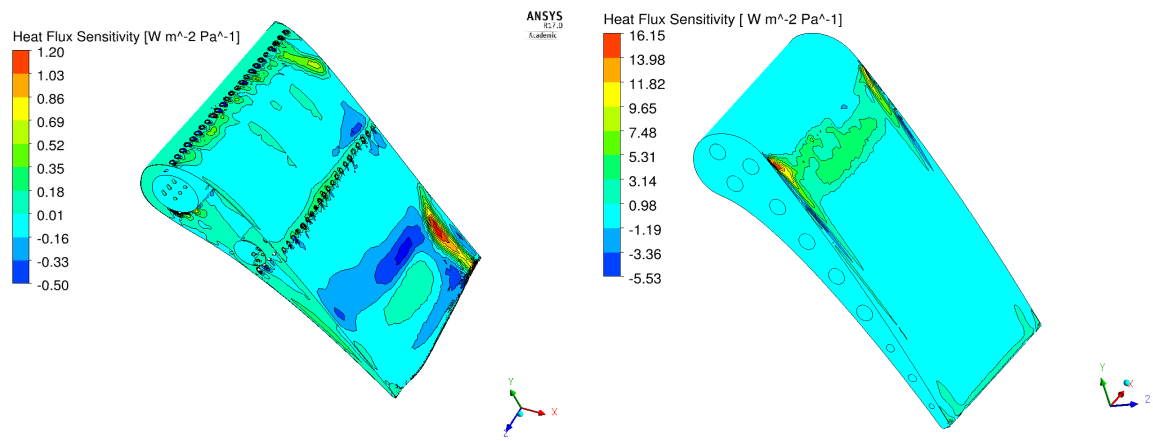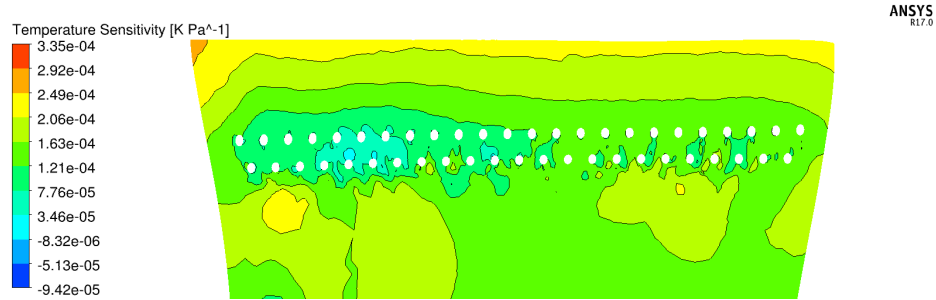**Figure A.15:** Heat flux sensitivity comparison $Ma = 1.07 \div 1.02$

Figure A.16: Temperature sensitivity in the MT1 case $Ma = 1.04 \div 1.02$

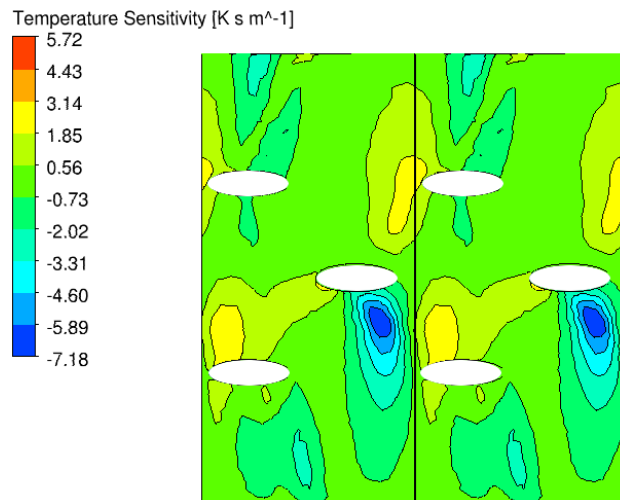**Figure A.17:** Temperature sensitivity in the LE case $Ma = 1.04 \div 1.02$

Bibliography

[1] http://tameo89.altervista.org/blog/index.php/cpu-top-gamma-confronto

[2] http://www.finot.com/ecrits/Damien%20Lafforgue/article_voiles_english.html

[3] https://www.sharcnet.ca/Software/Ansys/17.0/en-us/help/flu_ug/flu_ug_mesh_quality.html

[4] Rolls-Royce plc (1996). The Jet Engine. 5th ed., Derby, England.

[5] BOGARD, D. G.: Airfoil Film Cooling.

[6] CALONI, S. ; SHAHPAR, S. : Investigation Into Coupling Techniques for a High Pressure Turbine Blade Tip. In: *ASME Turbo Expo 2015: Turbine Technical Conference and Exposition* American Society of Mechanical Engineers, 2015, S. V05AT10A017–V05AT10A017

[7] CHANA, K. S. ; POVEY, T. ; JONES, T. V.: Heat Transfer and Aerodynamics of Intermediate Pressure Nozzle Guide Vane With and Without Inlet Temperature Non-Uniformity. In: *ASME Paper No. GT2003-38466* (2003)

[8] DÉLERY, J. ; DUSSAUGE, J.-P. : Some physical aspects of shock wave/boundary layer interactions. In: *Shock waves* 19 (2009), Nr. 6, S. 453–468

[9] DOBROWOLSKI, L. D. ; BOGARD, D. G. ; PIGGUSH, J. ; KOHLI, A. : Numerical Simulation of a Simulated Film Cooled Turbine Blade Leading Edge Including Conjugate Heat Transfer Effects. In: *ASME Paper No. IMECE2009-11670* (2009)

[10] HAN, J.-C. ; DUTTA, S. ; EKKAD, S. : *Gas turbine heat transfer and cooling technology*. CRC Press, 2012

[11] HYLTON, L. ; MIHELC, M. ; TURNER, E. ; NEALY, D. ; YORK, R. : Analytical and experimental evaluation of the heat transfer distribution over the surfaces of turbine vanes. (1983)

[12] MAFFULLI, R. ; HE, L. : Wall temperature effects on heat transfer coefficient for high-pressure turbines. In: *Journal of Propulsion and Power* (2014)

[13] MURTHY, J. Y. ; MATHUR, S. R.: Computational heat transfer in complex systems: a review of needs and opportunities. In: *Journal of Heat Transfer* 134 (2012), Nr. 3, S. 031016

[14] RAVELLI, S. ; DOBROWOLSKI, L. ; BOGARD, D. G.: Evaluating the Effects of Internal Impingement Cooling on a Film Cooled Turbine Blade Leading Edge. In: *ASME Paper No. GT2010-23002* (2010)

[15] SCHETZ, J. A.: Boundary layer analysis. In: *NASA STI/Recon Technical Report A* 93 (1993)

[16] SCHLICHTING, H. ; GERSTEN, K. ; KRAUSE, E. ; OERTEL, H. : *Boundary-layer theory*. Bd. 7. Springer, 1955